

Photo-physical characterization of aromatic compounds for laser-induced fluorescence based diagnostics of fuel concentration, temperature, and equivalence ratio in practical combustion processes

Von der Fakultät für Ingenieurwissenschaften, Abteilung Maschinenbau und Verfahrenstechnik
der

Universität Duisburg-Essen

zur Erlangung des akademischen Grades

eines

Doktors der Ingenieurwissenschaften

Dr.-Ing.

genehmigte Dissertation

von

Thorsten Benzler

aus

Dinslaken

1. Gutachter: Prof. Dr. Christof Schulz

2. Gutachter: Prof. Dr. Stefan Will

Tag der mündlichen Prüfung:

12.04.2019

Summary

This dissertation is based on experiments to determine photo-physical properties of the aromatics toluene, 1,2-xylene, 1,2,4-trimethylbenzene, anisole, 1,4-difluorobenzene, naphthalene and 1-methylnaphthalene under various environmental conditions in the gas phase. Most of these species are part of commercial fuels like kerosene, gasoline, or Diesel or have similar physical and chemical properties. Therefore, their photo-physical properties are used for diagnostics methods in combustion engines and gas turbines to either visualize the gas transport and mixing or to get information about the local thermo-dynamical state. To be able to realize the environmental conditions present in these combustion chambers in the laboratory, heated, optically-accessible high-pressure cells were utilized. Flows of nitrogen, carbon dioxide, or an oxygen-nitrogen-mixture and a few vol% of the aromatics were investigated spectroscopically. Absorption spectra were measured with a deuterium lamp or Nd:YAG laser. Fluorescence information was determined by exciting the species with a frequency-converted picosecond Nd:YAG laser and the laser-induced fluorescence (LIF) was measured spectrally and temporally resolved by a fast photomultiplier or a spectrometer coupled with a streak camera. The investigated tracers differ in their photophysical properties and therefore vary in their applicability for specific measurement techniques.

The core of this dissertation consists of four publications as well as some unpublished results. One of these publications results from a collaboration of three researchers of our department and is dealing with the principle of self-quenching, giving insight into origin and the interrelationship between the base deactivation pathways for excited states. The experiments of the other three publications have been planned, carried out, analyzed and published (mostly) by myself. They all provide fundamental photophysical properties of selected aromatic compounds for various environmental conditions and also give phenomenological fitting functions with which the estimated signal intensity per molecule for internal combustion engine relevant temperatures and pressures can be calculated. As unpublished results, the absorption cross-section of anisole and the fluorescence spectra and lifetime of 1-methylnaphthalene in dependence on the environmental conditions fill gaps in the dataset of these tracers. A comparison of all fluorescence tracers investigated here and several that had been investigated before is made to give an overview, to enable tracer selection for specific applications, and to put the results of this dissertation into perspective.

Zusammenfassung

Diese Dissertation basiert auf Experimenten zur Bestimmung der photophysikalischen Eigenschaften der Aromaten Toluol, 1,2-Xylol, 1,2,4-Trimethylbenzol, Anisol, 1,4-Difluorbenzol, Naphthalin und 1-Methylnaphthalin unter verschiedenen Umgebungsbedingungen. Die meisten dieser Spezies sind Teil von kommerziellen Brennstoffen wie Kerosin, Benzin oder Diesel oder haben ähnliche physikalische Eigenschaften. Daher werden ihre photophysikalischen Eigenschaften für laserbasierte Messungen in Verbrennungsmotoren und Gasturbinen verwendet, um entweder Spezies-transport und -mischung zu visualisieren oder thermodynamische Informationen zu erhalten. Um die in diesen Verbrennungskammern vorhandenen Umgebungsbedingungen im Labor untersuchen zu können, wurden heizbare, optisch zugängliche Hochdruckzellen verwendet. Sie wurden mit Stickstoff, Kohlenstoffdioxid oder einer Sauerstoff-Stickstoff-Mischung durchspült, die wenige Vol.-% der Aromaten enthielten. Die Absorptionseigenschaften wurden mithilfe einer Deuteriumlampe oder eines Nd:YAG-Lasers gemessen. Die Fluoreszenzinformation wurde durch Anregen des Messvolumens durch einen ins Ultraviolette frequenzkonvertierten Pikosekunden-Nd:YAG-Laser gewonnen und die laserinduzierte Fluoreszenz (LIF) wurde spektral und zeitlich aufgelöst durch einen schnellen Photovervielfacher oder eine Spektrometer-gekoppelte Streackamera gemessen. Die untersuchten Spezies unterscheiden sich in ihren jeweiligen photophysikalischen Eigenschaften und sind daher für verschiedene Messtechniken unterschiedlich gut geeignet.

Der Kern dieser Dissertation besteht aus vier Publikationen sowie einigen nicht veröffentlichten Ergebnissen. Eine dieser Veröffentlichungen basiert auf einer Zusammenarbeit von drei Mitgliedern unserer Arbeitsgruppe und befasst sich mit Selbstlöschung des angeregten Zustandes. Diese Arbeit zeigt den Ursprung dieses Effektes und die Zusammenhänge zwischen den einzelnen Deaktivierungspfaden. Die Experimente, auf denen die drei anderen Veröffentlichungen basieren wurden (größtenteils) von mir alleine geplant, durchgeführt, ausgewertet und zusammengefasst. Sie geben allesamt bisher nicht veröffentlichte photophysikalische Messgrößen verschiedener aromatischer Verbindungen unter einem breiten Spektrum wechselnder Umgebungsbedingungen wieder. Außerdem werden phänomenologische Funktionen vorgestellt, mit denen die Fluoreszenzintensität pro Molekül unter Verbrennungsmotor-relevanten Bedingungen vorhergesagt werden kann. Als nicht publizierte Ergebnisse runden der Absorptionsquerschnitt von Anisol und die Fluoreszenzlebensdauer in Abhängigkeit von den Umgebungsbedingungen von 1-Methylnaphthalin die Ergebnisse ab, die bisher vorhandene Lücken in der Dokumentation dieser Spezies schließen. Ein Vergleich aller hier untersuchten sowie einiger bereits zuvor beschriebener Fluoreszenztracer ermöglicht die Auswahl von Tracern für bestimmte Anwendungen und setzt die neuen Ergebnisse in einen größeren Kontext.

Table of contents

Summary	2
Zusammenfassung	3
Table of contents	4
1 List of abbreviations	7
2 Introduction	9
3 Background	12
3.1 Motivation.....	12
3.2 Commonly used fluorescence tracers	12
3.3 Typical applications of tracer-LIF diagnostics	21
3.3.1 Measurement of fuel/air ratio	21
3.3.2 Thermometry with organic tracers.....	21
3.3.3 Measurements of combined volatility classes of multi-component fuels.....	22
3.3.4 Diagnostics based on the fluorescence lifetime.....	23
4 Theoretical background – photophysics of organic molecules	24
4.1 Absorption	24
4.1.1 Classification of electronic transitions.....	24
4.1.2 Classification of electron states into different classes	25
4.2 Deactivation of excited states in molecules.....	26
4.2.1 Fermi's golden rule	27
4.2.2 Radiative processes.....	27
4.2.3 Fluorescence spectra of aromatic molecules	27
4.2.4 Non radiative processes	28
4.3 Quantum yield and fluorescence lifetimes	30
4.3.1 Fluorescence quantum yield	30
4.3.2 Natural and effective lifetime	30
4.4 Quenching.....	32
4.4.1 Stern-Volmer behavior for collisional quenching	32
4.4.2 Electronic energy transfer.....	34
4.4.3 Fluorescence quenching by molecular oxygen.....	35
4.4.4 Self-quenching	35
4.5 Fluorescence model development.....	36
4.5.1 Average thermal energy level (ATEL)	36
4.5.2 Energy dependent transition rate constants	36

4.5.3	Photo-induced cooling	37
4.5.4	Step-ladder model	38
5	Published and unpublished research	40
5.1	Low-pressure effective fluorescence lifetimes and photophysical rate constants of one- and two-ring aromatics	42
5.1.1	Introduction.....	42
5.1.2	Theoretical background	45
5.1.3	Experiment and data evaluation.....	47
5.1.4	Data analysis	47
5.1.5	Results.....	47
5.1.6	Discussion.....	52
5.1.7	Conclusions.....	54
5.2	Self-quenching in toluene LIF	55
5.2.1	Introduction.....	55
5.2.2	Experiment.....	59
5.2.3	Results.....	62
5.2.4	Conclusions.....	66
5.3	UV absorption and fluorescence properties of gas-phase p-difluorobenzene	68
5.3.1	Introduction.....	68
5.3.2	Theoretical background	70
5.3.3	Experiment.....	70
5.3.4	Data Evaluation	73
5.3.5	Results.....	75
5.3.6	Discussion.....	81
5.3.7	Conclusions.....	81
5.4	Temperature, pressure, and oxygen quenching behavior of fluorescence spectra and lifetimes of gas-phase <i>o</i> -xylene and 1,2,4-trimethylbenzene	83
5.4.1	Introduction.....	83
5.4.2	Theoretical background	85
5.4.3	Experiment.....	86
5.4.4	Date evaluation	88
5.4.5	Results.....	91
5.4.6	Discussion.....	102
5.4.7	Conclusions.....	103
5.5	Unpublished results	105
5.5.1	Anisole absorption cross-section	105
5.5.2	1-Methylnaphthalene fluorescence	106
6	Potential LIF tracer data summary	110
7	Conclusions.....	114

8	List of references.....	113
	Acknowledgement	124

1 List of abbreviations and symbols

ATEL	Average thermal energy level
CCD	Charge-coupled device
DCA	Degree crank angle
DFB	1,4-Difluorobenzene
dV_c	Detection volume (m^3)
ϕ_{fl}	Fluorescence quantum yield
ϕ_{rel}	Relative fluorescence quantum yield
E	Energy ($\text{kg m}^2\text{s}^{-2}$)
FARLIF	Fuel/air-ratio LIF
h	Planck's constant (Js)
\hbar	Reduced Planck's constant ($h/2\pi$; Js)
\hat{H}'	Hamilton operator responsible for the transition
η_{opt}	Detection efficiency
I	Intensity (kg s^{-3})
I_{laser}	Intensity of the incident laser beam (kg s^{-3})
I_{LIF}	Intensity of the detected LIF signal (kg s^{-3})
IC	Internal conversion
IC	Internal combustion
ISC	Intersystem crossing
k_{fl}	Fluorescence rate (s^{-1})
k_{IC}	Rate of internal conversion (s^{-1})
k_{ISC}	Rate of intersystem crossing (s^{-1})
k_{NR}	Non-radiative rate (s^{-1})
k_{q}	Quenching rate coefficient (s^{-1})
k_{SV}	Stern-Volmer coefficient
k_{tot}	Total depopulation rate (s^{-1})
λ	Wavelength (nm)
LIF	Laser-induced fluorescence
n	Number density (in m^{-3}) of molecules in the gas phase
n_{q}	Number density of a quenching species (in m^{-3})
ν	Frequency (s^{-1})
p	Total pressure (bar)
\mathbf{p}_M	transition dipole moment of state M

P_n	Transition probability
p_{O_2}	O ₂ partial pressure (bar)
σ_{abs}	Absorption cross-section (in cm ²)
S_{fl}	Fluorescence signal
T	Temperature (K)
TL	Toluene
TMB	1,2,4-Trimethylbenzene
τ	Fluorescence lifetime (ns)
τ_{eff}	Effective fluorescence lifetime (ns)
τ_{fl}	Natural lifetime (ns)
UV	Ultra violet region of light, $\lambda < 400$ nm
UV/Vis	Ultra violet / visible region of light, $\lambda < 700$ nm
VR	Vibrational relaxation
Ψ_n	Wave function of state n
XL	1,2-Xylene
1MN	1-Methylnaphthalene

2 Introduction

In today's world, the impact that fossil fuels used for power generation, heating and transportation such as coal, oil, and gas are constantly on the news. At the same time, these resources are becoming scarcer and prices are steadily increasing. The use of renewable energies would be optimal. However, since these are not yet economical, not available in sufficient (constant) quantity, and difficult to use for transportation, we will still depend on fossil fuels for many years to come. Therefore, it is becoming increasingly important to deal efficiently with these resources. To improve the efficiency of combustion processes, e.g., in internal combustion (IC) engines and gas turbines, it is necessary to understand what is happening at or immediately before ignition and at which pressures and temperatures these effects occur. For this purpose, a method is required, with which these parameters can be recorded during operation. Optical measurement techniques offer the advantage that they are non-contact and thus do not affect the system. Therefore, the real behavior of the reactive system can be well monitored and understood. Various optical diagnostics methods have been developed in the past, e.g., light absorption or scattering [1] (see chapter 3.3). Another frequently used method for the investigation of gases or liquids is laser-induced fluorescence (LIF), in which the substance to be investigated (for example the fuel) is excited with a laser and fluoresces in a characteristic wavelength range [2-4]. If this emission shows a temperature and/or pressure dependence, these parameters potentially can be measured alongside the concentration of the fluorescing species.

Commercial fuels, e.g., gasoline, show broad and unstructured fluorescence spectra, originating from many different species present in the mixture. Another problem is the lack of reproducibility of the emission characteristics (temporally as well as spectrally), since the composition of the fuel varies widely and is influenced by uncontrollable factors, e.g., the oil source or the processing plant. Quantitative fluorescence measurements with commercial fuels are therefore only possible in few specific cases [4, 5].

In this context, so-called molecular tracers come into play. Suitable tracers are substances that have well-characterized fluorescence properties. For the most realistic measurements, a tracer is chosen that differs as little as possible in properties such as vapor pressure, viscosity, diffusion, and combustion properties from those of the real fuel, so that the physical behavior, e.g., the evaporation characteristics are not altered significantly. It is then added in low concentrations to an otherwise non-fluorescent surrogate fuel (e.g., iso-octane) and evaporated, e.g., via a nozzle. After laser excitation the fluorescence signal of the tracer can give information on local temperature, the air/fuel ratio (see chapter 3.3) or simply visualize the propagation of the surrogate fuel. For this, a reliable set of calibration data for the tracer in the gas-phase for known environmental conditions is essential.

Many substance classes can serve as tracers, inorganic as well as organic molecules. In general, there is no universal tracer. The use always depends on the application and the parameter range of interest. Nitric oxide (NO), for example, is a well-studied gaseous tracer with high fluorescence

intensities, but it is toxic and corrosive. The aromatics (organic molecules) investigated in this work are inexpensive and are in large fractions part of commercial fuels and thus, within certain limits, do not alter the behavior of surrogate fuel in comparison to real fuel [4].

In addition, it is also important for a tracer that excitation and detection are experimentally simple. For most aromatic tracers, both conditions are fulfilled since they can be electronically excited with typical UV lasers (for example with a frequency-quadrupled Nd:YAG laser) and the fluorescence is detectable with typical camera systems (e.g., CCD). Toluene is often used as a tracer for gasoline, while for Diesel or kerosene, which are less volatile than gasoline, naphthalene is a popular candidate. One of the most important parameters of tracers are the fluorescence quantum yield (ϕ_{fl}) and the fluorescence spectrum and their dependence on temperature. These parameters and their dependences are unique and give each tracer an individual “footprint”. The ϕ_{fl} is the ratio of the number of absorbed and emitted photons. Especially in the case of aromatic tracers, the increasing O₂ content of the buffer gas leads to a strong quenching of the fluorescence signal. There are pros and cons to this effect. On the one hand, the ϕ_{fl} and thus the signal intensity is strongly reduced and the temperature dependence decreases. On the other hand, the changing ϕ_{fl} can also provide information on the mixing ratio of fuel and oxygen. Measuring this quantity is of interest, as it gives direct information on the degree of mixing on the molecular scale, which affects the combustion efficiency. In most cases, it is not necessary to determine absolute quantum yields but relative quantum yields based on a calibration point, e.g., 296 K, 1 bar with N₂ as buffer gas. In this context, the measurement of the fluorescence lifetime offers an interesting alternative to measurements of signal intensities. It is known from literature that the fluorescence lifetime is proportional to the quantum yield [6, 7] (see chapter 4.3), which makes the former a quantity, which mirrors this quantum-yield dependence.

As mentioned, temperature and oxygen concentration also have an influence on the fluorescence spectrum, which becomes visible in a redshift of the spectrum as well as a changed shape, e.g., less structure. The total pressure and the excitation wavelength also have an effect on both, the fluorescence spectra and the ϕ_{fl} (fluorescence lifetime). This results in a very broad range of parameters which must be determined over a large range since the environmental conditions in an IC engine also change by order of magnitudes. Providing such data, which are necessary for quantitative tracer-LIF diagnostics, for a number of different aromatic tracer species is the aim of this work. Since it is quite difficult to make use of the data alone, with all the parameters and different dependences, different forms of fluorescence models have been developed. The more sophisticated step-ladder model [8-10] demands a lot of additional input (e.g., rate constants for all deactivation pathways for each energy level of the ground and the excited state) and is therefore quite hard to put together. A semi-empirical approach [11], where the collected data is fitted with reasonable functions for all parameters which are then combined into one formula has proven to be as effective, if one is interested in the estimated signal intensities rather than the physical process of fluorescence. Since the necessary rate-constant data for the tracers that have been characterized in this work is not published yet, the latter approach is used in this work.

This thesis is structured as follows: In chapter 3, a short motivation is given in the form of an overview of the background of literature, consisting of previous work and practical applications, followed by an introduction into the underlying theory in chapter 4. The resulting publications that represent the main body of this dissertation are given in chapter 5. In addition, unpublished work that is worth mentioning is presented in this chapter. Chapter 6 provides a summary for potential LIF tracer and chapter 7 summarizes the work.

3 Background

3.1 Motivation

It is crucial to improve practical combustion processes to make the most out of the remaining fossil energy resources. With optical measurement methods, a lot of aspects of these processes can be investigated, e.g., visualization of gas mixing, determination of local fuel/oxygen ratios and temperature. Accurate knowledge of the composition of the fuel mixtures, for example before the ignition in an internal combustion engine, plays an important role. Optical measurement methods, such as laser-induced fluorescence (LIF) used here are especially suitable because they are non-contact techniques that do not interact with the combustion process. In order to be able to use these diagnostics to measure, e.g., temperature or fuel concentration, in an internal combustion engine or in gas turbines, photophysical data for the respective species must be available for the entire range of environmental conditions. Laser-induced fluorescence is the spontaneous radiation emitted after (usually pulsed) laser excitation. Since the typical time scale for the spontaneous emission is 0.1–150 ns, with pulsed excitation it is possible to generate snap-shot images even of rapidly changing processes. The fluorescence signal in general depends on

$$S_{\text{fl}} = \frac{E}{h\nu} \eta_{\text{opt}} dV_c n \sigma_{\text{abs}} \phi_{\text{fl}}, \quad (1)$$

with the photon flux density $\frac{E}{h\nu}$, the system-dependent factor for losses in the detection system η_{opt} , the detection volume dV_c , the number density of the fluorescent molecule n , and the molecular absorption cross-section (σ_{abs}) and the fluorescence quantum yield (ϕ_{fl}).

Two parameters are crucial for the LIF process. On the one hand, it is the σ_{abs} of the fluorescent species, which is a measure of the likelihood of absorption and thus excitation of the molecule. On the other hand, there is the ϕ_{fl} , which represents the ratio of emitted vs. absorbed photons. The intensity of the LIF signal is decisively determined by these two factors. Both are experimentally measurable, in the case of the σ_{abs} , e.g., with an absorption spectrometer, but since they depend on the excitation wavelength as well as the temperature and in case of the ϕ_{fl} also of the total pressure and the oxygen partial pressure, they describe a complex relationship. These processes are explained in more detail in chapter 4.

3.2 Commonly used fluorescence tracers

Commercial fuels such as kerosene, gasoline, or Diesel are mixtures of a wide variety of substances, many of them absorbing in the UV and subsequently emitting fluorescence. They therefore show a spectrally broad fluorescence signal after optical excitation (Figure 1). In commercial fuels, the constituent mole fractions vary from sample to sample, therefore, only qualitative measurements, e.g., the investigation of the composition of the fuel sample by analyzing the spectrum

in different wavelength ranges, can be performed on such mixtures as shown in Figure 1. If one is interested in the combustion phase, one could also make use of intermediate species arising during or after combustion, e.g., OH or NO, which can again fluoresce through excitation in the species specific excitation wavelengths. If only one single species is responsible for the fluorescence in a given spectral range, quantitative measurements are possible again.

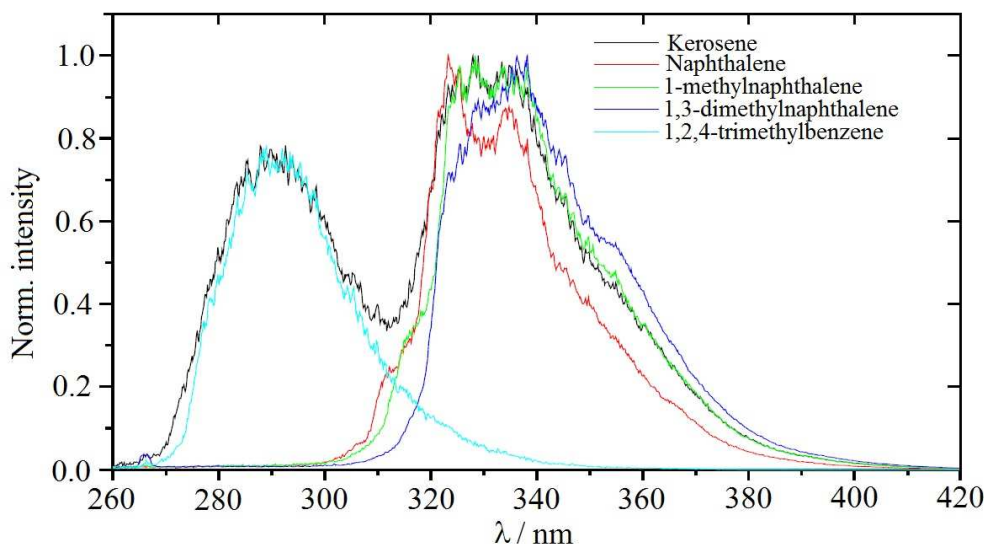


Figure 1: Peak-normalized fluorescence spectrum of kerosene (black curve), excited with 266 nm at 445 K and in 1 bar N_2 , as well as spectra of some aromatics occurring in kerosene [12].

Another approach is to add a small amount (a few vol%) of a single fluorescent species (a so-called tracer) to a non-fluorescent surrogate fuel. This way the resulting fluorescence signal can be unambiguously assigned, it is thus possible to obtain quantitative LIF measurements (such as concentration or temperature) for known external conditions, e.g., pressure and temperature. The choice of a suitable tracer depends on the thermochemistry and the thermophysical properties of the system under consideration, which should differ as little as possible from the actual fuel. In addition, it would be advantageous if the tracer had as little influence on combustion of the main fuel as possible. These limitations still allow for many substances and material classes. They include single atoms (e.g., krypton), small inorganic molecules (e.g., NO), various ketones (e.g., acetone) and aromatics (e.g., toluene). The tracers studied in this work all belong to the class of aromatics. These can all be electronically excited with standard laser sources, are readily available and only little to non-toxic. In Figure 2 and Table 1, all aromatic tracers used in this Thesis and some of their thermodynamic properties are briefly presented.

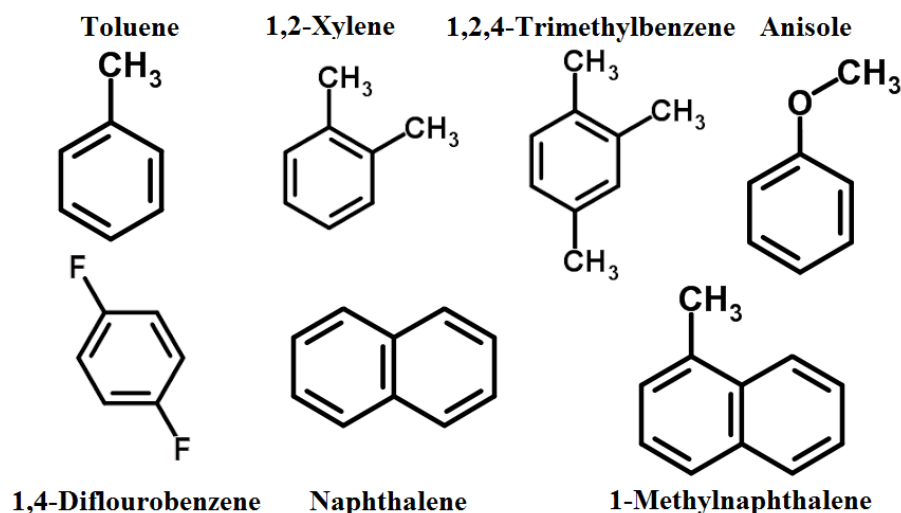


Figure 2: Structure of the investigated aromatic species

Table 1: Selected thermodynamic properties of the investigated aromatic species [13].

	Chemical formula	Molar mass / (g/mol)	Melting point / K	Boiling point / K	Density at 293 K / (g/cm³)	Vapor pressure at 298 K / mbar
Toluene	C ₇ H ₈	92.14	178	384	0.87	28
1,2-Xylene	C ₈ H ₁₀	106.16	248	417	0.88	8.8
1,2,4-Trimethylbenzene	C ₉ H ₁₂	120.19	229	443	0.88	2.8
Anisole	C ₇ H ₈ O	108.14	236	427	0.995	4.72
1,4-Difluorobenzene	C ₆ H ₄ F ₂	114.1	260	361	1.11	84.8
Naphthalene	C ₁₀ H ₈	128.17	351	491	1.025	0.086
1-Methylnaphthalene	C ₁₁ H ₁₀	142.2	251	514	1.001	0.089

In the following, a brief review of some important publications related to LIF of the aromatics considered here, as well as some of their applications will be presented.

Toluene (TL):

The fluorescence of toluene has been studied since 1929 [14, 15]. It is often used as a fluorescence tracer because its photo physical properties have been studied quite well and its evaporation characteristic match well with those of gasoline. Due to its high fluorescence quantum yield (see below) and high vapor pressure, even at low temperatures, gas mixing processes can be visualized. Figure 3 (left) shows the absorption spectra in the gas phase for temperatures up to 1128 K [16]. The fluorescence spectrum between 240 and 270 nm at room temperature shifts to higher wavelengths with increasing temperature. At the same time, the entire spectrum broadens and the fine structure disappears. Both KrF* excimer (248 nm) and frequency-quadrupled Nd:YAG lasers (266 nm) can be used for excitation. While the absorption cross-section (σ_{abs}) remains almost con-

stant at 248 nm with increasing temperature, it rises at 266 nm (Figure 3, right) [16].

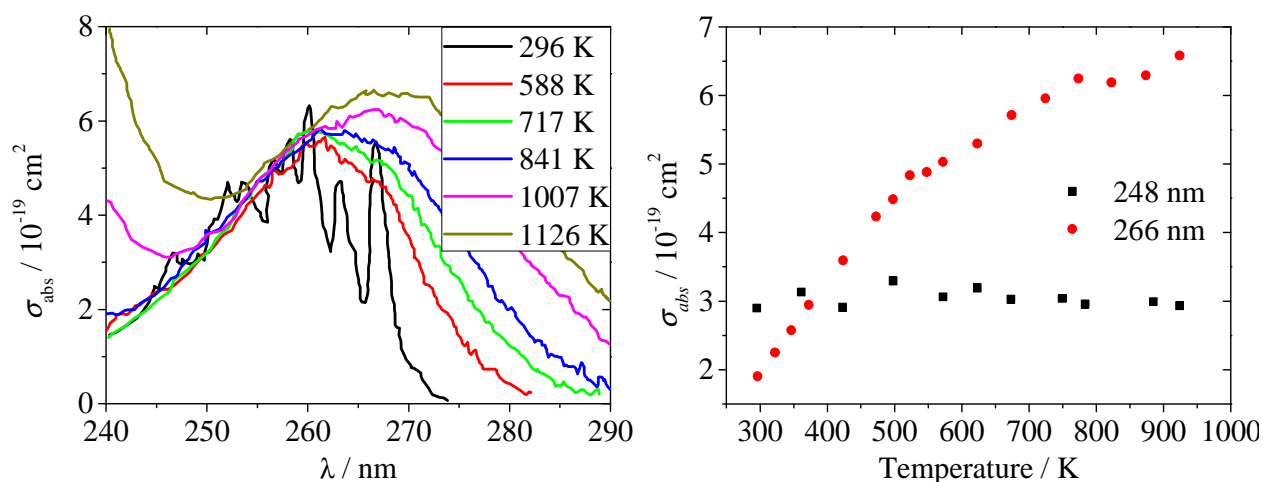


Figure 3: Toluene absorption spectra for various temperatures in 1 bar N_2 (left) and toluene σ_{abs} for laser excitation at 248 and 266 nm as a function of temperature (right); Data from Koban et al. [16].

At room temperature, the fluorescence ranges from 270 to 320 nm with a peak at 285 nm. The ϕ_{fl} in this range is relatively high (0.3) compared to other substance classes, e.g., ketones [17]. As the temperature increases, the fluorescence spectra shift to longer wavelengths with 2 nm / 100 K, while its width also increases (Figure 4, left) [10, 16]. This change in the range and shape of the spectrum allows the temperature to be measured by two-color thermometry (see section 4.3) [18, 19]. A similar but somewhat weaker effect is shown with excitation at 248 nm and increasing O_2 partial pressure (Figure 4, right). The red-shift is more pronounced at smaller partial pressures and saturates at about 200 mbar O_2 [20]. A similar two-color detection can be carried out, as with the temperature, by which O_2 concentration distributions can be measured [21].

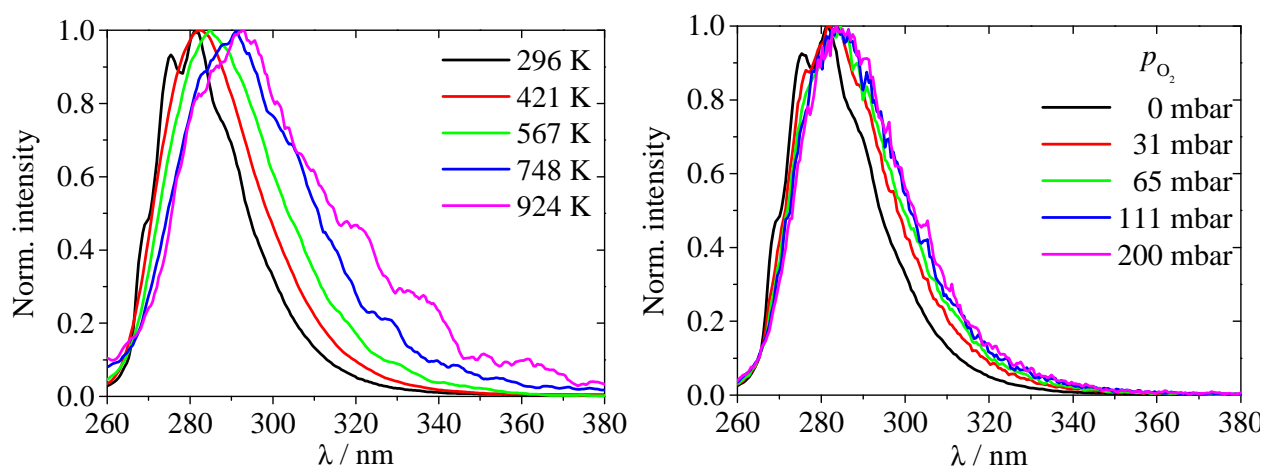


Figure 4: Normalized toluene fluorescence spectra for various temperatures after excitation at 248 nm (left, Koban et al. [16]) and various O_2 partial pressures at room temperature after excitation at 248 nm (right, Koban et al. [20]). Similar data has been reported for excitation with 266 nm by Faust et al. [22, 23].

The ϕ_{fl} of toluene also depends on temperature. It is reduced by three orders of magnitude with a temperature change from room temperature to 950 K. The decrease is more pronounced for excitation with 248 nm than for 266 nm (Figure 5, left) [10, 16], which is mainly used for one-color di-

agnostics of temperature measurements [24]. Koban et al. have developed a model [16] that was subsequently extended to include quenching effects by molecular oxygen [20] at 1 bar total pressure. Since the absolute ϕ_{fl} is known for room temperature (0.3 for 266 nm and 0.09 for 248 nm [17]), an absolute calibration of the temperature dependence could be carried out by Burton and Noyes [17]. Since their data was measured at low pressure (~ 22 mbar pure toluene) and the total pressure has a varying influence on the quantum yield, these values need to be adapted for atmospheric pressure.

The influence of total pressure on the ϕ_{fl} was less frequently investigated. Rossow showed a decrease of the quantum yield after excitation with 266 nm by 82% at 450 K and 74% at 700 K when pressure increases from 1 to 30 bar [10]. Cheung, on the other hand, noticed no pressure influence at room temperature for 266 nm [25], while excitation at 248 nm resulted in a slight increase [5, 25, 26]. Systematic investigations as well as an explanation for this are given in chapter 5.1.

The fluorescence of toluene (like that of many aromatics) is quenched by molecular oxygen. This effect is explained in chapter 4.4. Figure 5 (right) shows this strong influence of an increasing O_2 partial pressure at 1 bar total pressure [10, 20] along with model-based simulations from Koban for 248 nm excitation [16].

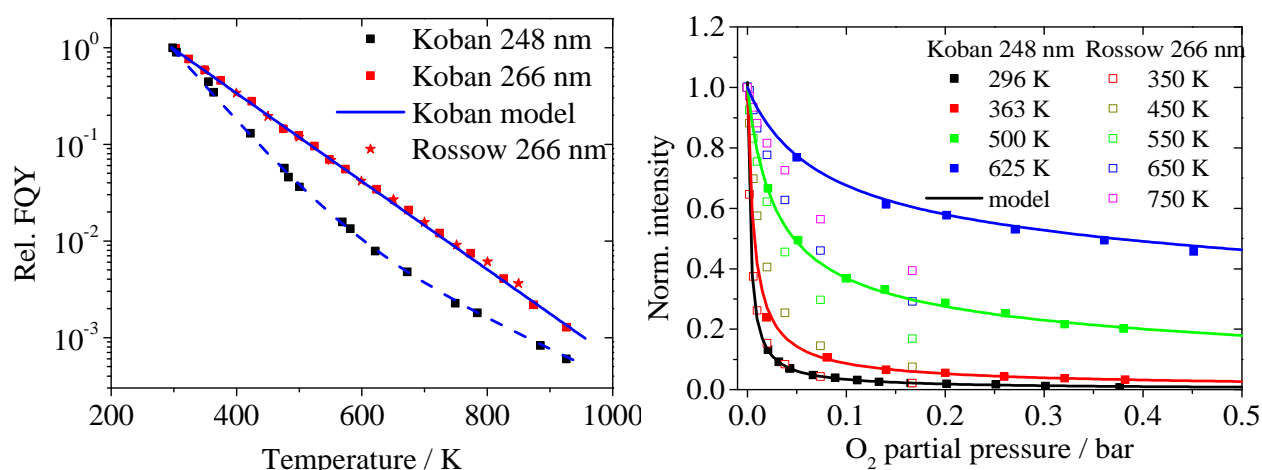


Figure 5: Left: Temperature dependence of the relative ϕ_{fl} for excitation at 248 and 266 nm (Koban et al. [16], Rossow [10]) in comparison to the simulated relative ϕ_{fl} for 248 and 266 nm (Koban et al. [20]). Right: Variation of the ϕ_{fl} with O_2 partial pressure for 248 and 266 nm excitation compared to the simulated relative ϕ_{fl} for 248 and 266 nm excitation (Koban et al. [20], Rossow [10]).

While many studies have investigated time-integrated fluorescence intensities under variable environmental conditions, the lifetime of the excited S_1 state has been measured less often. Lifetime measurements give a direct access to relative variations of the fluorescence quantum yield (see chapter 5.3.2) and are independent from experimental effects that influence the total signal intensity, such as variations in tracer concentration, laser pulse energy, signal trapping, or window transmission. Zimmermann et al. [27] investigated the fluorescence lifetime at 1 bar total pressure as a function of temperature and O_2 partial pressure after 248 nm excitation. For 266 nm excitation, there exist studies at room temperature (or below), at low pressures (around 13.3 mbar and

lower) [28-31], or in air at 1 bar [32]. More recently, Faust et al. extensively characterized the temperature, total pressure and O₂ partial pressure dependence of the fluorescence lifetime for 266 nm excitation [22, 23] (Figure 6), and Friesen et al. showed that with the fluorescence lifetime of toluene, the temperature in an internal combustion engine can be measured [33, 34].

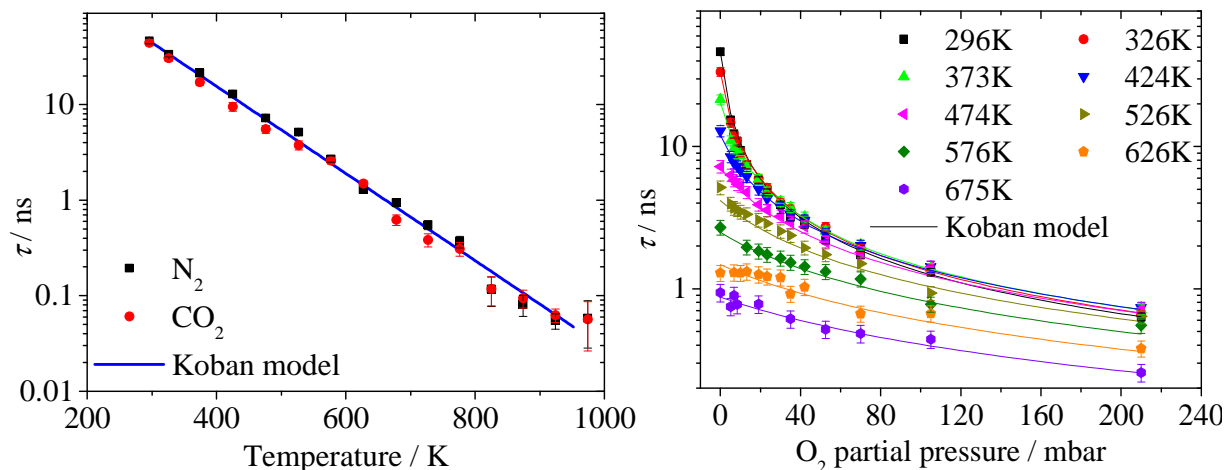


Figure 6: Left: Temperature dependence of the effective fluorescence lifetime for 266 nm excitation in comparison to the simulated relative ϕ_{fl} for 266 nm (Koban et al. [20]). Right: Variation of the effective fluorescence lifetime with oxygen partial pressure for 266 nm excitation compared to the modeled relative ϕ_{fl} for 266 nm (Koban et al. [20]).

1,2-Xylene

Until recently, little has been known about the fluorescence of 1,2-xylene (*o*-xylene, 1,2-dimethylbenzene). Its σ_{abs} at room temperature was investigated by Etzkorn et al. [35] and Fally et al. [36] and the S₀→S₁ absorption band was found to be spectrally located in between that of toluene and 1,2,4-trimethylbenzene. Since this compound is also present in commercial fuels and has a higher boiling point compared to toluene, further information on this tracer is relevant and will be presented in chapter 5.4.

1,2,4-Trimethylbenzene

An attractive tracer that has rarely been characterized is 1,2,4-trimethylbenzene [37]. At room temperature, its fluorescence spectrum is shifted by 10 nm to the red compared to toluene and its temperature-dependent red shift is somewhat stronger. On the other hand, the temperature dependence of the FQY in N₂ is comparable to that of toluene. The higher boiling point and thus lower vapor pressure compared to toluene make it a possible tracer for less volatile fuels, e.g., Diesel or kerosene. 1,2,4-trimethylbenzene is one of the substances responsible for the fluorescence spectrum of kerosene (Figure 1, [12]). Orain et al. [37] and Rossow [10] have investigated the σ_{abs} , the temperature dependence of the ϕ_{fl} at atmospheric pressure, as well as the total pressure dependence of the fluorescence at two temperatures. In this thesis, further data on the ϕ_{fl} and the σ_{abs} as well as semi empirical models for temperature, total pressure and oxygen quenching is presented in chapter 4.4.

Anisole

Anisole (methoxybenzene) has made an impact in the last years as promising tracer alternative to toluene. It is non-toxic and non-carcinogenic, making it an attractive alternative to other aromatic tracers. Although its chemical structure is very similar to that of other aromatic components, it is not contained in commercial fuels. Its fluorescence was first investigated in 1924 [38] and Hirasawa et al. have already discussed the possible use as a tracer in gaseous flows [39]. Anisole shows strong absorption at 266 nm with an σ_{abs} of $\sim 3 \times 10^{-18}$ at room temperature (decreasing for higher temperatures), as measured by Zabeti et al. in a shock tube [40]. Their work will be complemented by moderate temperature flow-cell measurements in chapter 5.5. The fluorescence spectrum of anisole ranges from 270 to 360 nm with a maximum at 290 nm [41] (Figure 7, left). Faust et al. have also studied its fluorescence lifetime with respect to temperature, total pressure (both Figure 7, right) and O_2 quenching and have developed a phenomenological fluorescence model to predict these dependences [41]. On a per-molecule basis, the higher absorption cross-section leads to a considerable signal improvement under otherwise identical conditions compared to toluene as shown by Faust et al. [42].

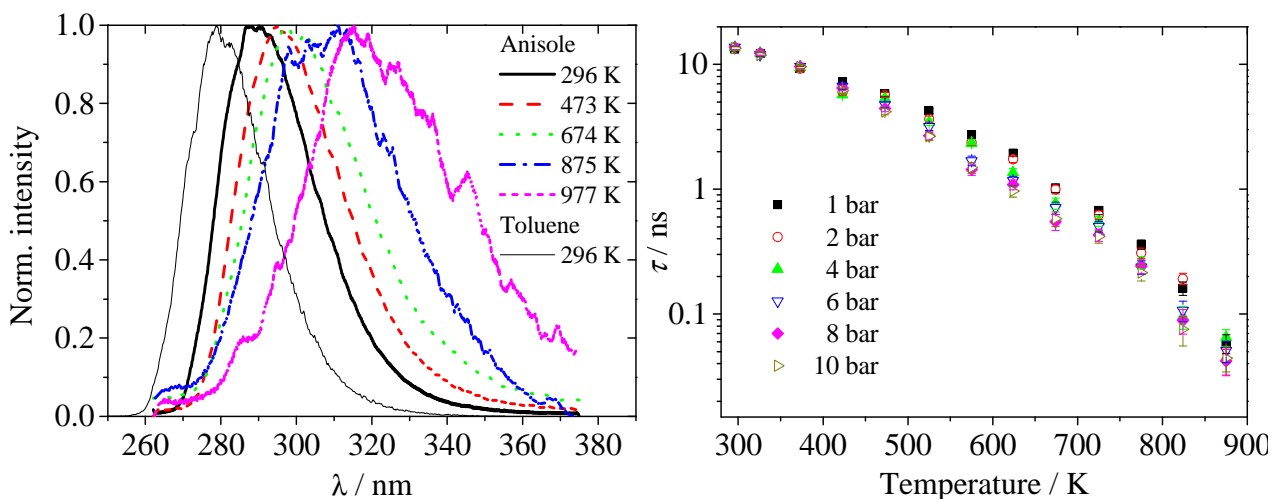


Figure 7: Left: Normalized anisole fluorescence spectra for various temperatures after excitation at 266 nm [41]. Right: Temperature and total pressure dependence in N_2 of the effective fluorescence lifetime for 266 nm [41].

p-Difluorobenzene

A very promising tracer for high volatility class fuels is *p*-difluorobenzene. The reported σ_{abs} and ϕ_{fl} by Volk et al. [43] and its high vapor pressure (84.8, see Table 1) hint at the potential signal increase compared to toluene that this tracer possesses. One drawback of this species is the potential formation of hydrofluoric acid during combustion. Nevertheless, this tracer has already been used (together with 1-methylnaphthalene) in applications to visualize preferential evaporation phenomena during spray evaporation by Itani et al. [44]. The basic characterization of this tracer species for such application including σ_{abs} , ϕ_{fl} , and a semi-empirical model can be found in chapter 5.3.

Naphthalene

Although the earliest studies on the basic photo physical properties of naphthalene were conducted more than a hundred years ago (e.g., [6, 45-50] and references therein), it is still used as commonly as toluene. Its evaporation properties resemble those of the low-volatility components of Diesel or kerosene, because it (or close derivatives of it) make up a large fraction of these commercial fuels. Naphthalene is solid at room temperature and is often dissolved in a liquid before it is brought into the gas phase by evaporation. The fluorescence properties of naphthalene under engine-relevant conditions were described by Orain et al. [51]. Previous studies were done in a restricted temperature range [52] or in pure nitrogen at 1 bar total pressure [6].

Absorption spectra of naphthalene have been published only at low temperatures, i.e., for 313 K, where significant absorption takes place between 240 and 280 nm [53]. However, the σ_{abs} shows no dependence on the temperature between 350 and 900 K when excited at 266 nm [10]. Measured fluorescence intensities can therefore be interpreted in a good approximation as relative ϕ_{fl} .

At 350 K, the fluorescence spectrum of naphthalene is in the range 300–400 nm with a maximum at 335 nm (Figure 8, left). The red-shift of the spectrum with temperature is somewhat stronger (5 nm / 100 K) than with toluene (2 nm / 100 K, see Figure 4). The same applies to the red-shift as a function of O_2 partial pressure (Figure 8, right). While two-color thermometry for naphthalene is used in applications similar to toluene [9], no attempt for monitoring the O_2 partial pressure by two-color detection has yet been published.

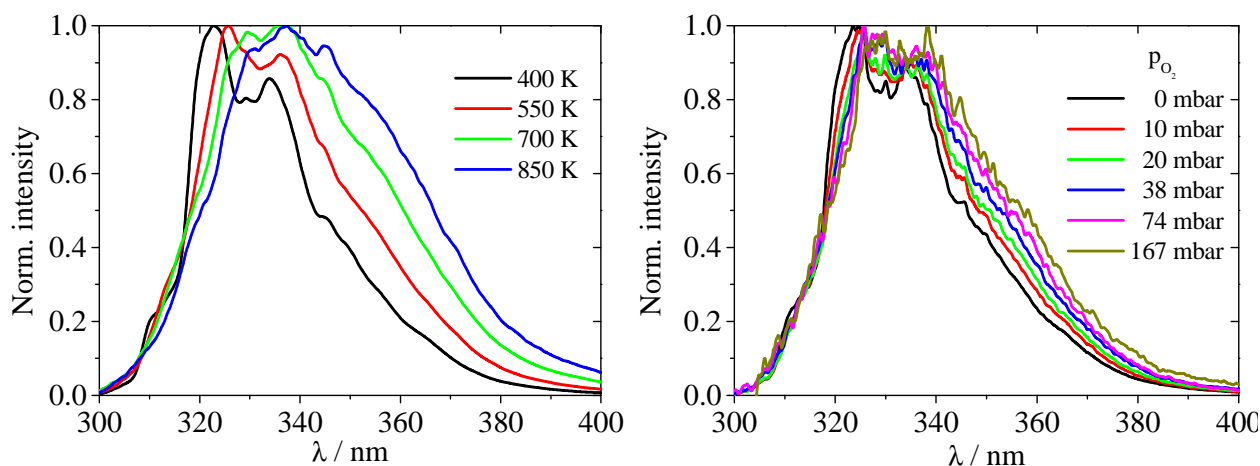


Figure 8: Normalized naphthalene fluorescence spectra for various temperatures after excitation at 266 nm in 1 bar N_2 (left, Orain et al. [51]) and for various O_2 partial pressures at 450 K after excitation at 266 nm (right, Rossow [10]).

The temperature dependence of the ϕ_{fl} of naphthalene (Figure 9, left) is somewhat lower than for toluene (Figure 5, left) [6, 51]. A total pressure increase in the case of naphthalene leads to a slight increase in the ϕ_{fl} by 10%. This is in stark contrast to the pressure dependence of toluene where an increase in pressure decreases the ϕ_{fl} . This effect is discussed in chapter 5.1. Naphthalene fluorescence is also strongly quenched by O_2 (Figure 9, right). As with toluene, this effect decreases with increasing temperature, but is still prominent for high temperatures.

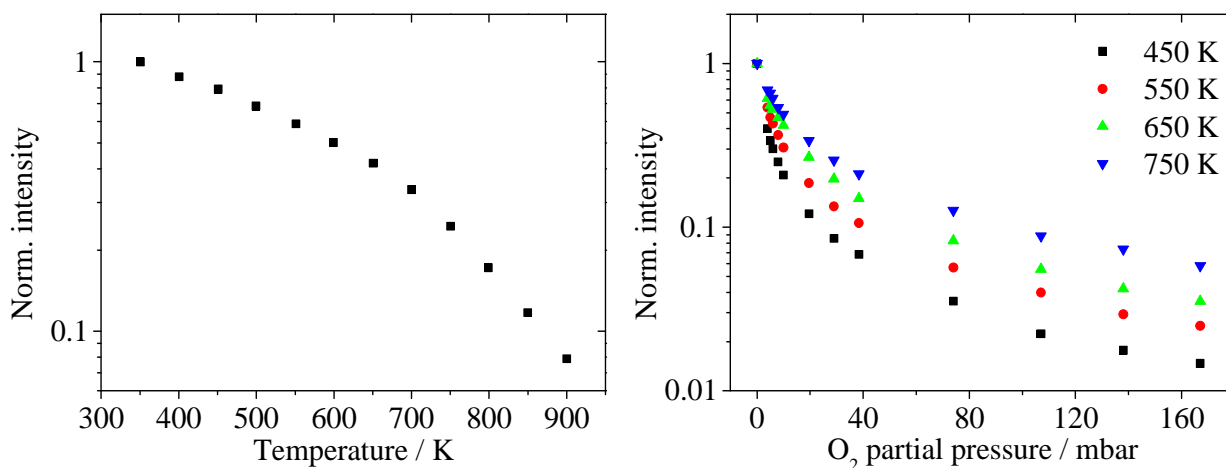


Figure 9: Temperature dependence of the relative fluorescence quantum yield at 1 bar N₂ (left, Orain et al. [51]) and with O₂ partial pressure at various temperatures at 1 bar total pressure (right, Rossow [10]).

Effective fluorescence lifetimes of naphthalene were studied by many groups. The first measurements were carried out mainly at low temperatures and low pressures [46]. Ni and Melton [54] and Ossler et al. [6] investigated naphthalene fluorescence lifetimes as a function of temperature at 1 bar N₂. The influence of O₂ and total pressure on the lifetime have been investigated by Faust et al. [23]. This work also presented a semi-empirical model for the fluorescence of naphthalene. Two lifetime components were observed by Ossler et al. [6] and Faust et al. [23] even at low temperatures with a third lifetime component being noticeable at higher temperatures only (see slope change in Figure 9, left). This is most probably related to the “third decay channel”, introduced by Jacon et al. [30]. In contrast to toluene, the fluorescence lifetime of naphthalene was investigated in gas flows [54] and standard burners [7], but only with the exclusion of O₂.

1-Methylnaphthalene

Despite the larger molar mass compared to naphthalene, 1-methylnaphthalene is liquid at room temperature, and therefore easier to handle. The fluorescence spectrum is slightly red-shifted (~4 nm) compared to naphthalene. There are very few studies on 1-methylnaphthalene fluorescence. Kaiser and Long showed a similar O₂ quenching behavior as for naphthalene for two temperatures [52]. 1-Methylnaphthalene is an important component of the fluorescence spectrum of kerosene and Diesel [12]. Similar to 1,4-difluorobenzene, 1-methylnaphthalene has been used for visualizing preferential evaporation effects as a surrogate for low-volatile fuel components [44]. Some additional data about the fluorescence lifetime and its dependence on temperature, pressure and oxygen partial pressure is provided in chapter 4.5.

3.3 Typical applications of tracer-LIF diagnostics

Laser-induced fluorescence using tracers offers a wide range of possible applications. In addition to the thermometry described in the following section, this includes, e.g., the determination of the air/fuel ratio or the visualization of spray injection. In most of these applications LIF imaging is used. For this purpose, the exciting laser beam is formed into a light sheet with typical dimensions of 20–30 mm height and 0.5 mm thickness. Optically-filtered fluorescence emission is then recorded at right angle by an intensified (and thus UV-sensitive) CCD camera.

3.3.1 Measurement of fuel/air equivalence ratio

In many practical applications, the local fuel/air ratio must be known for optimizing fuel/air mixing and thus the actual combustion process. This can be achieved in a similar way [21] as the two-color detection thermometry explained in the next section. Since the fluorescence of aromatics is strongly quenched by O_2 , the first assumption was that the fuel/air equivalence ratio is proportional to the fluorescence signal (fuel/air ratio LIF, FARLIF) [55, 56]. However, Koban et al. [11, 20, 57, 58] for toluene and Kaiser and Long [52] as well as Orain et al. [51] for 1-methylnaphthalene and naphthalene showed that this assumption is not justified in most practical cases and direct measurements of fuel/air ratios are more complex.

3.3.2 Thermometry with organic tracers

Thermometry, i.e., retrieving temperature information from some accompanying spectral feature variation are, besides the simple visualization of mixing processes, one of the most important tracer-LIF applications. This allows for example visualizing the temperature distribution during the compression stroke in an engine cylinder before ignition, which would deliver important information for the optimization of the subsequent combustion process. There are several temperature measurement methods available, therefore, here only the one- and two-color detection method mentioned above will be described.

Single-color thermometry uses the spectrally-integrated fluorescence intensity to determine the temperature according to calibration curves measured in flow cells [24]. In this case, toluene was used as a tracer with 248 nm excitation and the technique was used to measure temperature fluctuations due to wall interaction during the compression stroke of an IC engine. This method has a higher precision (below 4% precision error) compared to other forms of optical thermometry. However, it can only be used in homogeneous mixtures, where the signal variation can be attributed to temperature variation only (but not density and concentration variations). If this condition cannot be fulfilled, other approaches need to be used.

The two-color detection method (e.g., [59]) exploits the temperature dependence of the spectral intensity distribution that occurs with almost all aromatic tracers (Figure 10, left). The molecule is excited with a laser and the emission is measured in different spectral regions, e.g., with two different cameras or one camera equipped with an image doubler. The spectral regions are separated

via different filters that are placed between the camera and the measurement volume. The spectral ranges should be selected with regard to maximum temperature sensitivity in the ratio formation of the signal intensities (Figure 10, right). The advantages of this method are that the intensity ratio is independent from local variations in tracer concentration and that it is not influenced by laser fluctuations or uneven energy distributions in the laser light sheet. A disadvantage is the signal loss per channel due to the spectral filtering. Furthermore, this technique works only with aromatics, since only these show a shift of the spectrum with the temperature. Also, ratiometric measurements tend to increase the noise level of the measurement.

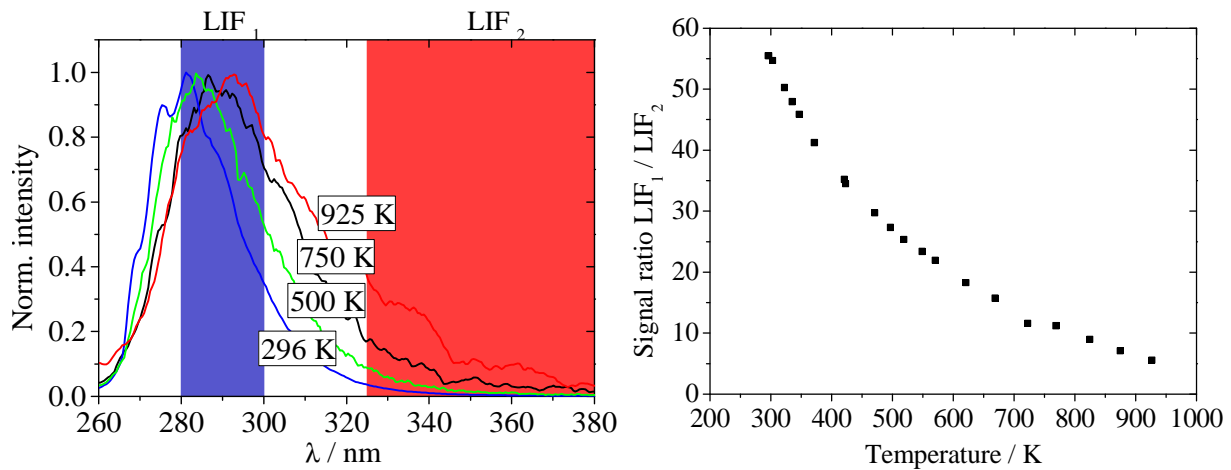


Figure 10: Fluorescence spectra of toluene for various temperatures after excitation with 248 nm (left) and the change of the signal ratio of LIF₁ (280–300 nm) / LIF₂ (325–380 nm) with temperature [58] (right).

3.3.3 Measurements of combined volatility classes of multi-component fuels

In most cases, the visualization of fuel/air mixing uses a single tracer only [4, 60]. Under certain operating conditions, this is a simplification because commercial fuels consist of multiple compounds with different evaporation characteristics. Therefore, especially at low temperatures, the evaporation of a multi-component spray can lead to a spatial separation of light and heavy fractions of the fuel. Itani et al. [44] used a combination of *n*-pentane, *iso*-octane and *n*-undecane to match the evaporation characteristics of commercial gasoline to study the effect of preferential evaporation. To visualize the different volatility classes, *p*-difluorobenzene (for high volatility) and 1-methylnaphthalene (for low volatility) were added to the surrogate fuel (Figure 11, left). Since the fluorescence spectra after excitation with 266 nm of these two tracers are separated from each other, the ratio of two different spectral-windows (similar to two-color thermometry) can give information of the distribution of the two tracers (and therefore also for the different species of the surrogate fuel) during the evaporation (Figure 11, right). The photo physical information for both tracers used here is given in this thesis (see chapter 5.3 and 5.5). A similar method was used by Krämer et al. [61]. They used different tracer combinations (acetone/toluene, acetone/*p*-xylene and 3-pentanone/*p*-xylene) to represent different volatility classes. The fluorescence has then been measured after passing either a band pass filter (295 nm \pm 15 nm) or a WG360 for various degree crank angle (DCA) in an IC engine. The location of each tracer could be displayed for the meas-

ured DCA, showing the feasibility of simultaneous mapping of fuel distributions of two different fluorescent markers representing different volatility classes.

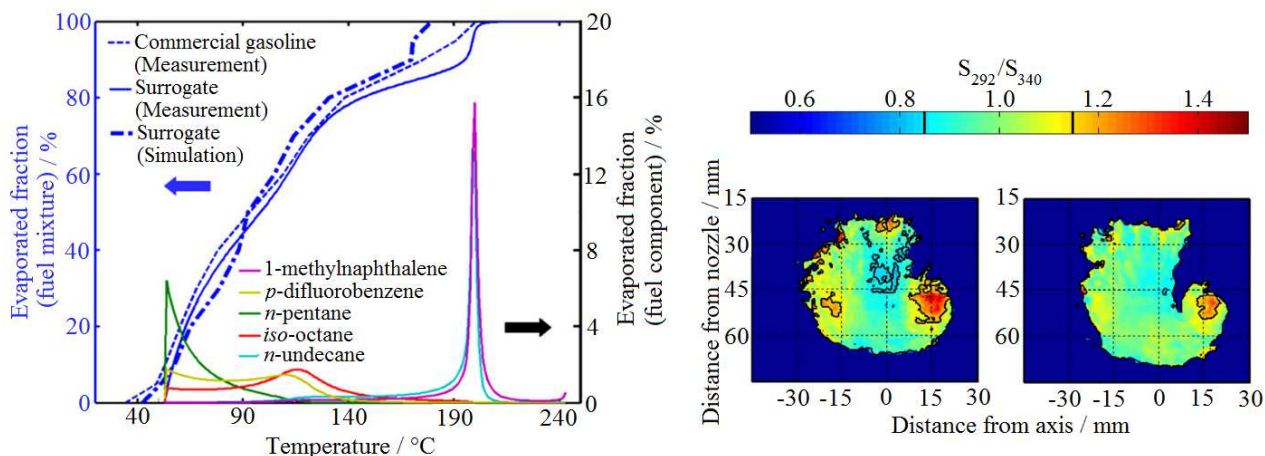


Figure 11: Evaporation characteristics for 1-methylnaphthalene, *p*-difluorobenzene, *n*-pentane, *iso*-octane, and *n*-undecane as well as their combined evaporation fraction compared to commercial fuel (left) [44]. Two-dimensional distribution ratio of high volatile species (red) and low volatile species (blue) for 550 K (left) and 600 K (right) [44].

3.3.4 Diagnostics based on the fluorescence lifetime

Apart from the previously described methods of measuring time-integrated fluorescence intensities for the determination of the desired quantities, there is also the possibility of exploiting the temporal variation of the fluorescence signal via time-resolved measurements. The lifetime of the excited state can be determined from the temporal decay of the fluorescence intensity. In order to be able to reliably determine this quantity, the excitation source must be pulsed and its pulse duration must be short with respect to the fluorescence lifetime. By temporal decay fitting including a convolution with the instrument function, fluorescence lifetimes close to the duration of the pulse can be measured [62, 63]. Since the fluorescence lifetime is proportional to the ϕ_{fl} (see chapter 4.3), it can therefore also lead to the desired parameters such as temperature or O_2 concentration. An advantage of lifetime- instead of intensity-based measurements is their independence on the absolute intensity that is influenced e.g. by variations in laser intensity and tracer concentration. In addition, a quantity proportional to ϕ_{fl} can be determined without knowing the absorption cross-section σ_{abs} . Despite these advantages, these measurements are rarely performed, most probably because more sophisticated equipment is necessary that can mostly be applied to point measurements.

A proof-of-concept of this method for temperature measurement has been done by Friesen et al. [33]. They used an optically accessible spark-plug sensor to measure the fluorescence lifetime after excitation with 266 nm in a small probe volume via fiber based illumination and detection and time-correlated single-photon counting (TCSPC). The measured fluorescence lifetimes were then transformed into corresponding temperatures using the temperature dependence of the fluorescence lifetimes measured before in a flow cell [22]. The results were in good agreement with the temperature calculated from the pressure trace.

4 Theoretical background – photo physics of organic molecules

All the following information is taken from [64, 65] unless otherwise indicated.

4.1 Absorption

4.1.1 Classification of electronic transitions

An electron reaches a higher state by absorbing the energy of a light quantum (photon), provided that the energy of the photon corresponds to the energy difference between the states involved. This process is identical for all atoms and molecules and differs only by the energy gap of the states that are characteristic for each atom or molecule. The wavelength-dependent molecular absorption cross-section $\sigma_{\text{abs}}(\lambda)$ indicates the probability of such a transition. It can be calculated by time-dependent perturbation theory, which is not dealt with in this work.

The electron transitions are subdivided into different classes, which are determined by the involved electron orbitals. In the case of the organic molecules of interest, these orbitals were composed of linear combinations of atomic s- and p-orbitals. Three main groups of orbitals can be distinguished:

- Bonding σ - and π -orbitals
- Antibonding σ^* - and π^* -orbitals
- Nonbonding orbitals

The highest occupied molecular orbital (HOMO) is a bonding σ -, π - or a neutral n-orbital. The lowest unoccupied molecular orbital (LUMO) is usually an antibonding σ^* - or π^* -orbital. The following transitions are possible:

- $\pi \rightarrow \pi^*$, e.g., with alkenes,
- $n \rightarrow \pi^*$, e.g., for substances with carbonyl groups (ketones, aldehydes)
- $n \rightarrow \sigma^*$, e.g., with amines, alcohols
- $\sigma \rightarrow \sigma^*$, e.g., for alkanes

In analogy to the classification in functional groups for a particular reaction behavior, organic substances can also be grouped in photophysical groups. The decisive factor is the so-called chromophore, which is responsible for light absorption. Table 2 provides an overview of some of these groups.

Table 2: Transition, peak wavelength and σ_{abs} for some typical chromophores [66].

Chromophore	Transition	$\lambda_{\text{max}} / \text{nm}$	$\sigma_{\text{abs}} / 10^{-20} \text{cm}^2$
C=O	$n \rightarrow \pi^*$	280	8
Benzene	$\pi \rightarrow \pi^*$	260	80
C=N	$n \rightarrow \pi^*$	240	50
C=C-C=C	$\pi \rightarrow \pi^*$	220	8×10^4
C=C	$\pi \rightarrow \pi^*$	180	4×10^4
C-C	$\sigma \rightarrow \sigma^*$	< 180	400
C-H	$\sigma \rightarrow \sigma^*$	< 180	400

4.1.2 Classification of electron states into different classes

Most organic molecules have a noble gas configuration. This means that all their binding orbitals are occupied. According to Fermi, each orbital is occupied with a spin \uparrow as well as with a spin \downarrow electron. This results in a total spin $S = 0$.

Apart from the spin, the degree of excitation is also important for the state description. In this case, one of the electrons is raised to a higher state, as a result of which the total spin can change, since the spins can be arranged parallel or antiparallel in two half-occupied orbitals. According to their degree of degeneracy (also called multiplicity) one distinguishes singlet (S) states with $S = 0$ and triplet (T) states with $S = 1$. The index is used to indicate the degree of degeneracy, where zero is the ground state. Figure 12 shows simple transitions.

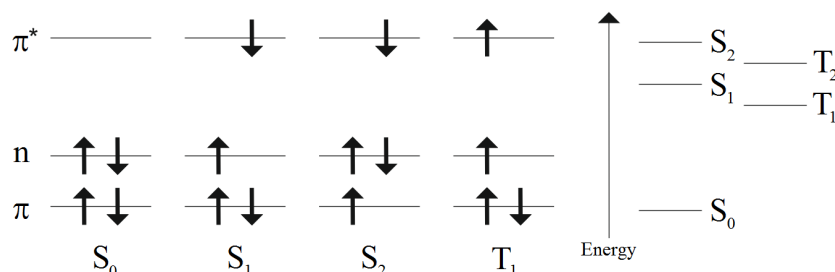


Figure 12: Electron configuration and their terminology according to the spin behavior of the corresponding carbonyl group (left) and the relative energy of their electronic states (right). S: singlet and T: triplet.

4.2 Deactivation of excited states in molecules

The process of absorption leaves an unoccupied orbital in an energetically more favorable state, which is why the excited state is not stable. The additional energy can lead to a chemical process such as decay of the molecule, a reaction or a physical process. Chemical processes are irrelevant for the present work and are therefore not further considered. The physical processes we are interested in can be divided into 3 groups:

- Radiation processes: emission of a photon
- Radiation-free processes: deactivation of the state without photon emission
- Quenching: energy transfer to another molecule

The first two groups can be visualized using a Jablonski diagram (Figure 13). Radiation processes are shown here as wavy lines, non-radiative processes as straight lines. First, the molecule is excited by absorption. Depending on the energy of the absorbed light quantum, the electron reaches a corresponding excited energy level of the 1S_1 state. Collisions with adjacent molecules give the molecule energy in form of heat or take it away, depending on the Boltzmann statistics (see 4.5.1), and the electron enters the corresponding energy level of the 1S_1 state. This process is called vibrational relaxation (VR). It is also possible for the electron to change the electronic state at any time. If the degree of degeneracy (multiplicity) is retained, this is referred to as internal conversion (IC) and the electron traverses to high energy levels of 1S_0 . If it changes, it is called intersystem crossing (ISC) and the electron enters the triplet state 3T_1 .

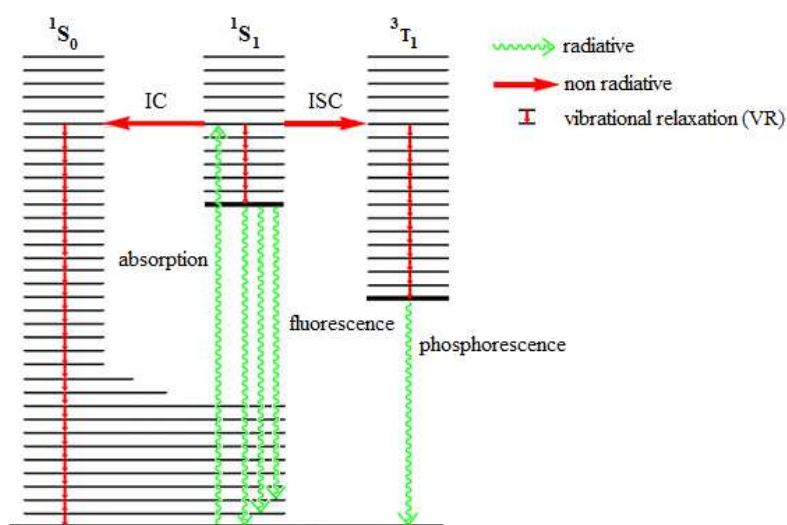


Figure 13: Jablonski diagram; photophysical activation and deactivation processes of a molecule. ISC: Intersystem crossing, IC: internal conversion, VR: vibrational relaxation.

For LIF, only the emission of light from the 1S_1 state known as fluorescence is usable. The fraction of electrons that is deactivated this way in relation to the number of absorption processes determine the ϕ_{fl} . The probability of any process to occur in the excited state mainly depends on the current energy level that the electron occupies.

4.2.1 Fermi's golden rule

Fermi's golden rule is a solution for the quantum-mechanical transition $m \rightarrow n$ of two states, analogous to the time-dependent Schrödinger equation for the absorption:

$$\frac{d}{dt} P_n = \frac{2\pi}{\hbar} \mathbf{M}_{nm}^2 \rho_n \quad (2)$$

P_n is the transition probability and $\mathbf{M}_{nm} = \langle \Psi_n | \hat{H}' | \Psi_m \rangle$ is the transition matrix element known from quantum mechanics. \hat{H}' is the part of the Hamilton operator responsible for the transition and $\langle \Psi_n |$ and $|\Psi_m \rangle$ the wave function of the final and initial state, respectively. ρ_n is the density of the states, also referred to as phase space, and includes the degree of degeneracy of the final state.: In case of absorption, $\rho = 1$, since this transition is a “state-to-state” process.

4.2.2 Radiative processes

The process of spontaneous emission of a photon is analogous to that of the absorption and accordingly follows the same selection rules, the transition matrix element and the transition probability. Since there is also a strong transition-frequency dependence of the phase space of the final state in the photoemission with $\rho_n \sim \nu^2$, radiative transitions between two oscillation levels of an electronic state are unlikely. One can think of various possible (quantified) "emission directions" to visualize this. Two types of radiation processes are distinguished by the different origin of their transitions:

Fluorescence

The transition which leaves the total spin unchanged (the so called spin-allowed transition) is called fluorescence. It usually takes 0.5–100 ns. This applies, for example, for allowed electronic $S_1 \rightarrow S_0$ dipole transitions. In the case of symmetrically and orbital-prohibited transitions, e.g., for ketones, the natural lifetime, would be on the order of microseconds. This would be the case if the S_1 state would not be depopulated much faster by intersystem crossing. As a result, the effective fluorescence lifetime is only a few nanoseconds (also see chapter 4.3.2).

Phosphorescence

The transition from triplet states to the ground state $T_1 \rightarrow S_0$ often has a much longer lifetime compared to those from singlet states. This is, on the one hand, due to the spin prohibition of the transition. On the other hand, the low probability for transition from $T_1 \rightarrow S_0$ via intersystem crossing into excited states of the ground state, leads to a lack in other potent deactivation pathways. This is due to the large energy gap from the triplet to the ground state. Phosphorescence usually lasts 1 μ s – 1 s and can therefore also be distinguished from the fluorescence. In addition, there is often a different emission spectrum, since the energy of the triplet state in general is lower than that of the singlet state.

4.2.3 Fluorescence spectra of aromatic molecules

The fluorescence spectrum of a laser-excited aromatic molecule is not as narrow as one may be accustomed to from an atomic fluorescence spectrum. The average half-width of a single electronic band is several tens of nanometers. There are various reasons for this. The first is the Boltzmann statistics, which describes the occupation of vibrational states (and the superposition of those) around the thermal energy level. Thus also slightly lower or higher energy levels are populated and add to the spectral range. This only has a small influence at low temperatures but increases in importance for higher temperatures and is also responsible for the redshift of the absorption and fluorescence spectra. The main reason for the broad spectra is the existence of numerous vibrational modes in larger molecules. The vibrational states, created by all superposition possibilities of the numerous and coupled vibrational modes, are also characteristic for each molecule. These states nearly form an energy band of possible target energy levels for the fluorescence in the ground state. The spontaneous emission could, theoretically, choose any of these energy levels,

varying the emitted energy and therefore the wavelength in the process. However, the probability of each transition is defined by the subsequent Franck-Condon factor for the transition. The spectra are then formed by the possible transitions from the populated energy levels in the excited state to the band of energy levels in the ground state, convoluted with the Franck-Condon factors.

4.2.4 Non-radiative processes

Energy-gap law

The probability of a radiative transition between two excited electronic states (internal conversion or intersystem crossing) is strongly dependent on the energy difference between the starting and the target state. This is due to the core wave function, whose spatial overlapping on the same level of energy becomes worse when the origin energy levels are far apart. For benzene derivatives, the singlet-triplet energy potential is significantly greater than 1.3 eV. This results in a slow transition of excited electrons from $S_1 \rightarrow T_1$. Ketones e.g., have an energy gap of approx. 220 meV, which is why the $S_1 \rightarrow T_1$ transition for ketones occurs much faster. A rapid transition from the S_1 state to T_1 means a reduction in the fluorescence signal since the S_1 state depletes faster than the natural fluorescence lifetime is (see chapter 4.3.2).

Singlet-triplet broadening

For electrons, it is always more energetically convenient when its spin is parallel with others. If all orbitals are filled in the ground state, excited triplet states will always have a lower energy level than excited singlet states, although their quantum numbers are identical. A clear explanation for this is provided by Coulomb repulsion, which will not be explained here in detail. The core point is that the singlet and the triplet state in aromatics and ketones have different orbital transitions. The transition in aromatics is a $\pi \rightarrow \pi^*$ transition whose orbital overlap is significantly greater than that for ketones, which is a $n \rightarrow \pi^*$ transition. A larger overlap is equivalent to a smaller distance of the electrons and thus a stronger Coulomb repulsion, which increases the splitting of the singlet-triplet levels.

Intersystem crossing (ISC)

Intersystem crossing is the non-radiative transition between two electronic levels, which changes the total spin. The energy of the molecule is not changed, only the energy gap between the origin energy level of the excited and the ground state is different, since a potential function with a lower minimum is reached. With the energy-gap law the influence on the transitional probabilities has already been discussed. However, the electronic wave function also has an effect on the probability of transition. Intersystem crossing is in principle spin prohibited. It is only possible through spin-orbit coupling. The “El-Sayed's rules” now emerge from the symmetry considerations, which are only enumerated here, but are not further explained or derived:

- ISC for singlet triplet $n \rightarrow \pi^*$: transition is “forbidden”
- ISC for singlet triplet $\pi \rightarrow \pi^*$: transition is “forbidden”

- ISC for singlet- $n \rightarrow \pi^*$ – triplet $\pi \rightarrow \pi^*$: transition is “allowed”
- ISC for singlet- $\pi \rightarrow \pi^*$ – triplet $n \rightarrow \pi^*$: transition is “allowed”

The quotes are necessary because the El-Sayed forbidden transitions also have a non-zero transition probability. This is due to vibrations of the nuclei, which make this transition possible. Higher oscillation excitation thus also means a higher transition rate through intersystem crossing. However, the probability of a “forbidden” transition is lower (by a few orders of magnitude) than that of an “allowed” one. Although intersystem crossing for benzene derivatives, such as the aromatic compounds discussed in this work, is “forbidden”, its transition rates are nevertheless about one order of magnitude greater than the rate for spontaneous emission.

Internal conversion (IC)

Internal conversion is the radiation-free transition between two electronic states without changing the total spin. This transition is spin-allowed, which is why it is limited only by the energy gap law. This is also the reason why only the first excited state exhibits spontaneous emission. Higher singlet states are very quickly depopulated by internal conversion due to their much smaller energies to the neighboring lower state, e.g., $S_2 \rightarrow S_1$ for example. In addition, the results of the work of Hsieh et al. [46] indicate that, while the excess energy of the excited state S_1 is low, the main non-radiative deactivation pathway is ISC while IC just plays a minor role. If the excess energy increases, the importance of IC increases as well until the significance of both effects is reversed.

Vibrational relaxation (VR)

Thermal energy according to a temperature above 0 K is stored in molecules according to the Boltzmann statistics, depending on the distribution of vibrational energy modes. Vice versa, if a molecule enters an excited state, e.g., after absorption of a photon, the distribution of the energy in the vibrational modes (excess energy, Figure 13) can be transcribed to the momentary temperature of the said molecule. If two molecules of different vibrational energy collide, a fraction of the energy difference is transferred to the lower-energy collision partner. This process of temperature adaptation is called vibrational relaxation. Subsequent collisions then slowly reduce the energy difference between the excess energy from absorption and the energy prescribed by the Boltzmann statistics of the bath gas. This results in an increase or a decrease of the energy in the molecule, depending on its initial conditions relative to those of the collision partners. As the number density of the collision partners increases, the collision frequency increases as well, as a result of which the relaxation time to the average thermal energy level (ATEL), defined by the Boltzmann distribution of the bath gas becomes pressure-dependent. Since the energy of the excited state also has an influence on the non-radiative deactivation pathways and the fluorescence time scales, vibrational relaxation and therefore pressure has an influence on the ϕ_{fl} [67].

4.3 Quantum yield and fluorescence lifetimes

4.3.1 Fluorescence quantum yield

As explained in chapter 4.2, there are several processes that can deactivate an excited state. Therefore, only a fraction of the absorbed light is emitted as photons again. This ratio is referred to as the fluorescence quantum yield (ϕ_{fl}):

$$\phi_{fl} = \frac{\text{Number of fluorescing molecules per time and volume}}{\text{Number of absorbed photons per time and volume}}$$

In the case that all the excited molecules would spontaneously emit, ϕ_{fl} would be one. The non-radiative deactivation processes therefore reduce the fluorescence quantum yield. While the transition rates of absorption and fluorescence can also be referred to as Einstein coefficients, the other deactivation processes symbolize losses:

- Absorption; transition rate: $k_{abs}[M][h\nu]$
- Fluorescence; transition rate: $k_{fl}[M^*]$
- All other (non radiative) deactivation processes; transition rate: $k_{NR}[M^*]$

Let $[M]$ be the concentration of ground state molecules and $[M^*]$ that of the molecules in the excited state. For each substance it must be investigated whether induced emission and saturation effects can be neglected during absorption. If so, one can assume that the absorption is proportional to the photon flux and the concentration of the molecules in the ground state. On the other hand, the fluorescence process rate increase linearly with the concentration of excited molecules. The ϕ_{fl} is then given by:

$$\phi_{fl} = \frac{k_{fl}[M^*]}{k_{abs}[M][h\nu]} \quad (3)$$

Since the concentration of the excited molecules cannot be easily determined, these are replaced by the transition rates, which represent the temporal change of their concentration:

$$-\frac{d}{dt}[M^*] = k_{fl}[M^*] + k_{NR}[M^*] - k_{abs}[M][h\nu] \quad (4)$$

With the assumption of quasi-equilibrium in the excited state, the left hand side of this equation tends to zero, which gives:

$$[M^*] = \frac{k_{abs}[M][h\nu]}{k_{fl} + k_{NR}} \quad (5)$$

Together with equation (3), the fluorescence quantum yield is derived as follows:

$$\phi_{fl} = \frac{k_{fl}}{k_{fl} + k_{NR}} \quad (6)$$

4.3.2 Natural and effective lifetime

First, it is assumed that the fluorescence is the only possible deactivation process. For a certain concentration of excited molecules, the following holds:



Since spontaneous emission, like radioactive decay, is a random process, it can also be expressed by a differential equation of the first order:

$$-\frac{d}{dt}[M^*] = k_{fl}[M^*] \quad (8)$$

$k_{fl}[M^*]$ is again the transition rate for the fluorescence. The solution for (8) provides:

$$[M^*] = [M^*]_0 e^{-k_{fl} t} \quad (9)$$

The initial value of the concentration immediately after excitation is denoted as $[M^*]_0$. The characteristic value here is not the half-life time, but the time until the concentration has dropped to $\frac{1}{e}$ of its initial value. This time is designated as the natural lifetime of the excited state, τ_{fl} :

$$\tau_{fl} = k_{fl}^{-1} \quad (10)$$

As can be seen from chapter 4.2, the selection rules for fluorescence correspond to those for absorption. Accordingly, the natural lifetime is long when the absorption coefficient is small. Table 3 provides some typical, non-specific values.

Table 3: Typical values for σ_{abs} and natural lifetime τ_{fl}

	Dipole allowed	Dipole prohibited, vibrationally allowed	Spin prohibited, Spin-orbit-allowed
$\sigma_{abs} / 10^{-20} \text{cm}^2$	2×10^3	5	5×10^{-3}
$\tau_{fl} / \mu\text{s}$	1×10^{-3}	5	5×10^3

This simplified model does not survive a reality check. The non-radiative processes intersystem crossing (ISC) and internal conversion (IC) affect the natural lifetime through their transition rates, which is why they need to be incorporated into the model:

$$-\frac{d}{dt}[M^*] = k_{fl}[M^*] + k_{ISC}[M^*] + k_{IC}[M^*] \quad (11)$$

Analogous to equation (9) the root of Eq. (11) is:

$$[M^*] = [M^*]_0 e^{-k_{tot} t}, \quad k_{tot} = k_{fl} + k_{ISC} + k_{IC} \quad (12)$$

In k_{tot} , all deactivating rates are summarized:

$$k_{tot} = \sum k_i = k_{fl} + k_{NR} = k_{fl} + k_{IC} + k_{ISC} + \sum k_{q,j} n_{q,j} = \frac{1}{\tau_{eff}} \quad (13)$$

k_{tot} is what is obtained by measuring the de-excitation process in a time-resolved manner over the fluorescence signal decay. The effective lifetime of the fluorescence is thus:

$$\tau_{eff} = \frac{1}{k_{tot}} \quad (14)$$

The ratio between natural and effective lifetime strongly depends on the environmental conditions. The effective lifetime can be similar to the natural lifetime for ideal conditions (e.g., low temperature) or be smaller by a few orders of magnitude for many conditions. For the substances of inter-

est in this dissertation, this is mainly due to the effective ISC process and the excess-energy dependent importance of IC for higher temperatures. Substituting equations (10) and (14) into equation (6), it is clear that the fluorescence quantum yield is proportional to the effective lifetime:

$$\phi_{\text{fl}} = \frac{k_{\text{fl}}}{k_{\text{tot}}} = \frac{\tau_{\text{eff}}}{\tau_{\text{fl}}} = k_{\text{fl}} \tau_{\text{eff}} \quad (15)$$

Since the measured signal strength S_{fl} is proportional to the number of fluorescence quanta and the absorption can be represented by a product of photon flux density, molecular absorption cross-section and molecular concentration, the signal strength thus results in [68]:

$$S_{\text{fl}} = \frac{E}{h\nu} \eta_{\text{opt}} dV_c n \sigma_{\text{abs}} \phi_{\text{fl}}, \quad (1)$$

With the photon flux density $\frac{E}{h\nu}$, the system-dependent factor for losses in the detection system η_{opt} , the detection volume dV_c , the number density of the fluorescent molecule n , and the molecular σ_{abs} and the fluorescence quantum yield. Thus, the ϕ_{fl} is obtained via the signal strength and thus, together with the measured effective fluorescence lifetime τ_{eff} , the natural fluorescence lifetime τ_{fl} can be determined. Conversely, equation (15) can also be used to deduce the relative quantum yield from the measured lifetime without having to take parameters such as the σ_{abs} or the number density into account. This is the approach that is used in the following work.

4.4 Quenching

If only a single molecule of the tracer species of interest would be present in the sample volume, all possible deactivation processes would have been already discussed above. Under realistic conditions, however, both gas molecules of different species are present interacting via collisions with the excited molecules. The effect of collision-induced vibrational relaxation that corresponds to a temperature equilibration, has already been discussed in chapter 4.2.4. However, there are other intermolecular interactions which can lead to deactivation.

4.4.1 Stern-Volmer behavior for collisional quenching

The previous model (equation 15) is now supplemented by a quenching term, which means a collision-induced depopulation of the excited state. For the special role of molecular oxygen as the most prominent quencher in case of aromatic compounds, see section 4.4.3. The quenching process depends on the number density of both the excited molecules and the quencher. Following the considerations in chapter 4.3.1, one obtains:

$$\phi_{\text{fl}} = \frac{k_{\text{fl}}}{k_{\text{tot}}} = \frac{k_{\text{fl}}}{k_{\text{fl}} + k_{\text{ISC}} + k_{\text{IC}} + k_{\text{q}} n_{\text{q}}} = \frac{\tau_{\text{eff}}}{\tau_{\text{fl}}} = \text{const.} \tau_{\text{eff}}, \quad (16)$$

where n_{q} is the quencher number density and k_{q} is the quenching rate-coefficient. The proportionality between signal strength and fluorescence quantum yield can then be written [2]:

$$\frac{S_{\text{fl}}^0}{S_{\text{fl}}} = \frac{k_{\text{fl}}}{k_{\text{tot}}} \frac{k_{\text{tot}} + k_{\text{q}} n_{\text{q}}}{k_{\text{fl}}} = 1 + \frac{k_{\text{q}}}{k_{\text{tot}}} n_{\text{q}} = 1 + k_{\text{SV}} n_{\text{q}} \quad (17)$$

S_{fl}^0 is the signal strength without the presence of the quencher. The ratio $\frac{S_{fl}^0}{S_{fl}}$ is a measure of the strength of the quenching effect. In order for equation (17) to be applicable, k_{tot} of S_{fl}^0 and S_{fl} need to be identical, i.e., the measurement of the two separate signal intensities must take place under otherwise identical environmental conditions (temperature, pressure, ...). The visualization of equation (17) is called a Stern-Volmer plot (Figure 14) and is a straight line with the slope $\frac{k_q}{k_{tot}}$ and the ordinate 1.

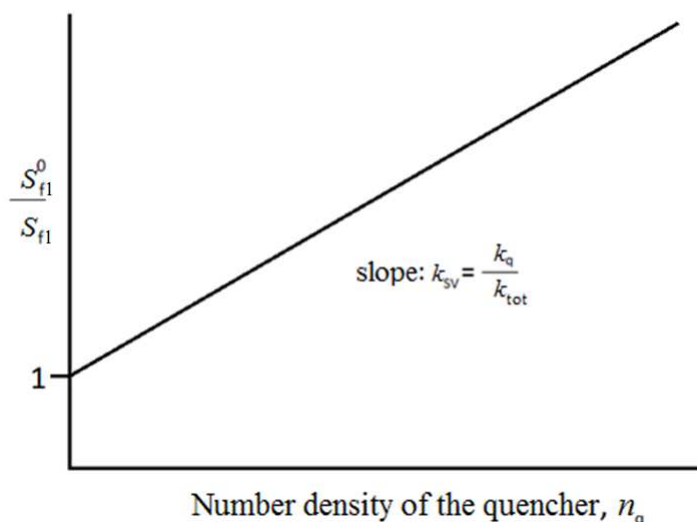


Figure 14: Schematics of a Stern-Volmer behavior, S_{fl}^0 : signal strength without quenching; S_{fl} : signal strength with quencher; k_q : quenching rate-coefficient in s^{-1} ; k_{tot} : sum of all deactivation rate-constants in s^{-1} .

With the slope and equation (9) one obtains the so called Stern-Volmer coefficient:

$$k_{SV} = \frac{k_q}{k_{tot}} = k_q \tau_{fl} \quad (18)$$

If one knows the signal strength of the unquenched fluorescence, and therefore the effective ϕ_{fl} , one can determine the quencher rate coefficient k_q from the slope. Due to the proportionality of the ϕ_{fl} and the fluorescence lifetime, the latter can also be used. The Stern-Volmer coefficient itself serves as a measure of the effectiveness of the quenching for a specific collision pair. Another way to determine k_q is to define a probability for collisional quenching. Thus, k_q can be determined as the product of the collision frequency Z_{coll} that we find from kinetic gas theory, and the quenching probability for each collision $\langle p \rangle$:

$$k_q = Z_{coll} \langle p \rangle \quad (19)$$

$\langle p \rangle$ is also called the efficiency of the quenching process.

4.4.2 Electronic energy transfer

An important process leading to quenching is related to electronic energy transfer. In general, during the collision, the excitation energy of the molecule is transferred to the collision partner [69]:



We denote M^* as donor and Q as acceptor. In the following, two basic mechanisms of quenching are distinguished that both lead to electronic excitation of the quencher.

Short range energy transfer through electron exchange

This effect, first discovered by Dexter in 1953 [70], requires an orbital overlap of the two species involved. It thus assumes an intermolecular distance of 0.5–1 nm. Moreover, the spectral overlap of the emission spectrum of the donor and the absorption spectrum of the acceptor is crucial for the transition probability. The intra-molecular transitional probabilities between the orbitals are irrelevant. Transfer processes for the electron exchange are [69]:



Long-range resonant energy transfer

This process that was first described by Förster (1948) [71], is generally abbreviated as FRET (“Förster resonance energy transfer”). In this case, the donor influences the electronic structure of the acceptor by means of the dipole–dipole interaction, as a result of which the quencher Q makes a transition into a higher vibrational state. This process is active for intermolecular distances of up to 10 nm, which corresponds to several molecular radii. We can calculate the dipole interaction by the operator

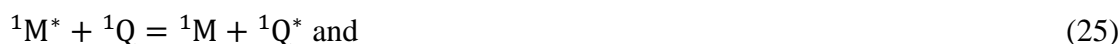
$$\hat{H}' = \frac{\mathbf{p}_M \mathbf{p}_Q}{r^3} \quad (23)$$

\mathbf{p} is the dipole moment of the transition and r is the inter-molecular distance. The strength of the interaction thus obtains a $\left(\frac{1}{r}\right)^6$ dependence since the probability for a transition depends on the square of the matrix element. Finally, the probability is [71]:

$$\frac{d}{dt} P_n = \frac{1}{\tau_{fl}} \left(\frac{r_0}{r}\right)^6 \quad (24)$$

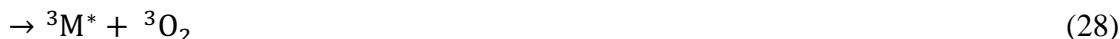
with the natural fluorescence lifetime τ_{fl} of M^* . The strength of this interaction is determined by the Förster distance r_0 . It determines the distance in which the energy transfer efficiency is 50% and is derived from the spectral overlap of the emission spectrum of the donor with the absorption spectrum of the acceptor and the transition probability of the electrons.

The occurring processes are determined through the position of the electrons by the spin selection rules [69]:



4.4.3 Fluorescence quenching by molecular oxygen

Since O_2 has a triplet ground state it is an effective quencher for many organic molecules. Therefore, it will be considered here in more detail. The energy transfer follows the pathways [69]:



The states of local excitation (e.g., ${}^3({}^1M^*, {}^3O_2)$, ${}^3({}^3M^*, {}^3O_2)$ etc.) are mixed with the charge-transfer state (${}^3M^+, {}^2O_2^-$) to a so-called exciplex. Since the two states have different spin multiplicities, the normally spin-forbidden intersystem crossing (ISC) is enhanced. However, this process can only take place if the energy required for the excitation of oxygen to the singlet state (0.98 eV, 91 kJ/mol) is exceeded by the singlet–triplet splitting of the molecule. Ketones for example have a much smaller singlet–triplet splitting (~40 kJ/mol), which is why quenching by molecular oxygen can be neglected for these tracers. For the aromatics discussed in this work, O_2 has a great influence on the ϕ_{fl} and thus also on the fluorescence lifetime, which is why – besides pressure and temperature – the oxygen concentration in the performed experiments is an additional quantity of interest.

4.4.4 Self-quenching

With increasing tracer concentration, tracer–tracer collisions gain importance, leading to the possibility of self-quenching. For small molecules like nitric oxide (NO) and nitrogen dioxide (NO_2), this behavior is well-known and the self-quenching rate constants have been determined by measuring the concentration dependence of the fluorescence lifetime [72, 73]. In these studies, the fluorescence decay rate showed a linear dependence on the tracer's partial pressure, which was attributed to collisions of the excited tracer A^* with ground-state molecules A. The effect of self-quenching is then fully represented by the self-quenching rate coefficient \tilde{k}_q^{tr} and the tracer number density n_{tr} .

For some larger aromatic molecules like anthracene [74] and pyrene [75], self-quenching has been investigated in detail. The self-quenching rates of pyrene and anthracene exhibit a negative temperature dependence and the activation energy determined from the observed temperature dependence is in the order of the binding energy of the relevant excimers $(AA)^*$. Through this observation and further supporting kinetic models, Davis et al. [75] suggest that the formation of an excimer is involved in the self-quenching process. For toluene, the effect will be discussed in greater detail in chapter 5.2.

4.5 Fluorescence model development

The availability of experimental σ_{abs} and ϕ_{fl} (or effective fluorescence lifetimes) under a wide range of environmental conditions makes it possible to develop semi-empirical or phenomenological models with which the corresponding signal can be predicted for the given conditions such as pressure, temperature, and O_2 concentration.

In 2005, Koban et al. presented a semi-empirical model for toluene which was able to predict the relative fluorescence quantum yield of toluene for various temperatures and O_2 partial pressures [20]. This model was fitted to the data that he accumulated and works well for temperatures below 750 K and at 1 bar total pressure:

$$\phi_{\text{fl}}(T, n_{\text{O}_2}) = \left[\frac{A_1(\lambda_{\text{exc}}, T)}{1+k_{\text{SV},1} n_{\text{O}_2}} + \frac{A_2(\lambda_{\text{exc}}, T)}{1+k_{\text{SV},2} n_{\text{O}_2}} \right] \quad (29)$$

However, since this model neglects the photo physical processes that lead to fluorescence, it fails to predict the ϕ_{fl} outside the parameter range of the measured data (especially at high oxygen concentrations and temperatures that are present during the compression stroke in an IC engine where the model produces a singularity). For a phenomenological model that does not have this flaw, clear understanding of the deactivation processes and their rate constants is essential. In the following chapter, the necessary theoretical background as well as a realization for toluene is presented.

4.5.1 Average thermal energy level (ATEL)

For a specific temperature, the ensemble of molecules is distributed to various vibrational and rotational energy levels according to the Boltzmann distribution. In larger molecules such as aromatics these are (due to superposition) so dense that, to a good approximation, the states can be considered to form a quasi-continuous band. The higher the temperature, the higher energy levels are populated through the Boltzmann distribution. For simplification, often an average thermal energy level (ATEL) is considered rather than a detailed description of a whole distribution. This applies to any bound electronic state. The temperature dependence of the distribution is based on all the vibrational energy levels of the respective electronic states [2]. The ATEL can be calculated (in cm^{-1}) as:

$$E_{\text{therm},n} = \sum_{i=1}^N \frac{E_{\text{vib},i}}{e^{\frac{1,44 E_{\text{vib},i}}{KT}} - 1} \quad (30)$$

The values thus determined indicate the energetic distance of the ATEL of an electronic state from its vibrational zero-point energy level as a function of the temperature.

4.5.2 Energy-dependent transition-rate constants

In section 4.2, the most important deactivation processes of excited molecules have already been discussed. Since the non-radiative transition rates as well as the fluorescence transition rate are energy-dependent, it is also important to consider the probability of a change in the energy level

due to vibrational relaxation for a closer look at the formation of the fluorescence. The more collisions the molecule experiences between excitation and deactivation, the closer it moves from the excitation level to an average thermal level E_{therm} of the S_1 state. The energy ΔE_{coll} is transmitted as collision energy by each of these collisions, which depends on the current energy level of the fluorescing molecule, the thermal energy level of the bath gas, and the bath-gas species. During this time, there is also the possibility of collisional quenching by, e.g., O_2 , which is not energy-dependent. Figure 15 illustrates these cascade processes schematically.

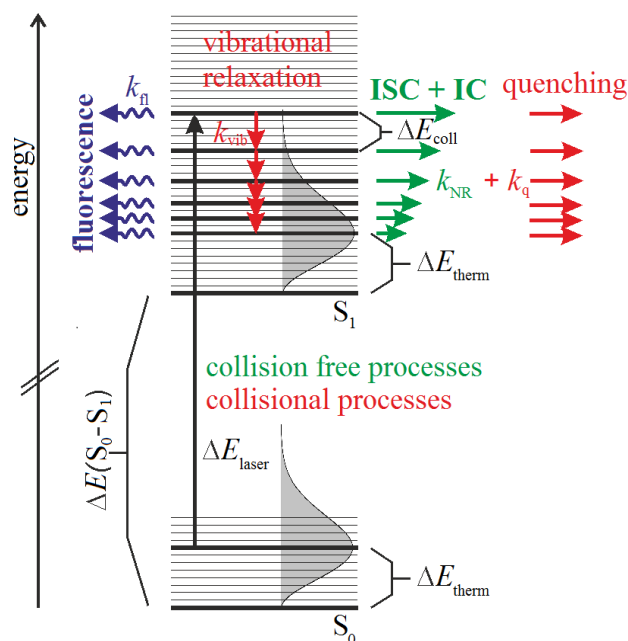


Figure 15: Jablonski diagram (based on [76]) that illustrates the most important energy-transfer processes and rate constants within the first excited state of an organic molecule after optical excitation.

4.5.3 Photo-induced cooling

A molecule in the ground state already has a certain amount of thermal energy. An excitation of the molecule with a photon with energy greater than the S_0 - S_1 bandgap not only gives an electron enough energy to reach the S_1 state but also to enter a state above the ATEL due to excess energy. Since the temperature corresponding to the energy of the newly excited molecule is higher than its environment, this ultimately leads to energy transfer to the bath gas due to collisions with the excited molecule. With each collision ΔE_{coll} is transferred to the bath gas.

On the other hand, it is also possible to populate the S_1 state between the S_1 vibrational zero-point energy and the ATEL as long as the sum of the thermal energy in the S_0 state and the photon energy is higher than the S_0 - S_1 bandgap. In this case, collisions with bath-gas species provide energy to the excited molecule to reach the ATEL and thus lead to cooling of the environment. An example for this is toluene at room temperature after excitation at 266 nm. However, since the thermal level of the S_1 state increases faster than that of the S_0 state (due to vibrational modes being denser), there is theoretically a temperature at which energy is absorbed by collisions for each molecule that releases energy due to collision at room temperature. A detailed explanation on this theoretical concept as well as experimental proof is given in chapter 5.1.

4.5.4 Step-ladder model

With this knowledge on the deactivation processes of excited molecules and the thermal energy distribution it is possible to understand the phenomenological model developed by Thurber [68] and extended by Koch [8] for the calculation of the fluorescence quantum yields of ketones. For each possible energy level, which the system can attain in the S_1 state, the probability of reaching this state is multiplied with the probability that it emits fluorescence from this energy level, and this is summed up for all states. The relative fluorescence quantum yield is then obtained:

$$\phi_{fl} = \frac{k_{fl,1}}{k_{fl,1} + k_{vib} + k_q[O_2] + k_{NR,1}} + \sum_{i=2}^{N-1} \left[\frac{k_{fl,i}}{k_{fl,i} + k_{vib} + k_q[O_2] + k_{NR,i}} \prod_{j=1}^{i-1} \left(\frac{k_{vib}}{k_{fl,j} + k_{vib} + k_q[O_2] + k_{NR,j}} \right) \right] + \frac{k_{fl,N}}{k_{fl,N} + k_{vib} + k_q[O_2] + k_{NR,N}} \prod_{j=1}^{N-1} \left(\frac{k_{vib}}{k_{fl,j} + k_{vib} + k_q[O_2] + k_{NR,j}} \right) \quad (31)$$

$k_{fl,i}$ is the energy-dependent fluorescence rate constant, $k_{NR,i}$ is the energy-dependent rate constant for non-radiative transitions, k_{vib} is the rate constant for vibrational relaxation (i.e., the number of collisions with a bath-gas molecule per second multiplied by a bath gas specific factor which indicates how much energy is transmitted per collision), and $k_q[O_2]$ the quenching rate constant for O_2 (the number of collisions with O_2 per second multiplied by a factor specific to O_2 , the efficiency of the quenching process in equation 18). Some of these constants were determined during this work and are shown in chapter 5.1.

Implementation of a model for toluene

If all transition rates, the thermal levels of the S_0 and S_1 states, the zero-point energy gap between the S_0 and S_1 state, as well as the necessary transition rates for collision for all substances are known, the fluorescence quantum yield can be simulated according to the model approach in equation (31). Rossow developed such a model in his dissertation [10], where he found good agreement between simulation and measured spectral intensities. Figure 16 shows his data (symbols) for toluene. The code used for the simulation was not available; however, the relevant equations were adapted in an in-house code [77]. The solid lines shown in Figure 16 show the behavior calculated according to equation (31). As comparison, the model of Koban is shown as dashed lines. Although the values are in good agreement for low and high temperatures, there is a slight overestimation of the model values around 450 K that does not occur in the model of Rossow. Despite this satisfactory agreement, there is still need for improvement in model development since total pressure and the excitation wavelength cannot be varied yet. The source code can be found in my diploma thesis [78].

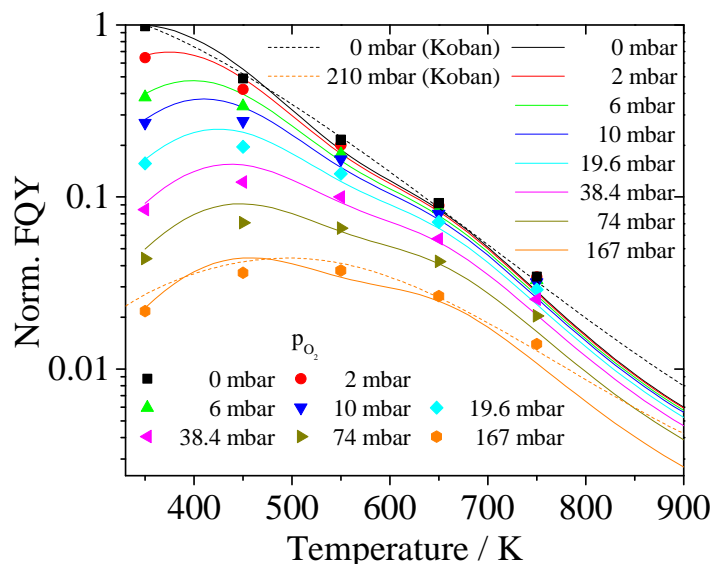


Figure 16: Comparison of the measured results of Rossow [10] (symbols) with the semi-empirical model of Koban [11] (dotted lines) and the phenomenological step-ladder model (solid lines) for the ϕ_{fl} of toluene after 266 nm excitation.

Since the results of the semi-empirical model by Koban et al. [11] are quite similar to the much more sophisticated (and literature data demanding) step-ladder model, semi-empirical models were chosen to estimate the fluorescence signal for the other aromatic compounds that were investigated during this work. The results for these species can be found in the publication chapters 5.3 and 5.4.

5 Published and unpublished results

The following chapter will present the core of this Dissertation, the research and results of my work at the University of Duisburg-Essen, which resulted in four publications in refereed journals (which the first four sub-chapters are based on) as well as some unpublished data at the end of the chapter.

The first publication gives insight into the pressure-dependence of laser-induced fluorescence of five aromatic species (toluene, 1,2,4-trimethylbenzene, anisole, naphthalene, and 1-methylnaphthalene), i.e., how the excess energy after electronic excitation is equilibrated into the corresponding Boltzmann distribution of the excited state due to collisions with the bath gas. Within this publication, photo-induced cooling and heating is explained and experimentally proven. Additionally, knowing the near collision-free fluorescence lifetimes, non-radiative transition-rate constants for these molecules were determined. The motivation for this publication is on the one hand to improve the understanding of the importance of vibrational relaxation and excess energy for the ϕ_{fl} , especially for the dependence of total pressure and on the other hand to give some transition rate coefficients for tracer species that do not have a photo physical model yet. The experimental data for this paper and its interpretation was gathered solely by myself.

The second publication is more focused on the fundamental understanding of the fluorescence process, especially the effect of self-quenching (process of deactivation through collisions with the same species). The effect was studied for varying tracer concentration, temperature and laser-induced fluence, as well as the fluorescence intensity and fluorescence lifetime. Critical values for the appearance of this effect are given, as well as experimental data, which shows that the collision of two excited molecules is the dominant process for self-quenching. The main goal of this paper is to illustrate the adverse effect of high tracer concentrations (often used to produce sufficiently strong signal) on the ϕ_{fl} . This work is resulting from collaboration with Dr. Daniel Fuhrmann, who performed the engine-related measurements, Dr. Torsten Endres, who was responsible for the low energy fluorescence lifetime data, and myself.

The third and fourth publications provide complete photo-physical characterizations of the aromatics 1,4-difluorobenzene (third paper), and 1,2-xylene and 1,2,4-trimethylbenzene (forth paper). In these studies, the absorption cross-section (σ_{abs}), fluorescence spectra and the fluorescence lifetime (and therefore the relative fluorescence quantum yield, ϕ_{fl}) were determined for combustion-relevant temperatures, total pressures and O₂ partial pressures. With these data, new semi-empirical models were developed that can even allow to extrapolate the photo physical properties of the respective species beyond the parameter range of the source data (within reasonable boundaries) and show global errors smaller than 12% within the whole set of experimental data. With these new additions to the tracer portfolio, some existing measurement techniques could be improved while some additional techniques have been enabled due to these published data and models (e.g., thermometry via absorption in case of 1,4-difluorobenzene). Data gathering and post pro-

cessing for these publications was done by myself. The same applies to the model development for 1,4-difluorobenzene, while Dr. Torsten Endres helped with the optimization of the model for 1,2-xylene and 1,2,4-trimethylbenzene.

The last section of this chapter presents some unpublished work on the ACS of anisole as well as the fluorescence spectra and fluorescence lifetimes of 1-methylnaphthalene. This completes the anisole data set of Faust et al. [41] and gives first insights into the usage of 1-methylnaphthalene as a suitable tracer for low-volatility applications.

5.1 Low-pressure effective fluorescence lifetimes and photophysical rate constants of one- and two-ring aromatics

The following chapter is based on the journal paper "Low-pressure effective fluorescence lifetime and photophysical rate constants of one- and two-ring aromatics", published in Applied Physics B, 121 (4) 2015, 549–558 by Thorsten Benzler, Stefan Faust, Thomas Dreier, and Christof Schulz.

Abstract

One- and two-ring aromatics such as toluene and naphthalene are frequently used molecular tracer species in laser-induced fluorescence (LIF) imaging diagnostics. Quantifying LIF signal intensities requires knowledge of the photo-physical processes that determine the fluorescence quantum yield. Collision-induced and intramolecular energy-transfer processes in the excited electronic state closely interact under practical conditions. They can be separated through experiments at variable low pressures. Effective fluorescence lifetimes of gaseous toluene, 1,2,4-trimethylbenzene, anisole, naphthalene, and 1-methylnaphthalene diluted in CO₂ were measured after picosecond laser excitation at 266 nm and time-resolved detection of fluorescence intensities. Measurements in an optically accessible externally heated cell between 296 and 475 K and 0.010 to 1 bar showed that effective fluorescence lifetimes generally decrease with temperature while the influence of the bath-gas pressure depends on the respective target species and temperature. The results provide non-radiative and fluorescence rate constants and experimentally validate the effect of photo-induced cooling.

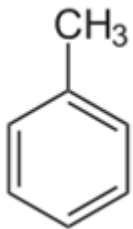
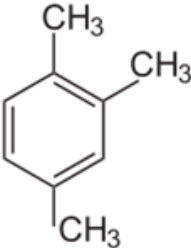
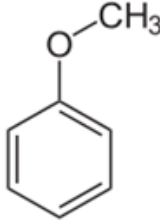
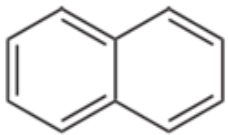
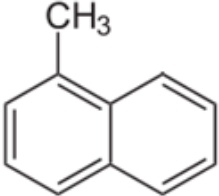
5.1.1 Introduction

Laser-induced fluorescence (LIF) imaging is commonly used, e.g., for the visualization of gas phase mixing processes and temperature measurements [4]. For this purpose, organic molecules, such as ketones, mono-aromatics (e.g., toluene), and di-aromatics (e.g., naphthalene) are frequently used as fluorescence tracers. For the observation of air/fuel mixing processes in combustion, they are added at low concentration (1–10%) to a non-fluorescing surrogate fuel. In any of these applications the measured fluorescence signal strongly depends on the environmental conditions, i.e., temperature, pressure, and bath-gas composition that influence the fluorescence quantum yield (ϕ_{fl}) for the particular excitation/emission process [20, 51, 58] and the absorption cross-section at the excitation wavelength [16]. While the absorption cross-section mostly depends on temperature, ϕ_{fl} also depends on pressure and bath-gas composition. Phenomenological step-ladder models have been set up for some ketones [8, 68] and aromatics [10] describing energy relaxation and emission processes within the energy level manifold in the excited state after laser excitation, and enable quantitative predictions of ϕ_{fl} within the investigated range of temperature, pressure, and bath-gas composition [9, 10, 68]. Temperature generally leads to reduced fluorescence quantum yields; the magnitude of this effect strongly depends on the tracer species. Pressure effects are less uniform and depend on the species, the temperature, and the bath gas. Increasing pressure can lead to either increasing or decreasing quantum yields. This behavior is not repro-

duced by the currently used models [9-11].

Lately, the concept of photo-induced cooling and heating, which distinguishes between laser excitation above the average thermal energy in an excited state (photo-induced heating) and below that level (photo-induced cooling), was introduced as an explanation for the species-specific dependence of the ϕ_{fl} on pressure [45, 79]. As other collision-induced energy-transfer phenomena these processes can best be studied by measuring effective fluorescence lifetimes in variable low-pressure environments where collision frequencies are reduced [65].

Table 4: Thermodynamic and electronic properties of the investigated aromatic compounds.

Species	Structure	Vapor pressure at 20°C / hPa [80]	Boiling point / °C [80]	S ₀ → S ₁ 0–0 energy gap / cm ⁻¹	S ₀ → S ₂ 0–0 energy gap / cm ⁻¹
Toluene		29,1	111	37476 [81]	47016 [81]
1,2,4-Trimethylbenzene		2,0	170	36435 [81]	
Anisole		3,6	154	36394 [82]	
Naphthalene		0,086	218	30200 [81]	35900 [49]
1-Methyl-naphthalene		0,054	244,6	29720* [49, 81]	

*: Extrapolated from the difference of benzene und toluene and scaled to naphthalene

The present work extends the range of measured effective fluorescence lifetimes to pressures below atmospheric in a temperature range from 300 to 475 K. This allows to distinguish between

fast intramolecular (internal conversion and intersystem-crossing) and collision-induced energy transfer processes in the excited state and thus gives valuable input for modeling the underlying photo-physical processes. Following the concept used by Cheung and Hanson [9] for 3-pentanone, rate constants for the underlying processes can be determined that are essential for photo-physical models that predict fluorescence quantum yields as a function of excitation energy, temperature, pressure and bath gas composition. A special emphasis lays on the ratio of the rate constants and the frequency of intermolecular collisions.

In the present work we analyze the dependence of effective fluorescence lifetimes of the benzene derivatives toluene, anisole, 1,2,4-trimethylbenzene, naphthalene, and 1-methylnaphthalene (Table 4) on total pressure between 0.01 and 1 bar at temperatures between 296 and 475 K. Electronic excitation is accomplished using picosecond pulses at 266 nm in gas-phase samples diluted in CO₂ as bath gas.

5.1.2 Theoretical background

All the species considered here can be excited in the UV via an allowed $\pi \rightarrow \pi^*$ transition. The electronic structure of the species considered here differs and Table 4 shows the energy gaps between the ground state and the involved excited singlet states. Therefore, for the various species, excitation at a given frequency leads to the population of different vibrationally-excited states in the first singlet state S_1 . For naphthalene, laser excitation at 266 nm is even sufficient to populate both the S_1 and the S_2 (35900 cm⁻¹) states at room temperature [49]. At higher temperatures even excitation of the S_3 state (47500 cm⁻¹) is possible. For toluene absorption of 266 nm photons leads to the population of the S_1 state only. Only at higher temperatures (> 600 K) the S_2 (47016 cm⁻¹) state can be populated as well [81]. In both cases, rapid internal conversion (on the femtosecond timescale) transfers the population to the S_1 state. This effect is known as Kasha's rule that describes the observation that fluorescence occurs from the S_1 state only. The rate of internal conversion can be estimated to be an exponential decay with the energy gap between the excited singlet states:

$$k_{IC} = 10^{13} f_v = 10^{13} \exp(-\alpha \Delta E) \quad (32)$$

The value α is 4.85 eV⁻¹ for, e.g., benzenoid aromatics. Because of the fast relaxation towards the S_1 state (~10 fs), in the following we ignore radiative processes originating from higher singlet states and from triplet states.

The following rate equation describes the intra-molecular deactivation (i.e., without collisions) of the excited molecules $[M^*]$ – neglecting re-absorption of fluorescence radiation [4, 65]:

$$\frac{d}{dt} [M^*] = (k_{fl} + k_{ISC} + k_{IC}) [M^*] \quad (10)$$

where k_{fl} , k_{ISC} , and k_{IC} are the rates for spontaneous fluorescence, intersystem crossing, and internal conversion, respectively (all in s⁻¹). In systems with collisions, the total depopulation rate, k_{tot} , can be expressed in terms of a measurable quantity, the effective fluorescence lifetime, τ_{eff} ,

using the following relation:

$$k_{\text{tot}} = \sum k_i = k_{\text{fl}} + k_{\text{NR}} = k_{\text{fl}} + k_{\text{IC}} + k_{\text{ISC}} + \sum k_{\text{q},j} n_{\text{q},j} = \frac{1}{\tau_{\text{eff}}}, \quad (13)$$

with k_{NR} as the non-radiative decay rate (s^{-1}) as the sum of k_{ISC} and k_{IC} . $k_{\text{q},j}$ is the quenching rate coefficient (in cm^3/s), with $n_{\text{q},j}$ (in m^{-3}) as the concentration of the quencher species j . Another parameter related to τ_{eff} is the fluorescence quantum yield, ϕ_{fl} :

$$\phi_{\text{fl}} = \frac{k_{\text{fl}}}{k_{\text{tot}}} = \frac{\tau_{\text{eff}}}{\tau_{\text{fl}}} = k_{\text{fl}} \tau_{\text{eff}} \quad (14)$$

with the natural lifetime τ_{fl} [65] given by (10) as the reciprocal fluorescence rate k_{fl} , τ_{fl} describes the theoretical fluorescence lifetime in absence of other decay channels. Thus, the fluorescence quantum yield is proportional to the effective fluorescence lifetime.

All the rate constants mentioned above depend on the vibrational excitation in the respective electronic state. Because various vibrational states are populated at the same time, a wide range of rate constants is active simultaneously. Due to Boltzmann statistics, the variability increases with temperature. For simplicity, often the photo-physical behavior of a single state with an energy corresponding to the average thermal energy is used for calculations to represent the entire distribution. The value of this average thermal energy is:

$$E_{\text{therm},n} = \sum_{i=1}^N \frac{E_{\text{vib},i}}{\exp(1.44 E_{\text{vib},i}/kT) - 1} \quad (30)$$

with $E_{\text{vib},i}$ as the energy of the vibrational states in the respective electronic state. At low total pressure (below 10 mbar) no collisions with bath-gas molecules take place before the excited molecule is deactivated via fluorescence. In this case and without any quenching, the expression

$$\phi_{\text{fl}} = \frac{k_{\text{fl}}}{k_{\text{fl}} + k_{\text{nr}}} \quad (5)$$

can be used to describe the fluorescence quantum yield.

5.1.3 Experiment and data evaluation

Fluorescence measurements were performed in a static stainless steel cell. Determined by preceding measurements, 2 μl of the liquid tracer (either as a liquid or dissolved in dodecane) were injected and the cell was filled with CO_2 to reach the desired total pressure. The cylindrical cell is 126 mm high with an inner diameter is 40 mm. Three 25 mm diameter quartz windows placed in o-ring-sealed flanges with 10 mm clear aperture allow optical access for the laser beam and fluorescence detection perpendicular to the laser beam. The cell is placed on top of a heating plate wrapped with heating wires. The gas temperature was measured with a K-type thermocouple placed inside the cell near the optical probe volume. The maximum achievable temperature was 500 K. The pressure was adjusted with a diaphragm valve and measured by a pressure transducer (Keller PAA-41/1-bar/8885).

Toluene, anisole, 1,2,4-trimethylbenzene, and 1-methylnaphthalene (Merck Chemicals, Analysis

Grade), all being liquid at room temperature, were used as a pure substance, while 10 wt% naphthalene (Merck Chemicals, Analysis Grade) was dissolved in dodecane (Sigma-Aldrich; >99% purity). Because the experiment focused on lifetime measurements and not on absolute fluorescence intensities, the exact concentration was not important. CO₂ (Air Liquide, purity 4.6) was provided from a gas cylinder. The liquids were injected into the cell through a septum. This resulted in approximately 4 mbar tracer vapor. Before each measurement the cell was evacuated to a pressure of ~10 mbar by a membrane pump (Vacubrand MD4C) and then was flushed with CO₂ to minimize oxygen contamination. The leakage rate was 20 mbar/h which had a negligible effect during the measurement time of 30 s. This was additionally confirmed by comparing 1,2,4-trimethylbenzene fluorescence lifetimes from the present experiment with measurements in a flow cell in pure N₂. Differences were within the measurement error (i.e., below 3%).

The optical setup is shown in Figure 17. A flashlamp-pumped frequency-quadrupled Nd:YAG laser (Ekspla, PL2143B) delivered pulse energies of 0.5 mJ at 266 nm with pulse lengths of 26 ps at a repetition rate of 10 Hz. The diameter of the circular laser beam was reduced to 4 mm by a Galilei telescope yielding a laser fluence of 4.5 mJ/cm². The signal was collected perpendicular to the laser beam by a set of spherical quartz lenses (200 and 50 mm focal lengths), discriminated against elastically scattered light with glass filters (Schott UG11 and UG1 for one- and two-ring aromatics, resp.) and detected by a fast photomultiplier (Hamamatsu H6780-04, rise time 0.78 ns). The signal was recorded by a digital oscilloscope (Tektronix TDS7404B, 4 GHz bandwidth) that was triggered by a photodiode recording laser stray light from a mirror. To improve signal-to-noise ratios, typically 200 fluorescence decay curves were averaged.

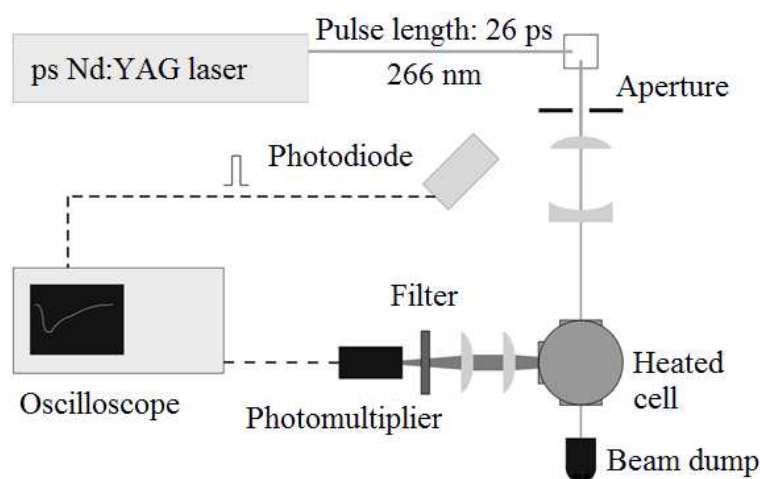


Figure 17: Experimental arrangement for time-resolved laser-induced fluorescence measurements.

To check for a linear response, the fluorescence intensity was recorded as a function of laser fluence (not shown here) and was found to be linear up to 6 mJ/cm² at 298 K for toluene. In additional measurements it was confirmed that the number density achieved with 2 μ l of the tracer solutions was low enough to not cause self-quenching of the fluorescence signal. Laser and signal attenuation was negligible (<2%) for the given concentrations and path lengths.

5.1.4 Data analysis

The left panel in Figure 18 shows the time-resolved LIF signals of toluene after picosecond excitation at 298 and 476 K after subtraction of the background signal (measured in the evacuated cell). The inset shows the signals in logarithmic scale vs. time together with mono-exponential fits. Mono-exponential fits yielded equally good results for 1,2,4-trimethylbenzene and anisole. The right panel in Figure 18 shows LIF-signal traces for 1-methylnaphthalene at 323 and 523 K. Bi-exponential decays were observed for 1-methylnaphthalene and naphthalene that deliver a slow and fast fluorescence lifetime component with amplitudes representing the respective contribution to the total measured signal trace.

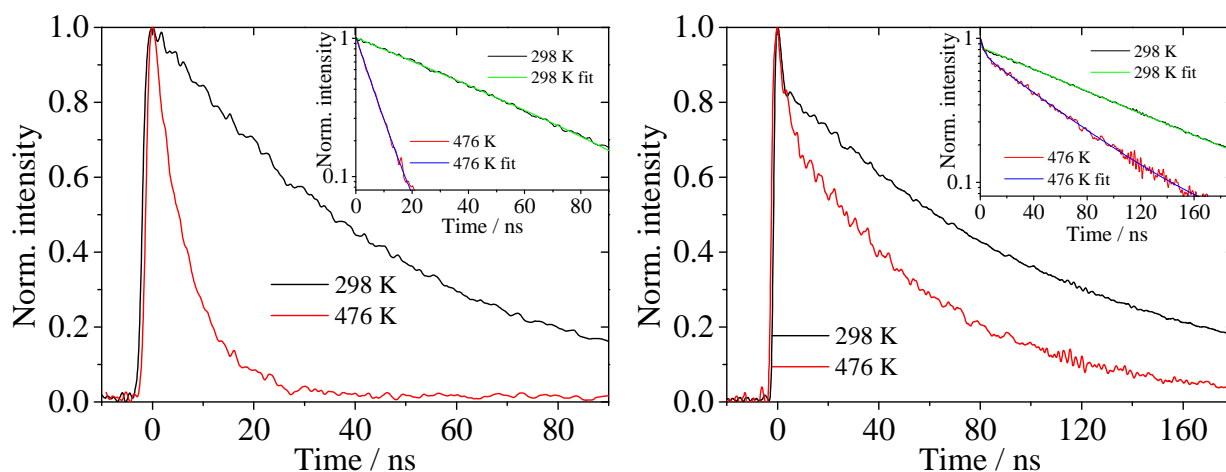


Figure 18: Left: Toluene-LIF signal decay after excitation at 266 nm at 298 and 476 K in 1024 mbar CO₂. The inset shows the decay in a logarithmic plot with a mono-exponential fit. The resulting fluorescence lifetime was 45 and 37 ns, resp. Right: 1-methylnaphthalene-LIF decay curve after excitation with 266 nm at 323 and 476 K in 1024 mbar CO₂. The inset shows the decay in a logarithmic plot with a bi-exponential fit. For 323 and 476 K, the resulting fluorescence lifetime were 112 and 49 ns for the long component and 2.1 and 1.7 ns for the short component, resp.

5.1.5 Results

Toluene

Figure 19 presents fluorescence lifetimes of toluene as a function of total pressure for various temperatures. Except for the lowest pressure at 298 K the lifetimes decrease with increasing pressure for all temperatures with this trend being more obvious at higher temperature. The difference in lifetime between 10 mbar and atmospheric pressure changes from -45% at 355 K to -79% at 475 K. The variation of the fluorescence lifetime with pressure can be described by mono-exponentials with offset (due to the lifetime at infinite pressure) as shown in Figure 19 as lines. With this fit it is possible to extrapolate the lifetimes to the collision-free regime at 0 bar and calculate the fluorescence (k_f) and non-radiative (k_{NR}) rate constants. These as well as the fit parameters are given in Table 5 and 6.

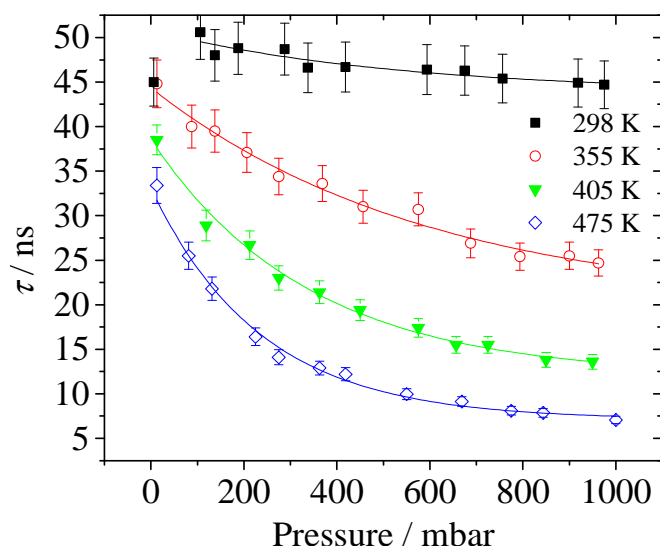


Figure 19: Dependence of the effective lifetime of toluene LIF (symbols) on total pressure at four temperatures. The lines represent mono-exponential fits to the data (the data point at 10 mbar and 298 K was neglected). 4 mbar toluene, CO₂ bath gas, 266 nm excitation. Fit parameters given in Table 5.

1,2,4-Trimethylbenzene

Figure 20 shows pressure-dependent fluorescence lifetimes of 1,2,4-trimethylbenzene for various temperatures together with mono-exponential fits for each temperature. For this species at 298 K the lifetime slightly increases with pressure but decreases for all other temperatures. The difference in lifetime between 10 mbar and atmospheric pressure changes from +12% at 298 K to -72% at 475 K.

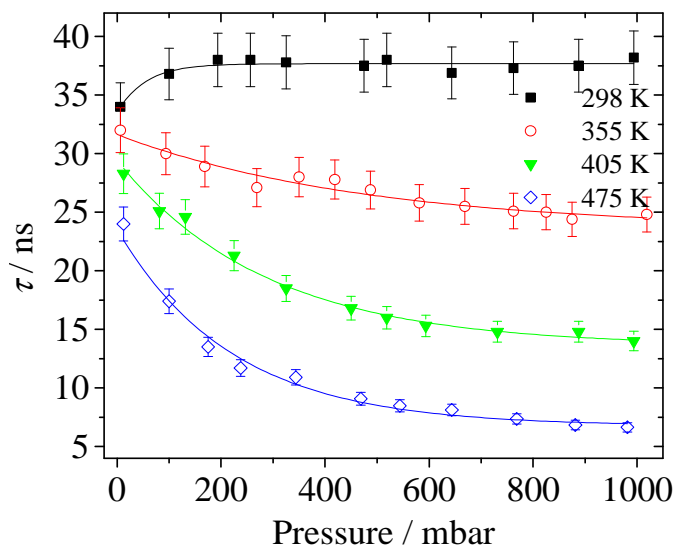


Figure 20: Dependence of the effective fluorescence lifetime of 1,2,4-trimethylbenzene (symbols) on total pressure at four temperatures. Solid lines represent mono-exponential fits to the data. 4 mbar 1,2,4-trimethylbenzene, CO₂ bath gas, 266 nm excitation. Fit parameters given in Table 5.

Anisole

Figure 21 shows the pressure-dependent fluorescence lifetimes of anisole for various temperatures together with mono-exponential data fits for each temperature. In comparison to 1,2,4-trimethyl-

benzene, a pressure-dependent increase in lifetime is visible for the lower two temperatures, which then switches to a pressure-dependent decrease for the two higher temperatures investigated here. The estimated transition temperatures between these two regimes are roughly 400 and 326 K for anisole and 1,2,4-trimethylbenzene, respectively. The change in lifetime from 10 mbar to atmospheric pressure is +18% at 298 K and -35% at 475 K.

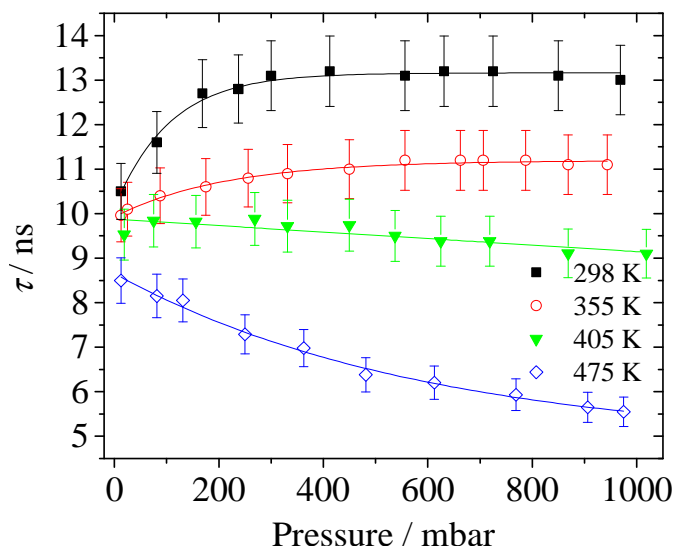


Figure 21: Dependence of the effective fluorescence lifetime of anisole (symbols) on total pressure at four temperatures (symbols). Solid lines represent mono-exponential fits to the data. 4 mbar anisole, CO₂ bath gas, 266 nm excitation. Fit parameters given in Table 5.

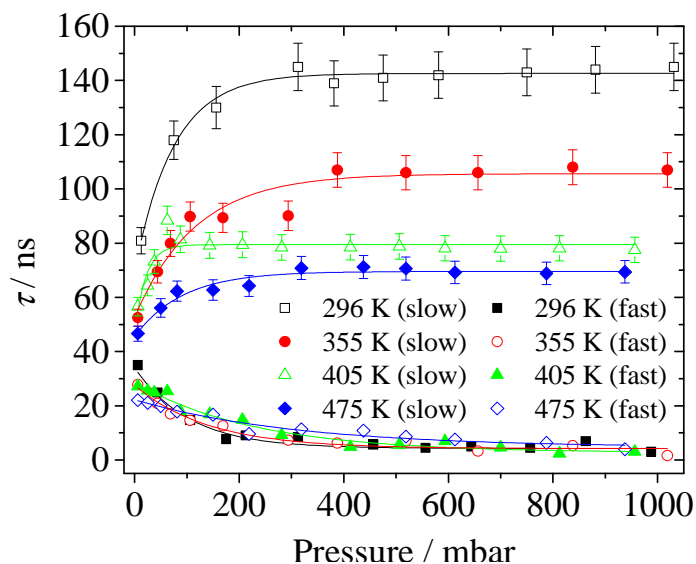


Figure 22: Dependence of the effective fluorescence lifetime of naphthalene (symbols) on total pressure at four temperatures. Solid lines represent mono-exponential fits to the data points. 4 mbar naphthalene, CO₂ bath gas, 266 nm excitation. Fit parameters given in Table 5.

Naphthalene

Figure 22 shows the pressure-dependent fluorescence lifetimes of naphthalene for various temperatures together with mono-exponential fits for each temperature. The slow and the fast lifetime components were extracted by applying a bi-exponential fit to the measured fluorescence decay

profiles. For the slow lifetime components (solid symbols in Figure 22), a variation in lifetime with increasing pressure is visible for all investigated temperatures. The increase in lifetime from 10 mbar to atmospheric pressure decreases from +79% at 298 K to +49% at 475 K. The pressure dependence shown here corresponds well to the data of Beddard et al. [83] and Ossler et al. [6]. The data in [83] was obtained using various laser excitation energies at fixed temperature rather than a common wavelength at variable temperatures, verifying that both methods are alternatives to reach various (average) excited state energies and share the same theoretical background.

Although the fast lifetime component could not be extracted from the fits precisely enough for pressures above 500 mbar due to the limited rise time of the photomultiplier (0.8 ns [84]), its contribution at low pressure cannot be neglected. At the lowest pressure the amplitude of the fitted exponentials of both lifetime components indicate almost equal contributions from both fluorescence decay channels. Therefore, the relative contribution of both decay channels was evaluated from the relative amplitudes of the bi-exponential fit at 10 mbar (2/1, 2.5/1, 3.2/1, and 2.2/1 for 296, 355, 405, and 475 K, respectively).

1-Methylnaphthalene

Figure 23 shows the fluorescence lifetimes of 1-methylnaphthalene for various temperatures together with mono-exponential fits for each temperature. Like for naphthalene, the slow and fast lifetime components were determined from bi-exponential fits to the measured fluorescence decay profiles. For the slow lifetimes, an increase with increasing pressure is visible for all temperatures investigated. The increase in lifetime from 10 mbar to atmospheric pressure decreases from +72% at 298 K to +37% at 475 K.

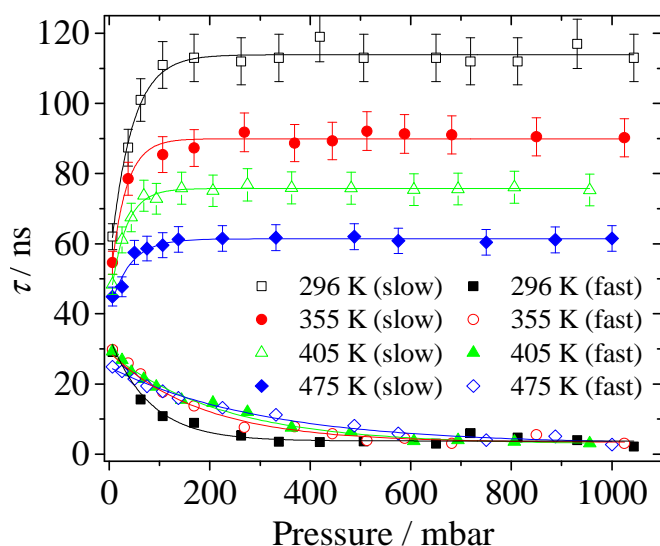


Figure 23: Dependence of the effective fluorescence lifetime of 1-methylnaphthalene (symbols) on total pressure at four temperatures. Solid lines represent mono-exponential fits to the data points. 4 mbar 1-methylnaphthalene, CO₂ bath gas, 266 nm excitation. Fit parameters given in Table 5.

Again, the fast lifetime component could not be extracted precisely for pressures above 500 mbar, but its contribution at low pressure cannot be neglected. The amplitude ratios of both lifetime components at 10 mbar were 1.6/1, 4.5/1, 4/1, and 3/1 for 296, 355, 405, and 475 K, respectively. A weighted average of both lifetime components with their intensity was used to calculate the natural lifetime and rate constants, just like for naphthalene.

Table 5: Fit parameters (equation: $\tau(p)/\text{ns} = A \exp\left(-\frac{p/\text{mbar}}{B}\right) + y_0$; τ : effective lifetime; p : pressure; A , B , y_0 : fit parameters) derived from the fluorescence decay profiles after 266 nm excitation of the investigated aromatics. The fluorescence lifetime extrapolated to zero pressure, τ_0 is the sum of A and y_0 .

Temperature	Parameter	Toluene	1,2,4-Tri-methyl-benzene	Anisole	Naphthalene*	1-Methyl-naphthalene*
296 K	A	7.004	-4.141	-3.0455	-72.64/29.78	-80.36/29.64
	B	524.8	54.81	13.1614	74.97/103.9	42.49/79.94
	y_0	43.80	37.68	104.88	142.6/4.275	113.9/3.745
	$\tau(0)/\text{ns}$	50.8	33.5	10.1	45.7	42.3
355 K	A	24.67	8.060	-1.2689	-54.24/23.42	-43.34/27.64
	B	595.4	477.6	11.1946	102.0/140.8	30.06/161.8
	y_0	19.70	23.57	211.974	104.4/4.213	89.92/3.668
	$\tau(0)/\text{ns}$	44.4	31.6	9.93	35.0	32.3
405 K	A	26.54	15.82	92065	-30.90/25.91	-33.64/26.17
	B	338.0	287.7	$1,275 \times 10^8$	23.38/230.7	30.10/226.4
	y_0	12.01	13.59	-92055	79.26/2.703	75.73/2.767
	$\tau(0)/\text{ns}$	38.4	29.4	9.88	32.9	31.6
475 K	A	25.96	16.78	3.8287	-24.07/17.63	-20.19/22.00
	B	235.9	222.1	591.18	91.77/311.7	42.38/305.0
	y_0	7.115	6.751	4.8268	69.58/4.598	61.44/2.805
	$\tau(0)/\text{ns}$	33.0	23.5	8.66	29.5	28.8

*Parameter for short/long lifetime component

Rate constant overview

Using equations (5), (14), and the absolute fluorescence quantum yield from literature [85], the natural lifetimes at 298 K and 266 nm and the rate constants k_{fl} and k_{NR} were determined for each tracer using extrapolated lifetimes for 0 mbar at 298 K. For the tracers with bi-exponential signal decays, both lifetime components were weighted with their amplitude at 10 mbar to determine an effective lifetime. The resulting error for extrapolation is around 28% for 1-methylnaphthalene and around 4% for the other tracers. The results are listed in Table 6. The obtained rate constants for toluene and naphthalene are in good agreement with previous data presented by Hsieh et al. [46], Jacon et al. [30], and Burton and Noyes [17].

Table 6: Natural lifetime τ_{fl} and rate constants k_{fl} and k_{NR} derived from τ_0 . For naphthalene and 1-methylnaphthalene a slow and fast lifetime component were extracted (see text) and weighted with the fit-derived amplitude for further calculation.

	Toluene	1,2,4-Trimethylbenzene	Anisole	Naphthalene *	1-Methylnaphthalene *
τ_{fl}/ns	230.9	81.8	28.1	108.8	100.6
$k_{fl}/10^6\text{ s}^{-1}$	4.33	12.2	35.6	9.19	9.93
$k_{NR}(296\text{ K})/10^6\text{ s}^{-1}$	15.4	17.6	63.2	12.7	13.7
$k_{NR}(355\text{ K})/10^6\text{ s}^{-1}$	19.4	19.4	65.1	19.4	21.0
$k_{NR}(405\text{ K})/10^6\text{ s}^{-1}$	21.8	21.8	65.6	21.2	21.7
$k_{NR}(475\text{ K})/10^6\text{ s}^{-1}$	26.0	30.3	79.9	24.7	24.8

5.1.6 Discussion

In the following, an effort is made to rationalize the observations described above. Anisole will be discussed first since it displays both pressure dependencies in the temperature range that was analyzed. From previous studies of the energy levels in the S_0 and S_1 states, the 0–0 energy gap has been determined to be 36394 cm^{-1} [82] which in our experiments is 1200 cm^{-1} lower than the photon energy (266 nm laser, i.e. 37594 cm^{-1}). Because the vibrational energy level structure is different for the S_0 and S_1 states, the average thermal energy level (called in accordance with literature the thermal energy level E_{therm} , cf., eq. 30) has a somewhat different energy gap (note, with increasing temperature, in general E_{therm} in S_1 shifts more quickly to higher energies than in S_0 , due to the higher density of the states in S_1). After laser excitation, the initial population in the S_1 state differs from the thermal population in the S_1 state. The initial population depends on the laser wavelength (fixed here) and the temperature, i.e., the thermal population in the S_0 state. At a given temperature the difference in the average energy of the initial distribution (E_{initial}) and the thermal energy level E_{therm} can be calculated based on known vibrational energies in both electronic states. For toluene and naphthalene, such vibrational energy levels are known with sufficient accuracy [86].

For anisole at room temperature and 266 nm excitation, E_{initial} is above E_{therm} , shown as heavy purple line in Figure 24 (left). The excess vibrational energy (“photo-induced heating”) is randomized within the molecule and in case of collisions transferred to the bath gas causing stepwise relaxation towards the thermalized condition with E_{therm} . This collisional relaxation becomes faster with increasing pressure. The rates of the non-radiative decay processes (i.e., IC and ISC) are state dependent and their rates increase with increasing vibrational energy. Collisional relaxation therefore reduces losses through these competing channels and more molecules are able to fluoresce. In the case of anisole at room temperature this can be seen by the increase of the fluorescence lifetime (i.e., fluorescence quantum yield) with pressure (filled squares in Figure 21, reproduced as inset in Figure 24).

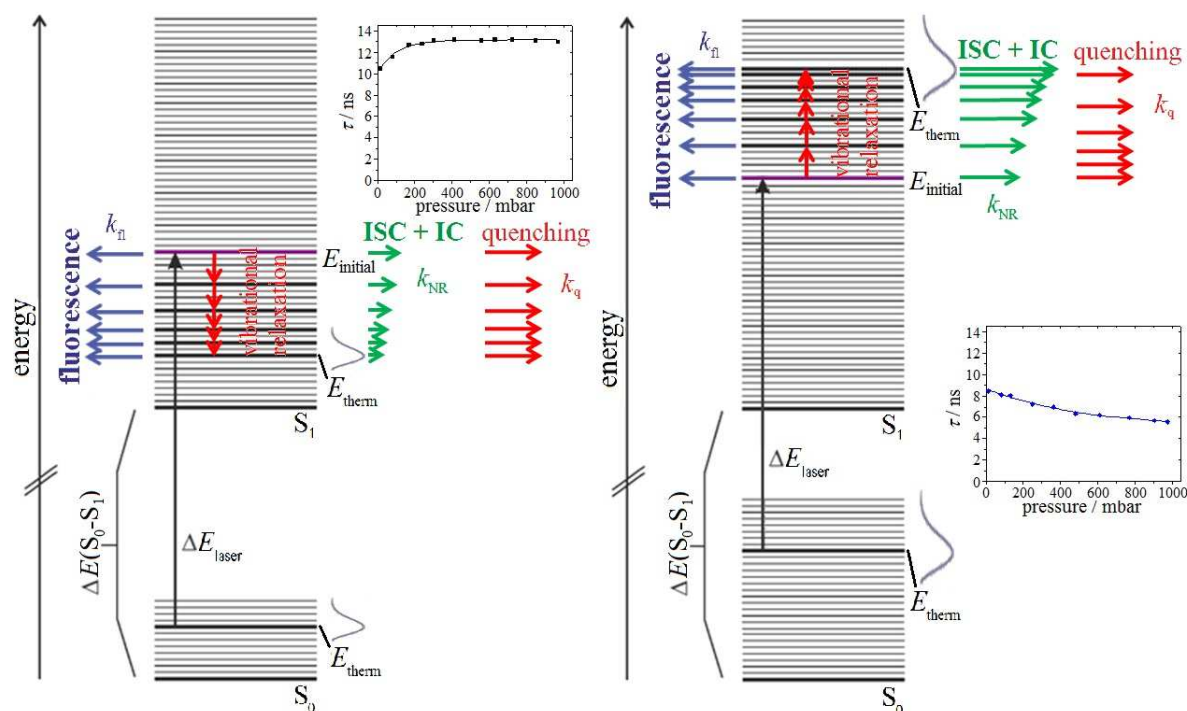


Figure 24: Schematic Jablonski diagram for anisole at room temperature, the lengths of the horizontal arrows for k_{NR} indicates the relative rate constants. ΔE_{therm} is the center of gravity of the thermal Boltzmann distribution in each state. ΔE_{laser} corresponds to 266 nm excitation. Left: $E_{\text{initial}} > E_{\text{therm}}$ leading to laser-induced heating, right: $E_{\text{initial}} < E_{\text{therm}}$ leading to laser-induced cooling.

With increasing temperature a transition regime is reached where E_{initial} equals E_{therm} and where the fluorescence quantum yield becomes pressure independent. At even higher temperatures, E_{initial} is below E_{therm} (Figure 24, right) and collisions lead to a cooling of the bath gas – a process referred to as photo-induced cooling [45, 79]. Collisions populate higher states in the electronically state and thus, increased collision rates reduce the lifetime of the excited state and hence the fluorescence quantum yield. In the present case of anisole at the higher temperatures (starting at around 405 K, cf., Figure 21) these processes then also shorten the fluorescence lifetime with increasing pressure (cf., Figure 21 and inset in Figure 24.).

This general concept can be transferred to every other molecule investigated in this study. The 0–0 energy gap of 1,2,4-trimethylbenzene is slightly higher than that for anisole (36435 cm^{-1} [81]). Therefore, the decrease of the fluorescence lifetime with increasing pressure starts at lower temperatures compared to anisole (Figure 20). For toluene, the 0–0 energy gap is so large (37476 cm^{-1} [81]) that for all temperatures investigated in this work, excitation at 266 nm leads to $E_{\text{initial}} < E_{\text{therm}}$, which causes a decrease in fluorescence lifetime with increasing pressure (cf., Figure 19). For naphthalene and 1-methylnaphthalene the case is much more complicated. The 0–0 energy gap for naphthalene is much smaller (30200 cm^{-1} [49]) compared to that of one-ring aromatics. This is well mirrored by the strong increase of the long fluorescence lifetime component with increasing pressure, even at 475 K (cf., Figure 22). This behavior was explained in the previous section for mono-aromatics. However, there is no explanation for the origin of the additional second-

ary lifetime component as well as its pressure dependence. The energy gap between the S_0 and S_2 state is only 35900 cm^{-1} [49] and hence also accessible with 266 nm radiation. This might be a hint for an explanation but further studies have to be conducted to find out more about this process. The same applies to 1-methelnaphthalene.

5.1.7 Conclusions

Effective fluorescence lifetimes of toluene, 1,2,4-trimethylbenzene, anisole, naphthalene, and 1-methylnaphthalene were measured after picosecond laser excitation at 266 nm and at temperatures between 298 and 475 K and pressures between 0.01 and 1 bar. Experiments were performed in a heated static optical cell with CO_2 as buffer gas. The data obtained provide a first systematic evidence of the effect of photo-induced cooling [45, 79] in anisole and 1,2,4-trimethylbenzene. This effect explains the species-specific characteristic variation of effective fluorescence lifetimes with pressure at fixed temperatures. For naphthalene and 1-methylnaphthalene, a slow and fast lifetime component was determined similar to Ossler et al [6]. A more in-depth investigation of these is necessary. In addition, this data is consistent with laser excitation variation measurements done by Beddard et al. [83].

Fluorescence and non-radiative rate constants have been determined using collision-free lifetimes extrapolated from the measured values to zero pressure. The obtained rate constants for toluene and naphthalene are in good agreement with previous data presented by Hsieh et al. [46], Jacou et al. [30], and Burton and Noyes [17]. For 1,2,4-trimethylbenzene, anisole, and 1-methylnaphthalene, no literature data is available so far. The parameters measured are needed for step-ladder fluorescence models to predict fluorescence quantum yields for these aromatics that are frequently employed as tracer species for quantitative gas mixing studies [20] and thermometry [87]. Such models yet need to be developed for 1,2,4-trimethylbenzene, anisole, and 1-methylnaphthalene. For this purpose the experimental data base initiated in this work needs to be extended to higher temperatures relevant in many areas of application of tracer LIF, e.g., engine combustion.

5.2 Self-quenching in toluene LIF

The following chapter is based on the journal paper "Self-quenching in toluene LIF", published in Proceedings of the Combustion Institute 36, 2017, 4505–4514 by Daniel Fuhrmann, Torsten Benzler, S. Fernando, Torsten Endres, Sebastian Kaiser, Thomas Dreier, and Christof Schulz.

Abstract

Toluene is frequently used as laser-induced fluorescence (LIF) tracer for visualizing mixing processes, for example, in internal combustion engines. The signal evaluation relies on a linear dependence of the LIF signal on tracer concentration – which is not present in many practically relevant cases. This paper presents an investigation of the dependence of the LIF signal intensities on the toluene concentration, revealing a non-linear signal response already at concentrations approximately ten times below those given by the room-temperature vapor pressure. Toluene was vaporized in a mass-flow controlled evaporator and investigated in a free jet. Nitrogen was used as bath gas with a variable addition of oxygen. After excitation at 266 nm, an intensified CCD camera recorded the spectrally filtered fluorescence. In separate experiments, the effective fluorescence lifetime upon picosecond UV-laser excitation was determined. The results indicate that the fluorescence lifetime decreases with increasing tracer concentration due to self-quenching. Results from imaging and fluorescence lifetime measurements are consistent. The investigation reveals that the self-quenching of toluene is dominated by collisions with excited-state toluene molecules, which causes an additional dependence of the magnitude of self-quenching on the laser fluence.

5.2.1 Introduction

5.2.1.1 Tracer LIF

Laser-induced fluorescence (LIF) can be used for spatio-temporally resolved imaging of gas-phase mixing processes, temperature, and concentration in internal combustion engines and other combustion applications. For quantitative measurements, fluorescent tracers may be added to a non-fluorescing surrogate fuel. Ketones, aromatics, and amines are commonly used groups of tracers [4, 88, 89]. Their spectroscopic properties such as the variation of the absorption cross-section and the fluorescence quantum yield as a function of temperature and oxygen concentration have been studied to support quantitative evaluation of measured signal intensities [20]. Recent comparisons of various tracers are presented in Refs. [42, 90]. Toluene is frequently used because its evaporation characteristics are comparable to that of gasoline [57], the response to oxygen quenching [55, 58] and temperature [24, 59, 91] can be useful under certain conditions, and the LIF signal is particularly strong in N_2 .

In measurements in which the quantity of interest is the tracer number density n_{tr} , it is usually assumed that, everything else being equal, the LIF-signal intensity S_{fl} scales linearly with that number density (as well as with the absorption cross section, σ_{abs} , the fluorescence quantum yield, ϕ_{fl} , and the laser fluence, I_{laser}):

$$S_{\text{fl}} \propto n I_{\text{laser}} \sigma_{\text{abs}} \phi_{\text{fl}} \quad (1)$$

Corrections for background signal and the response of the imaging system then allow simple conversion of the measured LIF intensity into at least a relative local tracer concentration.

The fluorescence quantum yield is also related to the fluorescence lifetime [65]:

$$\phi_{\text{fl}} = \frac{k_{\text{fl}}}{k_{\text{tot}}} = \frac{k_{\text{fl}}}{k_{\text{fl}} + k_{\text{NR}} + k_{\text{q}}} = \frac{\tau_{\text{eff}}}{\tau_{\text{fl}}} = \text{const.} \tau_{\text{eff}} \quad (16)$$

with k_{fl} denoting the rate of spontaneous fluorescence emission, k_{tot} the rate for the sum of all decay pathways, and τ_{eff} the effective fluorescence lifetime and τ_{fl} the fluorescence lifetime in absence of other decay channels.

Tracer-LIF measurements are often affected by limited signal-to-noise ratios. There are three ways to increase the signal: (i) increasing laser fluence (which is limited by non-linear signal response, see Figure 27), (ii) decreasing collisional quenching (e.g., carrying out measurements in N_2 instead of air), and (iii) increasing the tracer concentration (which is limited by the saturated vapor concentration at the lowest process temperature, in case of toluene: 2.85 vol% at room temperature). All these strategies can have a detrimental effect due to the often-overlooked influence of laser fluence and collisional energy transfer between the tracer molecules, i.e., self-quenching. This can lead to erroneous concentration measurements and might even affect spectroscopic measurements that are the basis for signal interpretation.

Deviations from Eq. (38) with increasing fluence are often described as ‘‘saturation’’ which in the simplest case changes this dependence to

$$S_{\text{fl}} \propto n I_{\text{laser,sat}} \frac{1}{1 + I_{\text{laser,sat}}/I_{\text{laser}}} \sigma_{\text{abs}} \phi_{\text{fl}} = n I_{\text{laser,eff}} \sigma_{\text{abs}} \phi_{\text{fl}} \quad (33)$$

with $I_{\text{laser,sat}}$ being the saturation [2] and $I_{\text{laser,eff}}$ the resulting effective laser fluence. This non-linear response to laser fluence can be attributed, e.g., to ground-state depletion, laser-induced emission, and laser-induced effects in the excited state (such as further electronic excitation, ionization, or photo-fragmentation). In many cases (as for toluene) it is not clear yet what actually is the responsible effect. In all previous cases, the non-linear effects attributed to saturation have not been linked to self-quenching, and a dependence on the tracer concentration has not been investigated. There is some concern, however, that some of the effects attributed to saturation are really self-quenching and thus, saturation studies at high tracer concentrations (such as, e.g., Ref. [92]) might in fact have looked at combined effects.

In this work, we investigated the dependence of the LIF signal on toluene concentration in pure nitrogen (N_2) and in N_2 with variable oxygen (O_2) concentrations as a bath gas. One experiment was intended to represent a typical situation for LIF imaging: time-integrated quantitative two-dimensional imaging of a free jet. Additionally, fluorescence lifetime measurements were conducted with picosecond laser excitation and time-resolved detection. The measurements were carried out at room temperature for a wide range of tracer concentrations and laser fluence.

5.2.1.2 Toluene photophysics

Table 7 lists the photo physical processes relevant in the context of this paper. Absorption of a UV photon leads to population of toluene in the S_1 state and fluorescence can be emitted with the rate k_{fl} . Variations of the fluorescence quantum yield due to (collisionally induced) relaxation in the vibrational manifold of S_1 with resulting variations in intersystem crossing and internal conversion modify the rate of intramolecular losses k_{tot} . These complex variations are described elsewhere (e.g., [23]) and are not of interest here.

Table 7: Photo physical processes relevant in the context of this work: 1A : Toluene in S_0 , ${}^1A^*$: Toluene in S_1 , ${}^nA^*$: excited state toluene (multiplicity n unspecified), A : toluene in unspecified state.

Absorption	${}^1A + h\nu \xrightarrow{k_{abs}} {}^1A^*$
Fluorescence	${}^1A^* \xrightarrow{k_{fl}} {}^1A + h\nu$
Quenching by O_2	${}^1A^* + {}^3O_2 \xrightarrow{\tilde{k}_q^{O_2}} {}^3A + {}^1O_2$
Self-quenching	${}^1A^* + {}^1A \xrightarrow{\tilde{k}_q^{tr}} 2 {}^1A$
	${}^1A^* + {}^nA^* \xrightarrow{\tilde{k}_q^{tr*}} {}^1A + A$

Intermolecular energy losses occur through collisional quenching. For aromatic compounds, O_2 is an effective quencher and its quenching properties have been studied in detail for toluene [93]. The excited molecule A^* is quenched by O_2 in the triplet state. The oxygen quenching-rate is the product of the O_2 number density n_{O_2} and the bimolecular quenching rate coefficient $\tilde{k}_q^{O_2}$ [58].

With increasing tracer concentration, tracer–tracer collisions gain importance, leading to the possibility of self-quenching. For small molecules like nitric oxide (NO) and nitrogen dioxide (NO_2), this behavior is well-known and the self-quenching rate constants have been determined by measuring the concentration dependence of the fluorescence lifetime [72, 73]. In these studies, the fluorescence decay rate showed a linear dependence on the tracer’s partial pressure, which was attributed to collisions of the excited tracer A^* with ground-state molecules A . The effect of self-quenching is then fully represented by the self-quenching rate coefficient \tilde{k}_q^{tr} and the tracer number density n .

For some larger aromatic molecules like anthracene [74] and pyrene [75], self-quenching has been investigated in detail. The self-quenching rates of pyrene and anthracene exhibit a negative temperature dependence and the activation energy determined from the observed temperature dependence is in the order of the binding energy of the relevant excimers $(AA)^*$. Through this observation and further supporting kinetic models, Davis et al. [75] suggest that the formation of an excimer is involved in the self-quenching process.

In Section 5.2.3 we will show that in case of toluene, self-quenching is dominated by collisions between excited-state toluene, A^* , with a number density of n^* and the rate coefficient \tilde{k}_q^{tr*} . We

assume that $n^* \sim I_{\text{laser,eff}} n_{\text{tr}}$. With tracer fluorescence quenched by both O_2 and the tracer itself (in the general case with both electronic ground state and excited state species), the LIF signal intensity S_{fl} given by Eq. (38) can then be written as:

$$S_{\text{fl}} \propto n_{\text{tr}} \sigma_{\text{abs}} I_{\text{laser,eff}} \frac{k_{\text{fl}}}{k_{\text{tot}} + \tilde{k}_{\text{q}}^{\text{O}_2} n_{\text{O}_2} + (\tilde{k}_{\text{q}}^{\text{tr}} + \tilde{k}_{\text{q}}^{\text{tr}*} I_{\text{laser,eff}}) n} \quad (34)$$

Thus, if self-quenching occurs, i.e., the term

$$\left(\tilde{k}_{\text{q}}^{\text{tr}} + \tilde{k}_{\text{q}}^{\text{tr}*} I_{\text{laser,eff}} \right) n \quad (35)$$

is not negligible, the LIF signal S_{fl} is no longer proportional to the tracer concentration n_{tr} .

Although self-quenching has been documented for several fluorescent species, it is usually ignored in tracer-based LIF imaging and even in spectroscopic experiments that aim at investigating the fluorescence quantum yield as a function of ambient conditions for later use in signal quantification.

An alternative way of describing the strength of the intermolecular deactivation process due to quenching is the Stern–Volmer relationship, which relates the signal in the presence of quenching, S_{fl} , to that without quenching, $S_{\text{fl},0}$:

$$\frac{S_{\text{fl},0}}{S_{\text{fl}}} = 1 + k_{\text{SV}}^{\text{O}_2} n_{\text{O}_2} + k_{\text{SV}}^{\text{tr}} n + k_{\text{SV}}^{\text{tr}*} n \quad (36)$$

$$\Leftrightarrow S_{\text{fl}} = \frac{S_{\text{fl},0}}{1 + k_{\text{SV}}^{\text{O}_2} n_{\text{O}_2} + k_{\text{SV}}^{\text{tr}} n + k_{\text{SV}}^{\text{tr}*} n} = \frac{a n_{\text{tr}}}{1 + k_{\text{SV}}^{\text{O}_2} n_{\text{O}_2} + k_{\text{SV}}^{\text{tr}} n + k_{\text{SV}}^{\text{tr}*} n} \quad (37)$$

k_{SV} are the so-called Stern–Volmer coefficients for the interaction with O_2 , A, and A^* , respectively:

$$k_{\text{SV}}^{\text{O}_2} = \frac{\tilde{k}_{\text{q}}^{\text{O}_2}}{k_{\text{tot}}}, k_{\text{SV}}^{\text{tr}} = \frac{\tilde{k}_{\text{q}}^{\text{tr}}}{k_{\text{tot}}}, k_{\text{SV}}^{\text{tr}*} = \frac{\tilde{k}_{\text{q}}^{\text{tr}*} I_{\text{laser,eff}}}{k_{\text{tot}}} \quad (38)$$

Note that here, $k_{\text{SV}}^{\text{tr}*}$ depends on the laser fluence. The proportionality between tracer concentration n_{tr} and the LIF signal in case of negligible quenching is accounted for by the proportionality constant a that is a function of laser intensity, absorption cross-section, detection efficiency, and other factors:

$$S_{\text{fl},0} = a n \quad (39)$$

Eqs. (1) and (16) show that varying fluorescence quantum yields (such as in the case of self-quenching) also affects the fluorescence lifetime,

$$\frac{S_{\text{fl},0}}{S_{\text{fl}}} = \frac{\tau_0}{\tau} \quad (40)$$

Here, everything else held constant, τ and τ_0 represent the fluorescence lifetime with and without the presence of a quencher. Thus, experimentally, two independent but equivalent ways of investigating the impact of tracer concentrations on the fluorescence quantum yield exist: measurement

of the time-integrated signal, S_{fl} , or the fluorescence lifetime τ . In this work, both methods were pursued.

5.2.2 Experiment

5.2.2.1 Time-integrated LIF imaging

Figure 25 shows the most important parts of the LIF-imaging experiment. The flow rate of liquid toluene was set by a syringe pump (KD Scientific KDS200). In a Venturi nozzle, the tracer was injected into a pre-heated and mass-flow controlled carrier gas flow of either N_2 , air, or mixtures of both. The two mass-flow controllers, MFC1 for N_2 and MFC2 for air, allowed maximum flow rates of 0.83 and 0.083 l/s, respectively. The total flow rate of the carrier gas was set to 0.5 l/s for all measurements. Hence, the carrier gas flow could contain O_2 at concentrations from 0 to 3.5 vol%. To avoid condensation of toluene at room temperature, the maximum toluene mass flow rate must stay below 55.4 mg/s (corresponding to a volume fraction of 2.85 vol%). After spray formation in the Venturi nozzle, the tracer evaporated and mixed with the carrier gas in a slightly heated plenum with a volume of 2.25 l. The gaseous mixture issued from a nozzle with 7.3 mm diameter as a vertical jet into the ambient air.

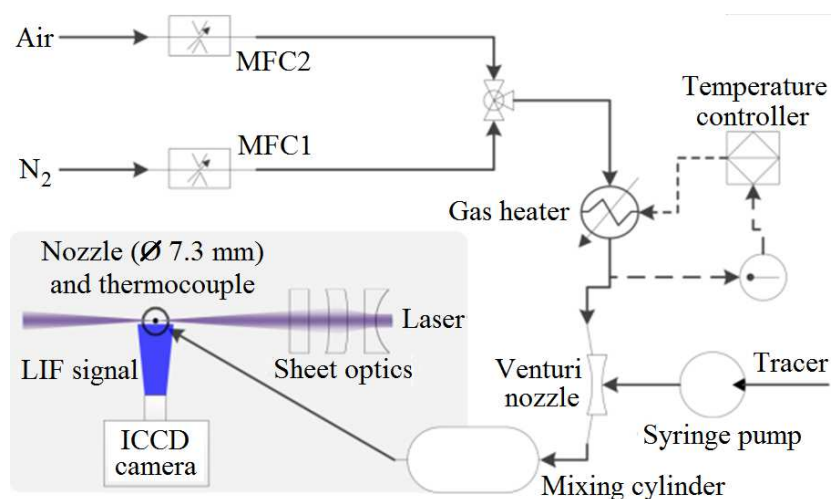


Figure 25: Schematics of the time-integrated LIF imaging experiment with the nozzle and optics in plain view.

The beam from a frequency-quadrupled Nd:YAG laser (266 nm, maximum energy at the probe volume 14.8 mJ/pulse, pulse duration 7 ns, repetition rate 10 Hz) was formed into a vertical 26 mm high light sheet, intersecting the gas jet's center line. The relative laser intensity as a function of the sheet-orthogonal direction was measured by the traversing knife-edge method using a photodiode. 80% of the energy was contained in the central 0.4 mm of sheet thickness, and is roughly Gaussian-distributed over that span. The maximum laser pulse energy resulted in an average fluence of $14.8 \text{ mJ} / (26 \times 0.4 \text{ mm}^2) = 142 \text{ mJ/cm}^2$ in the light sheet, while the corresponding peak fluence in the center of the light sheet is about 278 mJ/cm^2 . Reduced laser fluences were realized without changing the light sheet's intensity profile using a beam attenuator. The fluores-

cence signal was recorded with an intensified CCD camera with stray light being spectrally rejected by a long-pass filter (Semrock, 266 nm RazorEdge).

Figure 26 shows example images. After background correction, 100 single-shot images were averaged and the signal was spatially averaged within a region of interest (ROI) in the unmixed “potential core” of the jet, where no surrounding gases were entrained and where the illumination was homogeneous.

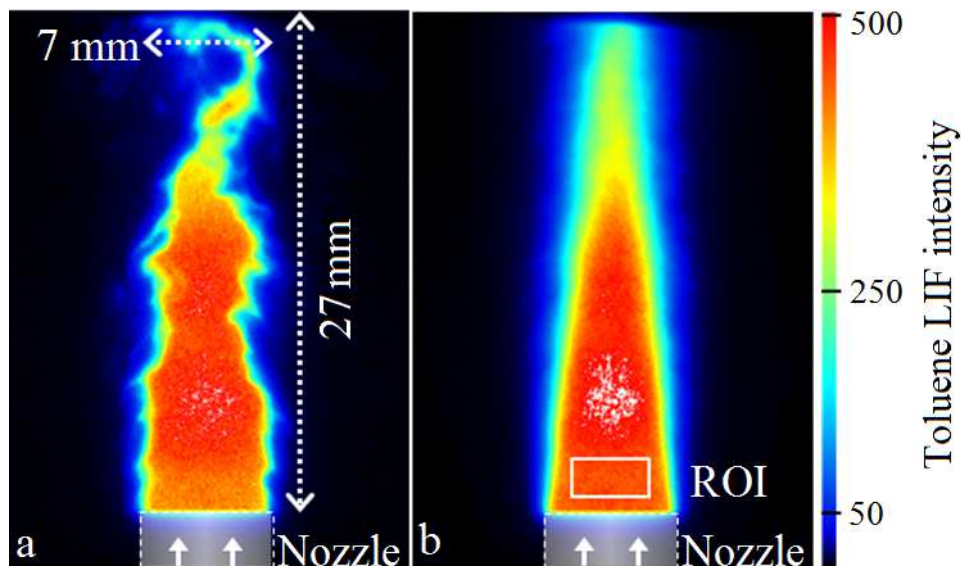


Figure 26: a) Example background-corrected single-shot LIF image; b) ensemble average over 100 images.

In the experiments, we sought to decouple the effects of saturation (i.e., non-linearity as a function of laser fluence) and self-quenching (i.e., non-linearity as a function of tracer concentration). Because both effects are coupled at combined high concentration and fluence, we performed measurements both at negligible toluene concentration and at near-zero laser fluence.

Figure 27 shows the signal dependence of toluene LIF on laser fluence for a tracer concentration for which we later show that self-quenching is negligible. For the conditions shown (303 K, N_2 , $n = 0.16$ vol%), the fitted curve according to Eq. (33) yields a saturation fluence of (192 ± 48) mJ/cm^2 (based on the sheet-mean fluence). Except when examining the fluence dependence of self-quenching, all further measurements were performed with “weak” excitation ($I_{laser} < 30$ mJ/cm^2), where the expected deviation of the signal from the linear case is less than 5%.

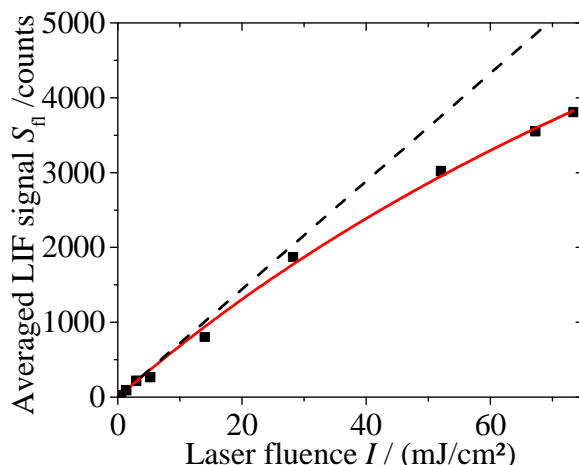


Figure 27: Toluene-LIF signal vs. laser fluence (carrier gas: N_2 , 303 K, $n = 0.16$ vol%). The solid red line is a fit according to Eq. (33) while the dashed line represents the expected trend without saturation.

5.2.2.2 Fluorescence lifetime measurement

A detailed description of the fluorescence lifetime experiment shown in Figure 28 can be found in [23]. A high-pressure pump (Bischoff, HPLC-pump 2250) metered the liquid tracer before it was evaporated and mixed with part of the main carrier gas N_2 in a commercial evaporator (Bronkhorst, CEM). The rest of the carrier gas was then admixed before the mixture entered a heatable high-pressure flow cell (flowing perpendicularly to the drawing plane in Figure 28). In the present experiments, the cell was operated at room temperature and atmospheric pressure.

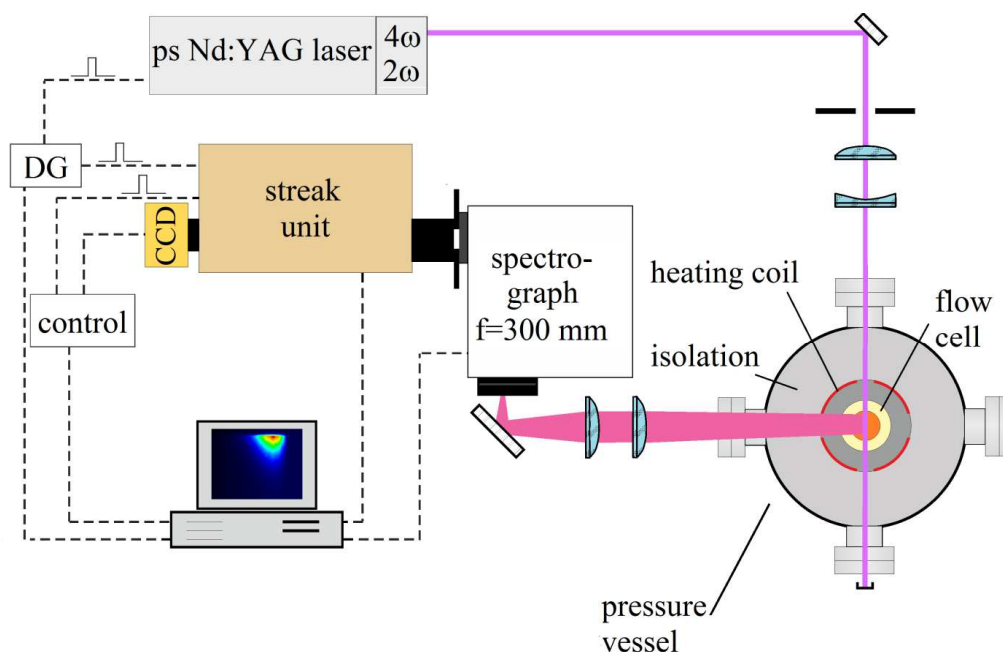


Figure 28: Schematics of the fluorescence lifetime experiment. DG: pulse/delay generator

For the LIF lifetime experiments, two optical arrangements were used. For picosecond excitation and direct detection of signal time traces, the unfocused beam of a frequency-quadrupled Nd:YAG laser (Ekspla, PL2143B, 266 nm, 26 ps, max. 1 mJ/pulse, 10 Hz) was directed through the center of the cell. The fluence in the probe volume was between 15 and 40 mJ/cm². By two quartz lenses,

the LIF signal was focused onto the entrance slit of a spectrograph (Acton, SP2300, $f = 300$ mm, 150 grooves/mm). The spectrally-resolved signal was imaged on the entrance slit of a streak camera (Hamamatsu C5680-24C), consisting of a streak module and a CCD camera (Orca R2) that provided temporal resolution depending on the setting of the streak module. For each condition, 1000 individual measurements were corrected for temporal jitter and background signal and then averaged.

For measurements with dramatically reduced (near zero) laser fluence, the output of a frequency-doubled Nd:YAG fiber laser (Fianium, UVP 266, 266 nm, 5 nJ/pulse, 30 ps, 20 MHz) was used and fluorescence lifetimes were determined from time-correlated single-photon counting (TCSPC) using a fast photomultiplier (Hamamatsu, R3809U50) and a TCSPC board (Becker and Hickl, SPC-130-EM) for data acquisition. A detailed description can be found in Ref. [33].

5.2.3 Results

5.2.3.1 Time-integrated LIF imaging

Figure 29 shows toluene LIF intensities measured with N_2 as bath gas as a function of toluene concentration (0.01–2.5 vol%) at $T = 303$ K and $p = 1$ bar. Here, the laser fluence was varied between 5 and 142 mJ/cm^2 . Together with results from the lifetime measurements described in Section 5.2.3.2, the data in Figure 29 can be used to check the applicability of the model introduced in Section 5.2.1.2, in particular as formulated in Eq. (34). In this equation, $\tilde{k}_q^{O_2} n_{O_2}$ was set to zero, since the LIF signal was collected from the oxygen-free part of the jet. As shown in section 5.2.3.2, self-quenching of toluene fluorescence vanishes for lower laser fluence, therefore, \tilde{k}_q^{tr} was also set to zero. The total rate of depopulation k_{tot} was fixed to the inverse value of the effective toluene-LIF lifetime under the experimental conditions, $\tau_{eff} = 46$ ns. The saturation fluence $I_{laser,sat}$ was also fixed to the previously determined value of 192 mJ/cm^2 . In order to fit the experimental data in Figure 29, we introduced a scaling factor G resulting in the following equation:

$$S_{fl} = G n_{tr} I_{laser,eff} \frac{k_{fl}}{k_{tot} + \tilde{k}_q^{tr*} I_{laser,eff} n_{tr}} \quad (41)$$

The scaling factor G and \tilde{k}_q^{tr*} were now optimized in least-squares fitting to the collective data points represented in Figure 29. This yields a self-quenching rate coefficient \tilde{k}_q^{tr*} of $(1.23 \pm 0.12) \times 10^5$ $cm^2/(s mJ vol\%)$, which, according to Eq. (38), corresponds to a Stern–Volmer coefficient k_{SV}^{tr*} of 0.11 $(vol\%)^{-1}$ at 22 mJ/cm^2 .

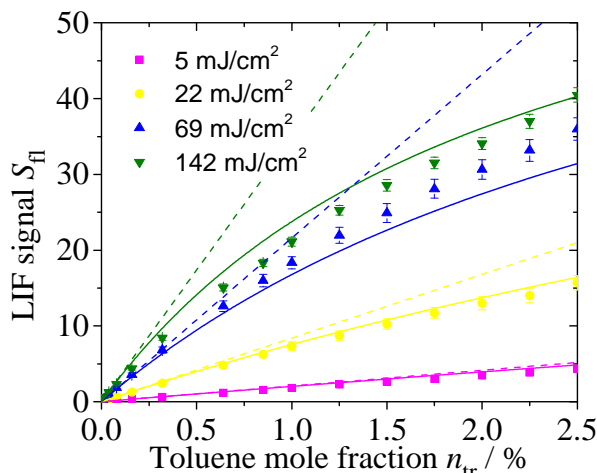


Figure 29: Toluene-LIF intensity as a function of toluene concentration (carrier gas: 1 bar N_2 at $T = 303$ K). The solid lines are fits including self-quenching and the dashed lines show the expected trend without self-quenching but including saturation. For details about the fit see text.

The relation expected in the *absence* of quenching can now be retrieved by setting the quenching term in Eq. (41) to zero. For each fluence, the expected linear relation (fluorescence intensity vs. tracer concentration) is represented by a dashed line in Figure 29. Note that for the two highest fluences the slope is no longer proportional to the laser fluence according to Figure 27 (“saturation”). The deviation of the measured data from linearity, however, is solely an effect of self-quenching, which already occurs at laser fluences that do not cause saturation. The combined effect is substantial, amounting to a maximum deviation from the linear expectation of a factor of two.

Figure 30 shows the result of experiments with various O_2 concentrations in the bath gas at a fixed total pressure of 1 bar at $T = 303$ K and $n_{tr} = 1.28$ vol%. The data were fitted again based on Eq. (39), but now including the self-quenching rate coefficient \tilde{k}_q^{tr*} fixed at the value determined above, and $\tilde{k}_q^{O_2}$ as a free parameter. This fit is shown as a solid red line.

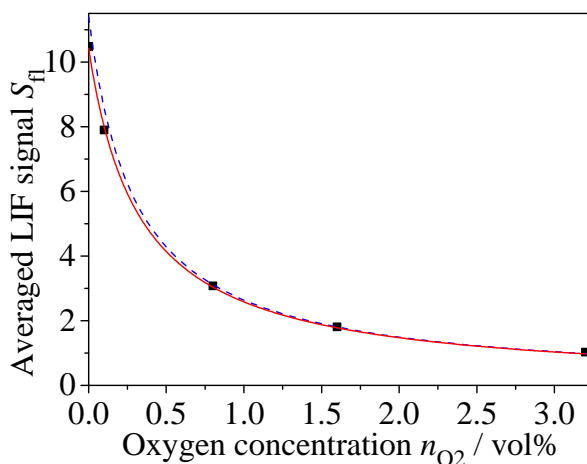


Figure 30: LIF signal vs. O_2 concentration for a toluene concentration of $n = 1.28$ vol% (carrier gas: N_2 /air mixture at $T = 303$ K, laser fluence: 22 mJ/cm²). The solid line is a fit according to Eq. (37), while the dashed line shows a simulation ignoring self-quenching.

The resulting Stern–Volmer coefficient for quenching by O_2 is $k_{SV}^{O_2} = (3.3 \pm 0.1) (\text{vol}\%)^{-1} = (330 \pm 10) \text{ bar}^{-1}$, which is consistent with values published in Ref. [20] ($k_{SV}^{O_2} = 340 \text{ bar}^{-1}$) and Ref. [17] ($k_{SV}^{O_2} = 402 \text{ bar}^{-1}$). Thus, quenching by O_2 is about a factor 50 more efficient than self-quenching, such that self-quenching becomes negligible in the presence of O_2 . We can simulate the signal expected in the absence of self-quenching by setting \tilde{k}_q^{tr*} to zero (dashed line).

Hence, in the presence of O_2 , the dependence of τ_{fl} on n is closer to linear up to higher tracer concentrations n_{tr} . Based on the constants determined above, Figure 31 shows the expected error that would result from neglecting self-quenching for a fluence of 25 mJ/cm^2 . In 5% O_2 , the error is still 5.5% for the higher laser energy. At all O_2 concentrations, the error can be expected to increase with increased laser fluence.

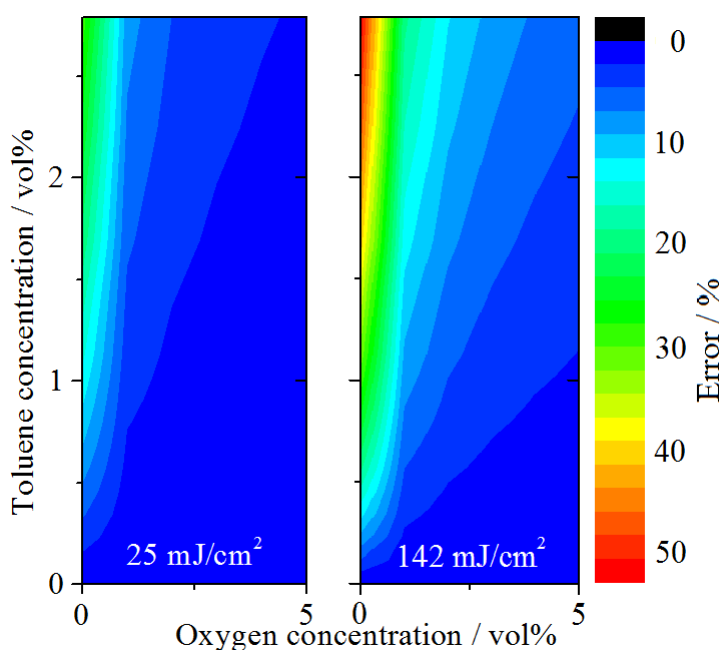


Figure 31: Error from neglecting self-quenching in toluene-LIF quantification for 300 K and a laser fluence of 25 mJ/cm^2 as a function of O_2 and toluene concentrations.

5.2.3.2 Fluorescence lifetime measurements

Figure 32 shows toluene-LIF lifetimes as a function of toluene concentration (0.12 to 2.8 vol%) and the corresponding Stern–Volmer plot from data measured in 1 bar N_2 at $T = 296 \text{ K}$ for various laser fluences. There is a significant decrease of the toluene-LIF lifetime with increasing toluene concentration at room temperature already at concentrations well below the vapor-pressure limit (2.85 vol%).

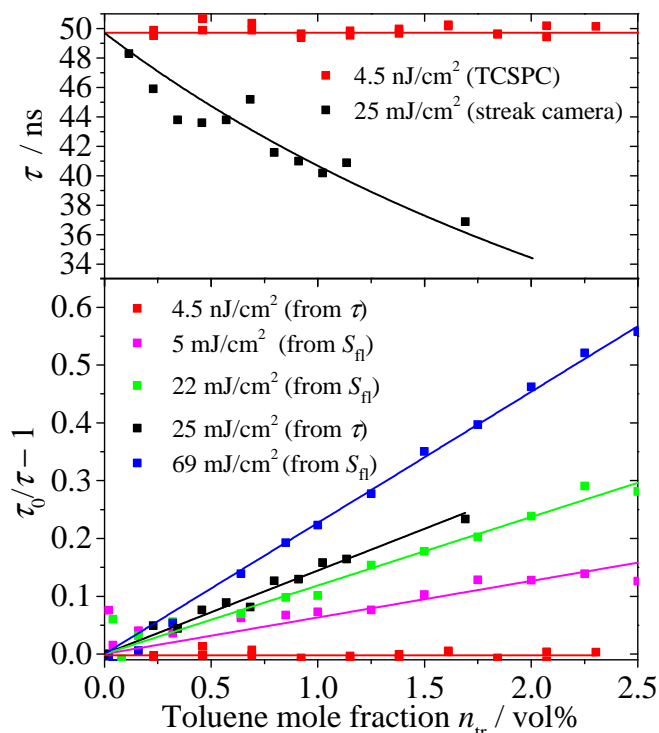


Figure 32: Top: Toluene-LIF lifetimes in 1 bar N₂ at 296 K as a function of toluene concentration determined from streak-camera and TCSPC measurements. Both data sets were fitted according to Eq. (42) sharing the same \tilde{k}_q^{tr*} . Bottom: Stern–Volmer plot for toluene self-quenching at 296 K for fluences up to 69 mJ/cm², both from lifetime measurements and time-integrated imaging. The deviations of the measured data from the fits for the lowest toluene concentration are due to the low signal-to-noise ratio at these low tracer concentrations.

Figure 32, bottom, shows that the slope in the Stern-Volmer plot (i.e., toluene self-quenching) systematically decreases with reduced laser fluence. To confirm this observation, fluorescence-lifetime measurements were carried out with near-zero laser fluence (~ 4.5 nJ/cm²). Under these conditions, the extremely weak signal can only be analyzed via time-correlated single-photon counting (TCSPC). Figure 32, top, shows that indeed the toluene-LIF lifetime becomes concentration-independent in this low-fluence range. This is also in agreement with earlier measurements with weak UV light from a lamp that did not show any influence of tracer concentration on the fluorescence quantum yield [17].

From the fluorescence-lifetime measurements, a self-quenching rate coefficient $\tilde{k}_q^{tr*} = (1.92 \pm 0.28) \times 10^5$ cm²/(s mJ vol%) can be determined by globally fitting the data at both 4.5 nJ/cm² and 25 mJ/cm² fluence according to

$$\tau = \frac{1}{\tau_{tot} + \tilde{k}_q^{tr*} I_{laser,eff} n_{tr}} \quad (42)$$

This value is qualitatively consistent with results from the time-integrated measurements, $(1.23 \pm 0.12) \times 10^5$ cm²/(s mJ vol%). The deviation outside the combined error limits could originate from uncertainty in the laser fluence for the lifetime measurements, since here the laser spot size was determined from burn patterns on photographic paper. This coarse method tends to overesti-

mate the spot size, leading to an overestimation for $\tilde{k}_q^{\text{tr}*}$. This possible additional systematic error is not covered in the estimated uncertainty for the self-quenching rate coefficient.

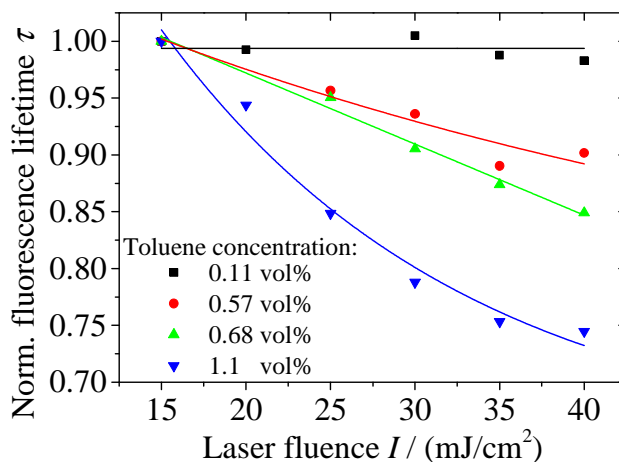


Figure 33: Toluene-LIF lifetimes in N_2 at 296 K (normalized with respect to the values at 15 mJ/cm^2) vs. laser fluence with exponential fits to guide the eye.

The effect of the laser fluence on the (normalized) fluorescence lifetimes is shown for selected toluene concentrations in Figure 33. The toluene-LIF lifetimes decrease with both increasing toluene concentration and increasing laser fluence. This again supports the conclusion that the effect of self-quenching depends on the laser fluence.

The complete absence of self-quenching in the low-fluence cases in this work strongly supports that quenching arises from collisions between two excited state molecules and ground-state toluene has a negligible quenching effect. Therefore, in case of toluene, \tilde{k}_q^{tr} can be ignored in Eq. (34) and the signal dependence on concentration and laser fluence can be described with the following equation:

$$S_{\text{fl}} \propto n_{\text{tr}} \frac{1}{1 + I_{\text{laser,sat}}/I_{\text{laser}}} \frac{k_{\text{fl}}}{\tau_{\text{tot}} + \tilde{k}_q^{\text{O}_2} n_{\text{O}_2} + \tilde{k}_q^{\text{tr}*} I_{\text{laser,eff}} n} \quad (43)$$

5.2.4 Conclusions

In this paper we demonstrated the effect of self-quenching on toluene LIF, which is significant at concentrations well below the limit given by the room-temperature vapor pressure, especially when measured with a bath gas that does not contribute to collisional quenching (such as N_2). These conditions have been used frequently in previous work when seeking strong signals to improve the signal-to-noise ratio in imaging experiments, calibration measurements, and for generating spectroscopic databases.

A tracer/carrier-gas mixture was investigated via LIF imaging in a free jet. With N_2 as bath gas, a significant deviation from a linear dependence of the LIF signal on the tracer concentration was observed already at concentrations 5–10 times below the room-temperature toluene vapor pressure due to self-quenching. Because the quenching cross-section of molecular oxygen is about 50 times

larger, toluene self-quenching is probably negligible for most measurement situations in air.

These effects were confirmed in fluorescence lifetime measurements, and both experiments yielded consistent self-quenching rate constants. It was shown that the self-quenching rate increases with laser fluence and becomes negligible at fluences near-zero, which is a strong indication that quenching occurs via collisions with electronically excited molecules and not with ground-state toluene.

The combined influence of laser fluence and tracer concentration on the signal intensity might have led to a misinterpretation of experimental observations in previous works. Deviations from linearity of signal vs. laser fluence that usually were interpreted as “saturation” might in reality have been caused by self-quenching phenomena. In cases where the toluene LIF signal was maximized by measuring toluene-LIF in nitrogen at high fluences, errors up to a factor of two may have occurred. Past spectroscopic measurements (e.g., those reporting the influence of temperature on fluorescence quantum yields) that were performed at elevated concentration and laser fluence should be revisited.

For quantitative imaging, the detrimental influence of the laser fluence on the measurement accuracy may limit the spatial resolution that can be achieved in the sheet-orthogonal dimension. To increase that resolution, the sheet thickness needs to be reduced, but for a given pulse energy this increases laser fluence and thus self-quenching needs to be considered to a greater extent.

Future work includes investigation of toluene self-quenching at elevated temperatures as well as revisiting other frequently used tracers. A thorough study is required to determine which published data (including those reporting fundamental spectroscopic data frequently used in the interpretation of tracer-LIF measurements) are affected by self-quenching. For instance, using the self-quenching rate coefficient determined here, a preliminary estimate shows that the results from Koban et al. [16] at room temperature are about 4% in error due to self-quenching. In that study an effective laser fluence of 3.12 mJ/cm^2 and maximum concentration of 2 vol% was used. Faust et al. [23] used an effective fluence of 29.6 mJ/cm^2 at 0.4 vol% toluene, leading to a self-quenching induced error of 7.3% at room temperature. Rossow used 3.92 mJ/cm^2 and a number density of 0.65 vol% [10], corresponding to an error of 1.5% at room temperature.

5.3 UV absorption and fluorescence properties of gas-phase *p*-difluorobenzene

The following chapter is based on the journal paper "UV absorption and fluorescence properties of gas-phase *p*-difluorobenzene", published in Applied Physics B 123 (1) 2017, 39–48 by Thorsten Benzler, Thomas Dreier, Christof Schulz.

Abstract

1,4-Difluorobenzene (*p*-DFB) is a promising aromatic tracer for determining concentration, temperature, and O₂ partial pressure in mixing gas flows based on laser-induced fluorescence (LIF). Signal quantification requires the knowledge of absorption and fluorescence properties as a function of environmental conditions. We report absorption and fluorescence spectra as well as fluorescence lifetimes of *p*-DFB in the temperature, pressure, and oxygen partial pressure range that is relevant for many applications including internal combustion engines. The UV absorption cross-section, investigated between 296 and 675 K, has a peak value close to 266 nm and decreases with temperature, while still exceeding other single-ring aromatics. Time-resolved fluorescence spectra were recorded after picosecond laser excitation at 266 nm as a function of temperature (296–1180 K), pressure (1–10 bar), and O₂ partial pressure (0–210 mbar) using a streak camera (temporal resolution 50 ps) coupled to a spectrometer. The fluorescence spectra red-shift (~2 nm/100 K) and broaden (increase in full width at half maximum by 58% in the investigated temperature range) with temperature. In N₂ as bath gas (1 bar), the fluorescence lifetime τ_{eff} decreases with temperature by a factor of about 20 (from 7 ns at 298 K down to 0.32 ns at 1180 K), while at 8 bar the shortest lifetime at 975 K is 0.4 ns. A noticeable pressure dependence (i.e., reduced τ_{eff}) is only visible at 675 K and above. Quenching of *p*-DFB LIF by O₂ (for partial pressures up to 210 mbar) shortens the fluorescence lifetime significantly at room temperature (by a factor of 8), but much less at higher temperatures (by a factor of 1.8 at 970 K). For fixed O₂ partial pressures (52 mbar and above), τ_{eff} shows a plateau region with temperature which shifts towards higher temperatures at the higher O₂ partial pressures. O₂ quenching is less prominent for *p*-DFB compared to other aromatic compounds investigated so far. The temperature dependence of O₂ quenching can be approximately expressed by an exponential function. The influence of temperature, total pressure, and O₂ partial pressure on absorption cross-sections and fluorescence quantum yields are given as empirical functions that allow for interpolation. For typical applications, *p*-DFB LIF provides up to three orders of magnitude stronger signal compared to toluene LIF.

5.3.1 Introduction

Single-ring aromatics are frequently employed as tracers in laser-induced fluorescence (LIF) imaging studies of gaseous systems for visualizing concentration, temperature, oxygen concentration, or fuel/air equivalence ratio [4]. The tracers are added to the respective UV-transparent base fuel (or bath gas) in concentrations low enough to provide sufficient LIF signal and still represent the

physical behavior of the base gas composition. The fluorescence signal intensity depends on the tracer concentration, the absorption cross section and the fluorescence quantum yield ϕ_{fl} . Because the latter two strongly depend on temperature, pressure, and bath-gas composition, quantitative interpretation of signal intensities requires the knowledge of these dependences.

Toluene is one of the best studied fluorescence tracers and widely used for applications [17, 19, 27, 29, 34]. Its fluorescence strongly decreases with increasing temperature and O₂ partial pressure which leads to a challenge for detecting signal under the respective conditions with high enough signal-to-noise ratio, especially in cases where methods are used that determine the desired quantity (such as temperature [16, 22] or O₂ partial pressure [20, 23]) from the ratio of two measured intensities. This study will show that para-difluorobenzene (*p*-DFB) can provide significantly stronger signal already at room temperature and shows a significantly reduced response to temperature and oxygen quenching leading to a gain in signal intensity compared to toluene by two to three orders of magnitude. Due to its thermophysical properties (boiling point: 88°C, viscosity: 0.6390 Ns/m² at 298 K, vapor pressure 72 mbar at room temperature) *p*-DFB is ideally suited as tracer for gasoline [57] or as representative for the light fraction of multi-component fuels [44].

Investigations of the photo physical properties of the S₀ → S₁ (π , π^*) transition of gas-phase *p*-DFB are scarce. Since different absorption bands are located between 246 and 273 nm (with a peak at 266 and 271 nm) [94] *p*-DFB can be excited conveniently with 266 nm radiation from a frequency-quadrupled Nd:YAG laser. Fluorescence spectra cover the 260–350 nm range. The high fluorescence quantum yield of 0.43 (for 266 nm excitation in N₂ at room temperature) as well as the large absorption cross-section in the range of 1.2×10⁻¹⁷ to 0.4×10⁻¹⁷ cm² make *p*-DFB attractive as fluorescence tracer for LIF imaging diagnostics.

Because of its promising properties, there is a strong need for further characterization of the photo-physical behavior of *p*-DFB. Such data can also contribute to a better understanding of energy redistribution and relaxation processes in *p*-DFB.

Therefore, we have investigated absorption cross-sections and fluorescence spectra as a function of temperature, and effective fluorescence lifetimes τ_{eff} of *p*-DFB are evaluated at various temperatures in N₂ and air as bath gas at various total pressures. Relative fluorescence quantum yields, i.e., normalized to a reference condition, can be quantified through τ_{eff} measured after short-pulse excitation to its first excited electronic state [65]. In the present work we analyze the dependence of *p*-DFB absorption cross-sections, fluorescence spectra, fluorescence lifetimes and quantum yields in the 298–1180 K temperature range with excitation at 266 nm. Measurements are carried out in pure N₂ and in air at total pressures between 1 and 10 bar. In addition, we present functional relationships for calculating the signal intensity per molecule in dependence of temperature, total pressure, and O₂ partial pressure for 266 nm excitation.

For application of fluorescence tracers at high temperature, it is also of interest to study the thermal stability limits. This can be of specific interest for fluorinated tracers because the decomposition can lead to the formation of strongly corrosive hydrofluoric acid.

5.3.2 Theoretical background

At room temperature, 266 nm excitation of the single-ring aromatic *p*-DFB species can populate the S_1 state, which generally is followed by very fast non-radiative vibrational relaxation (VR), internal conversion (IC) to S_0 and intersystem crossing (ISC) to a triplet state, 7800 cm^{-1} lower in energy [95] than the S_1 zero-point energy. The simplified rate equation [4, 65]

$$-\frac{d}{dt} [M^*] = (k_{\text{fl}} + k_{\text{ISC}} + k_{\text{IC}}) [M^*] \quad (11)$$

describes the intramolecular deactivation of the excited molecules M^* . Here k_{fl} , k_{ISC} , k_{IC} are the rates (all in s^{-1}) of fluorescence emission, intersystem crossing, and internal conversion, respectively.

Since O_2 is known as a highly-efficient fluorescence quencher for aromatic molecules due to its triplet structure in the ground state [4], a Stern-Volmer relation

$$\frac{S_{\text{fl}}^0}{S_{\text{fl}}} = \frac{\tau_{\text{eff}}^0}{\tau_{\text{eff}}} = 1 + k_{\text{SV}} n_{\text{q}} \quad (17)$$

can be used [20, 51, 52], i.e., a linear dependence of the ratio of signal intensity S_{fl} (and thus fluorescence lifetime τ_{eff}) without (index 0) and in presence of the quencher with number density n_{q} .

Generally, the relation between τ_{eff} and the fluorescence quantum yield ϕ_{fl} is given by

$$\phi_{\text{fl}} = \frac{k_{\text{fl}}}{k_{\text{fl}} + k_{\text{ISC}} + k_{\text{IC}} + \sum k_{q,j} n_{q,j}} = \frac{k_{\text{fl}}}{k_{\text{tot}}} = \frac{\tau_{\text{eff}}}{\tau_{\text{fl}}} = \text{const.} \times \tau_{\text{eff}}, \quad (16)$$

with τ_{fl} , the natural lifetime [65]. Thus, the fluorescence quantum yield is proportional to τ_{eff} . Measuring the fluorescence decay after picosecond laser excitation therefore provides a more direct access for measuring (relative) ϕ_{fl} [4, 22] and to the energy conversion processes taking place in the electronically excited state than do intensity-based measurements because it is independent on absolute intensity calibration, which needs careful control of instrumental parameters (e.g., laser intensity and tracer concentration).

5.3.3 Experiment

1,4-Difluorobenzene (Merck Chemicals, for analysis grade) was used as a pure substance without further purification and stored in a glass container pressurized with N_2 . N_2 (purity >5.0) and air were provided from vaporized liquid N_2 and compressed air for pressures up to 6 bar. N_2 and air for higher pressures were provided from gas cylinders (Air Liquide, purity 5.0). For gas mixtures with well-controlled composition, *p*-DFB was metered by a high-pressure pump (Bischoff-Chrom, HPLC Compact Pump 2250) and injected into a heated chamber (Bronkhorst, CEM) where it was evaporated and mixed with a part of the carrier gas. Variable O_2 partial pressures were provided via mass flow controllers (Bronkhorst) metering the flows of N_2 and air and a small gas mixing chamber. *p*-DFB partial pressures p_{DFB} were 3 to 12 mbar, well below the room-temperature vapor pressure of 72 mbar. To prevent condensation, all tubes were resistively heated to 470 K.

5.3.3.1 Absorption experiment

A stainless steel high-temperature absorption flow cell (flow rate 2 slm) with an absorption length of 110 mm [96] was placed in an oven and used at atmospheric pressure. The temperature was monitored by a thermocouple placed close to the measurement volume.

Absorption spectra were measured against a broadband UV light source (LOT Oriel deuterium lamp) collimated with a quartz lens. A beam splitter was placed in front of the cell entrance window. This reference signal as well as the transmitted light was coupled into a y-fiber connected to a spectrometer (Horiba, iHR20, $f = 320$ mm, 1200 groves/mm grating) and detected simultaneously by a CCD camera (Horiba, Syncerity CCD, 256×1024 pixels). An exposure time of 1 ms and an entrance slit width of $200 \mu\text{m}$ were used to adjust to the 16 bit dynamic range of the camera with a spectral resolution of 0.47 nm FWHM . Spectra were then generated by binning over 50 pixels for both the transmitted light and the reference. The p -DFB partial pressure was varied ($p_{\text{DFB}} = 0.1$ – 1 mbar) for each temperature to ensure that the measurements took place in the linear absorption regime and to average over various experimental conditions.

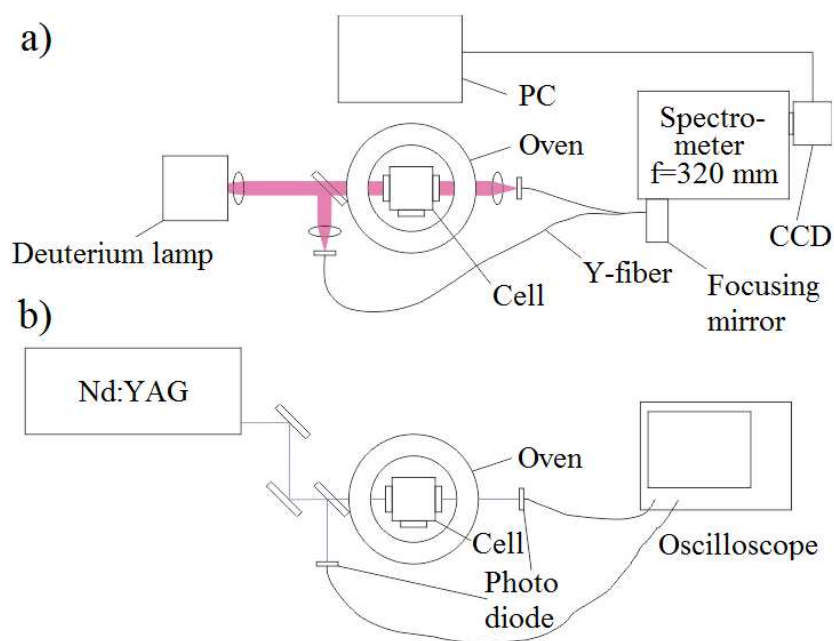


Figure 34: Experimental arrangement for absorption cross-section measurements with a) a deuterium lamp and b) a Nd:YAG laser.

The absorption spectra are structured at low and intermediate temperature. To ensure that the absorption cross-sections relevant for laser experiments with excitation at 266 nm are not affected by under-resolved spectral detection, additional absorption measurements were carried out with light from a Nd:YAG laser system (BM industries, Series 5000, 5 ns pulse duration). Reference and transmission signals were detected by photo diodes (Thorlabs, DET10A) and read out by an oscilloscope (Teledyne LeCroy, Wavesurfer 3034). Both arrangements are shown in Figure 34.

5.3.3.2 Fluorescence experiment

Spectrally- and temporally-resolved fluorescence measurements were carried out with an arrangement described in Ref. [22], therefore, only a brief overview is given here. A mixture of evaporated *p*-DFB and the respective bath gas was flowing continuously from top to bottom through a cylindrical ceramic flow chamber (inner diameter 45 mm, length 250 mm) with four holes on its circumference for optical access (Figure 35). This assembly is contained in a 400-mm-diameter stainless-steel pressure vessel where the incoming and outgoing gas flows through two concentric tubes connected with the flow chamber from the bottom of the vessel. Heating elements placed around the flow chamber and thermally insulated against the outer vessel walls by ceramic foam elements allow heating of the gas flow up to 1400 K at a maximum gas pressure of 10 bar, while keeping the pressure vessel and its window flanges below 370 K. Gas temperature and pressure in the flow chamber were measured with a R-type thermocouple located close to the measurement volume and a pressure transducer, respectively. Constant pressure was achieved by a back-pressure regulator in the exhaust line of the flow system. The residence time of the gases in the heated zone of the cell is ~ 2 s.

The quadrupled output of a ps-Nd:YAG laser (Ekspla, PL2143B, 266 nm, pulse duration: 26 ps) was collimated to a 3 mm diameter beam and directed horizontally through the center of the cell. The fluorescence was collected perpendicular and focused on the 150 μm entrance slit of a spectrometer (Acton SP2300, $f = 300$ mm, 150 grooves/mm grating, spectral resolution: 1.92 nm). The spectrally-dispersed light was imaged on the entrance slit of a streak camera (Hamamatsu, C5680-24C, temporal resolution: 50 ps). The system thus simultaneously delivers fluorescence spectra (binning of rows in the time domain) and fluorescence decay profiles (binning of columns in the spectral domain).

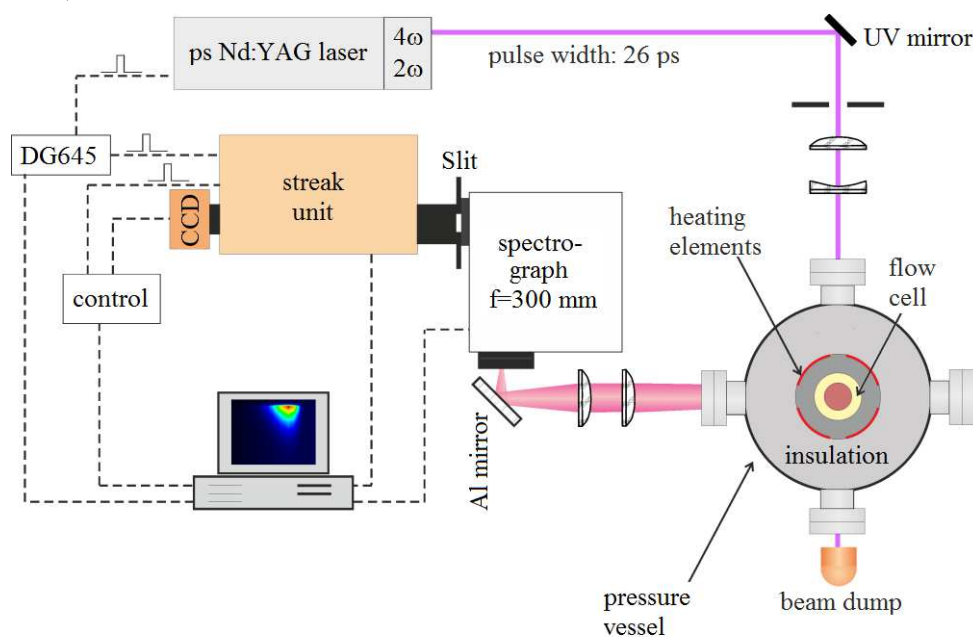


Figure 35: Experimental arrangement for spectrally- and temporally-resolved LIF measurements, CCD: CCD camera, DG: pulse delay generator.

The fluorescence intensity was investigated as a function of laser fluence to determine the limits of the linear regime (not shown here) which was approached at around 15 mJ/cm^2 at 296 K. This value was utilized for temperatures up to 900 K. Because the saturation limit is known to shift to higher fluences at elevated temperatures [97], the laser fluence was increased to 25 mJ/cm^2 at $>900 \text{ K}$ to maintain an acceptable signal-to-noise ratio. p_{DFB} was 3 mbar at the lowest temperature (296 K) and was correspondingly increased at higher temperatures to maintain nearly constant tracer number densities in the probe volume. In additional measurements it was tested that at this number density self-quenching [98] can be neglected.

5.3.4 Data Evaluation

5.3.4.1 Absorption experiments

For each measurement of absorption spectra, 200 images were averaged to minimize noise. Measurements were taken with and without p -DFB in the cell for otherwise identical conditions and the absorption was determined from the difference between both. The result was corrected for potential variations in intensity and lamp spectra using the reference measurement from the beam splitter. The absorption cross-section was then calculated using Beer-Lambert's law

$$\sigma_{\text{abs}} = \ln(I_0/I)/d n, \quad (44)$$

with I_0 and I as intensity without and with p -DFB, respectively, d as the distance between the quartz windows (110 mm) and n the tracer number density.

For the laser absorption measurements 1000 pulses were averaged. Afterwards, the same calculation with Lambert-Beer's law has been done for the laser with peak-to-peak measured signals to subtract the background.

5.3.4.2 Fluorescence experiments

For each condition, 1000 individual single-shot measurements were acquired and stored. The respective images were then averaged after adjusting the time axis with a jitter-correction routine provided by the streak camera software to minimize smearing of the temporal profiles. A background image was subtracted that was obtained while the laser was firing with N_2 flowing through the cell only. Figure 36 shows a sample image with wavelength along the horizontal and time along the vertical axis. In the CCD image, columns or rows can be binned to generate temporal or spectral profiles of the recorded fluorescence signals, respectively. It was found that within the error limits the number of binned columns did not influence the evaluated effective fluorescence lifetimes, i.e., there was no significant dependence of the lifetime with emission wavelength. Thus for SNR enhancement, the signal between 265 and 350 nm was integrated when determining fluorescence decay curves.

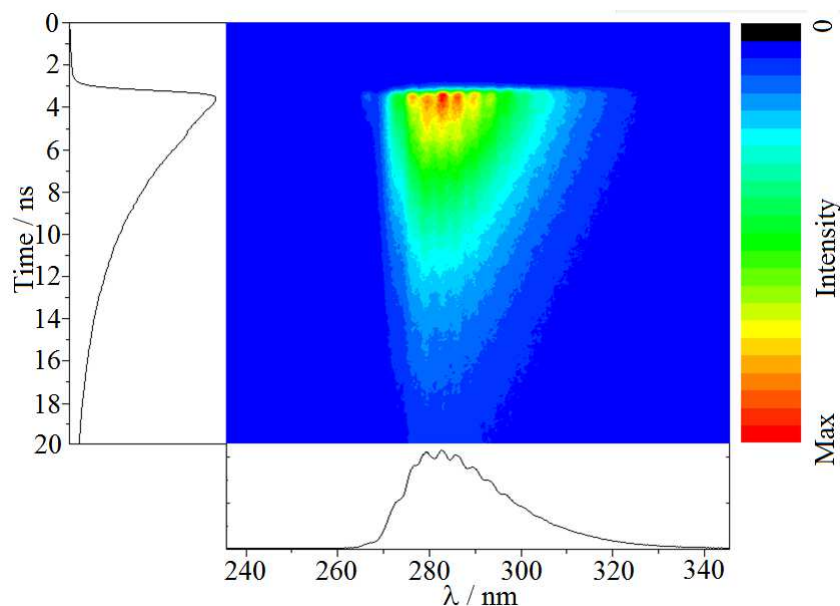


Figure 36: Sample image (averaged over 1000 single-shot images) of time- and spectrally-resolved *p*-DFB LIF after 266 nm excitation. Conditions: 325 K, 1 bar total pressure of N_2 , $p_{DFB} = 3$ mbar.

Fluorescence spectra were generated by binning all rows with significant pixel counts. The resulting spectra were corrected for the instrument spectral response by recording the spectrum from a deuterium lamp with known spectral irradiance using the same optical setup. Figure 37 presents typical LIF excitation/decay profiles for 298, 475, and 675 K together with the instrument response function determined from stray light in the empty cell. Here the streak camera was set to 20 ns sweep duration. Because the fluorescence lifetimes vary depending on the environmental conditions, the temporal resolution (i.e., the sweep duration) was adjusted, requiring separate instrument functions to be recorded.

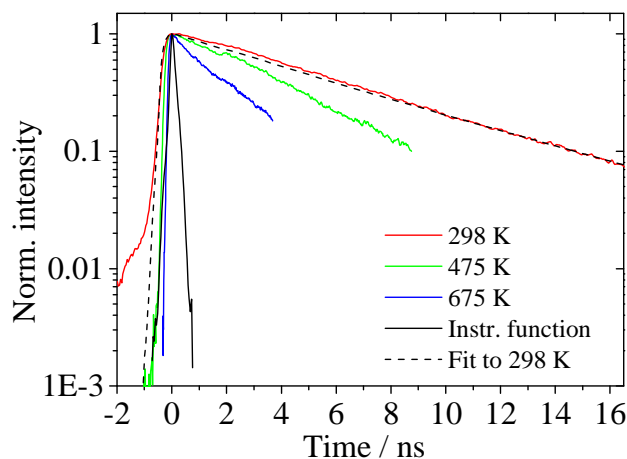


Figure 37: Time-resolved *p*-DFB LIF intensity in 1 bar N_2 with excitation at 266 nm at various temperatures. For 298 K, the fitted function (with $\tau = 6.6$ ns) is shown as dotted curve. The instrument response curve (magenta line) was recorded based on 266 nm stray light. Sweep duration 20 ns.

Signal decay times τ were determined using the convolve-and-compare method described by Settersten et al. [99, 100]. A convolution of a single- or double-exponential decay with the measured instrument-response function was fitted to the experimental excitation/decay profiles by min-

imizing the sum of squared residuals between both curves. Figure 37 shows an example of such a convoluted signal profile (black dotted line in Figure 37) fitted to the 298 K LIF signal trace (red) and the respective instrument function (black). In the fits the variable parameters were the decay time τ and a shift of the time axis to optimize the instance where experimental and simulated signal intensities reach their respective peak values. For the fastest measured decays, the minimum temporal resolution of the detection system was 50 ps.

5.3.5 Results

Absorption measurements were performed for temperatures between 296 and 675 K in 1 bar N₂ as bath gas. Fluorescence measurements were done at 296–1175 K and at 1–10 bar in N₂. At higher temperatures, no fluorescence was detectable apart from a significant increase in laser stray light, most probably due to pyrolysis during the ~ 2 s residence time in the heated cell. When O₂ was present, possible tracer degradation/oxidation limited the upper temperature to 975 K. At higher temperatures, again, strong stray light was detected, together with a small increase in gas temperature. Compared to other tracers investigated by us so far (e.g., toluene, naphthalene, anisole) *p*-DFB showed the strongest resistance to oxidation (i.e., the highest limiting temperature within the residence time of ~ 2 s in our cell).

5.3.5.1 Absorption cross-section

Figure 38 (left panel) shows the absorption spectra of *p*-DFB for various temperatures. The spectra show a characteristic band structure that is most prominent at the lower temperatures but persists up to the highest temperatures investigated here. The center of gravity of the spectra red-shifts with increasing temperature. The peak absorption was close to 266 nm and the individual peaks show a minor red-shift only. The right panel in Figure 38 shows the data for 266 nm from the lamp measurements compared to laser-based absorption measurements. The absorption cross-sections decrease with increasing temperature as the band structure vanishes. Although the spectral resolution of the lamp measurement is quite good (0.47 nm FWHM, cf. arrows in Figure 38 as determined by the FWHM of a recorded mercury line at 254 nm from a low-pressure discharge lamp), the spectra are still under-resolved for low temperatures, leading to an increased deviation between the lamp and laser measurements towards lower temperatures in the right panel in Figure 38. The room-temperature values of the laser measurement are reassured by results from Volk et al. [43]. At < 450 K, the fine structure is almost lost and the lamp and laser measurements approach each other.

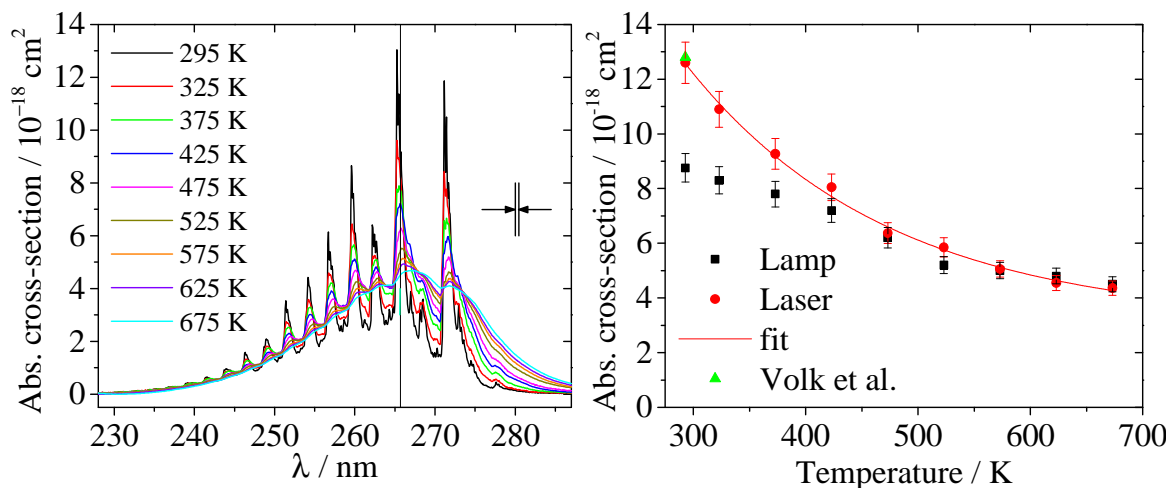


Figure 38: Absorption spectra of p -DFB at various temperatures in 1 bar N_2 (left panel). The arrows indicate the spectral resolution. Right panel: Absorption cross sections at 266 nm determined from the spectra (black squares) and the laser measurements (red dots) with fit. The fit is based on the function given in Table 8. Room-temperature literature value from Volk et al. [43].

5.3.5.2 Fluorescence spectra

The left panel in Figure 39 shows the temperature dependence of p -DFB fluorescence spectra in 1 bar N_2 normalized to their respective peak intensities. The spectra were smoothed by an adjacent-average filter with a window size of 1.5 nm. At room temperature, the emission extends from roughly 265 to 340 nm with a maximum at around 280 nm. With increasing temperature, a slight red-shift of this maximum ($\sim 2 \text{ nm}/100 \text{ K}$) can be observed, and the tail on the long-wavelength side of the spectra becomes stronger relative to the peak. Due to the limited spectral resolution of the present experiment of about 1.9 nm (FWHM, indicated by the arrows in Figure 39, determined from the FWHM of a recorded mercury line at 254 nm from a low-pressure discharge lamp) the band structure at low temperatures may be under-resolved. The observed spectral shape does not change with increasing total pressure. When adding increasing amounts of O_2 , a weak red-shift as well as a relative intensity change of the different peaks can be observed (Figure 39, right).

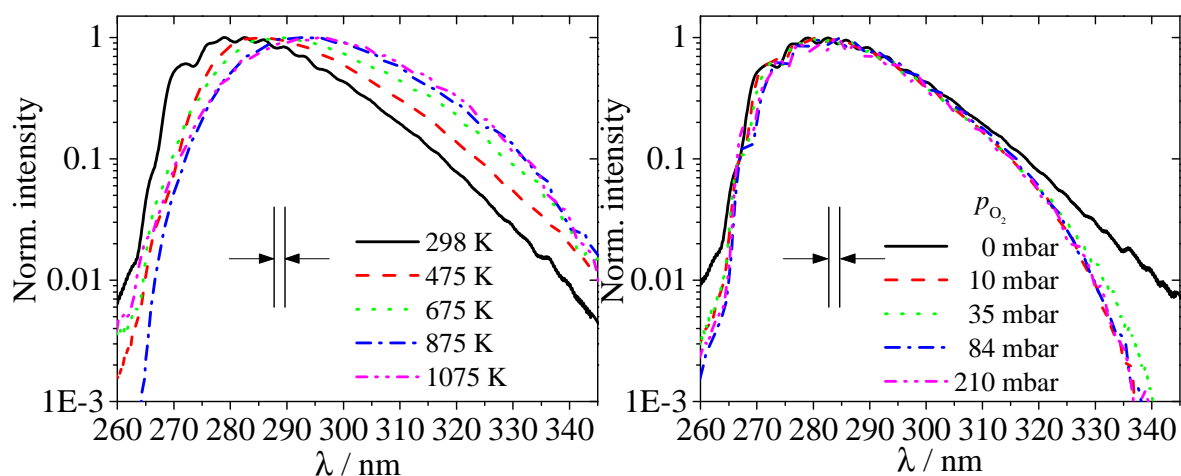


Figure 39: Left: Peak-normalized p -DFB fluorescence spectra at various temperatures in 1 bar N_2 bath. Right: Spectra at different O_2 partial pressures at 298 K and 1 bar total pressure. $p_{\text{DFB}} = 3 \text{ mbar}$. The arrows indicate the spectral resolution of the detection system (1.92 nm FWHM).

5.3.5.3 Effective fluorescence lifetimes

Nitrogen atmosphere

The present work complements data from our previous works on the temperature, O₂, and bath-gas pressure dependences on effective fluorescence lifetimes of toluene and naphthalene [23] and anisole [41]. Evaluated fluorescence lifetimes for *p*-DFB in N₂ are shown in Figure 40 as a function of temperature for a total pressure of 1 and 8 bar. For both pressures and lower temperatures, the lifetimes are almost equal within the experimental uncertainty and linearly decrease with temperature on a logarithmic scale up to a certain temperature before they continue to decrease more strongly with a different slope. This change in slope takes place at ~700 K at 1 bar and at ~580 K at 8 bar. The stronger slope at 8 bar (38% reduction in τ per 100 K) is about 26% larger than the slope at 1 bar (31% reduction in τ per 100 K) and both are larger than the common slope (17% reduction in τ per 100 K) in the lower temperature range (298–580 K). Exponential fits are shown as solid lines in Figure 40 for both pressures.

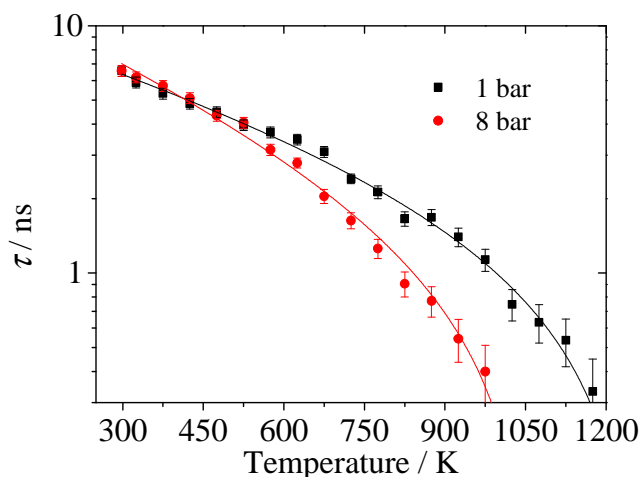


Figure 40: Effective fluorescence lifetimes of *p*-DFB in N₂ as a function of temperature for 1 and 8 bar together with the temperature fit for the subsequent pressures found in Table 8.

Figure 41 shows effective fluorescence lifetimes of *p*-DFB in N₂ as a function of total pressure and for 298–875 K. As already noticed in Figure 40, for the two lower temperatures of 298 and 475 K, the fluorescence lifetimes are almost independent of the gas pressure within the experimental uncertainty while for the higher temperatures a decrease with pressure in the lower-pressure region is noticeable, which flattens out into a plateau region up to the highest pressures investigated. As temperature rises the onset of the plateau region seems to start at increasingly higher pressures.

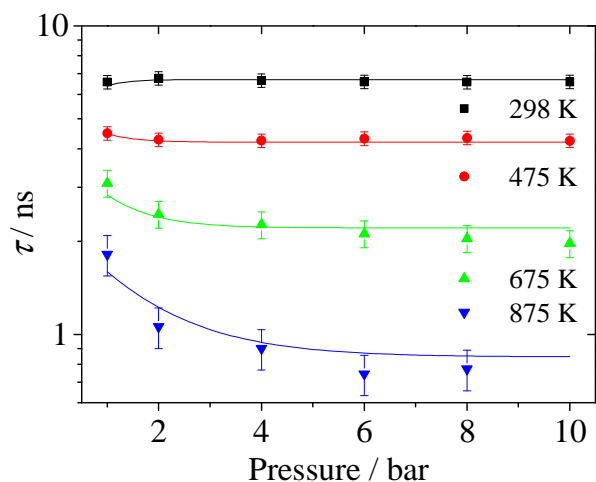


Figure 41: Effective fluorescence lifetimes of *p*-DFB as a function of N₂ pressure at various temperatures together with the pressure fit for the subsequent temperatures found in Table 8.

Oxygen quenching

It is known that O₂ with its triplet ground state is an efficient fluorescence quencher in aromatic species due to very fast collision-induced singlet–triplet energy transfer. Therefore, it is expected that (i) the *p*-DFB fluorescence lifetime strongly depends on p_{O_2} , and (ii) the presence of O₂ affects the temperature- and pressure dependence of ϕ_{fl} relative to measurements in a N₂ atmosphere. For constant temperature, increasing p_{O_2} causes a decrease in τ_{eff} . However, as can be seen in Figure 42, the reduction is most prominent at room temperature (factor of 8.3 between 0 and 210 mbar p_{O_2}) and diminishes at higher temperatures. Depending on p_{O_2} , τ_{eff} exhibit a shallow maximum with increasing temperature, which shifts towards higher temperatures at higher p_{O_2} , as also seen with other aromatic tracers [23, 41].

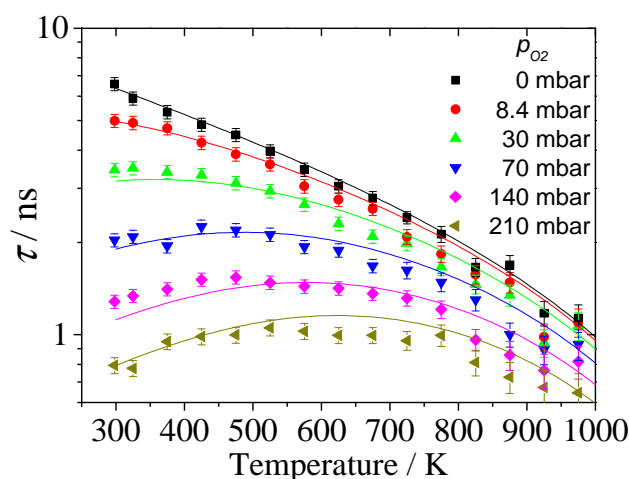


Figure 42: Effective fluorescence lifetimes of *p*-DFB as a function of temperature for several O₂ partial pressures.

The fluorescence lifetimes at >800 K might be less trustworthy since oxidation might already take place on the timescale of our experiment. However, *p*-DFB showed no noticeable degradation due to pyrolysis or oxidation within the residence times (~2 s) in the heated zone of the flow system

and at the highest temperatures investigated here, as can be deduced from the appearance of the fluorescence spectra presented earlier. In N_2 , p -DFB is thermally as stable as naphthalene and in air it exceeds the stability of naphthalene that has been investigated before in the same flow cell [41].

Stern-Volmer coefficients

The quenching behavior of the fluorescence of aromatic species by O_2 can often be expressed by the Stern-Volmer coefficient (Eq. 17). If temporally- and spectrally-integrated fluorescence intensities show Stern-Volmer behavior, this should apply as well to measured fluorescence lifetimes. To validate this, Stern-Volmer coefficients for p -DFB were determined from the slopes of fluorescence lifetime data plotted for a given total pressure (with N_2) and temperature vs. p_{O_2} (Figure 43, left). The resulting Stern-Volmer coefficients are plotted as a function of temperature in the right panel of Figure 43. In comparison to anisole [41] and toluene [23], O_2 quenching of p -DFB is comparably weak.

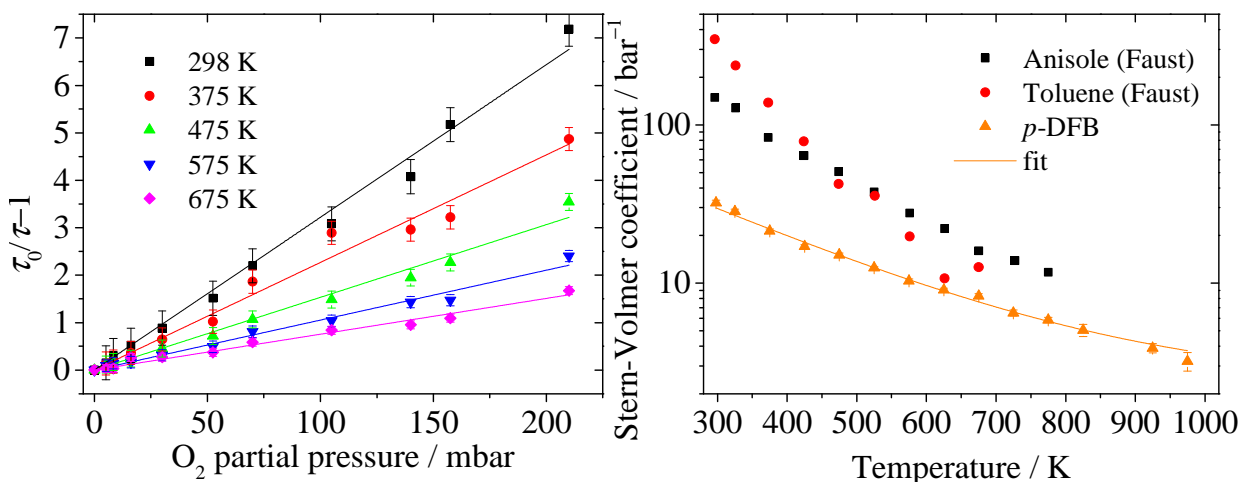


Figure 43: Left: Stern-Volmer plots of p -DFB effective fluorescence lifetimes for various temperatures. Right: Stern-Volmer coefficients for toluene [23], anisole [41], and p -DFB as a function of temperature together with a fit function for p -DFB given in Table 8.

5.3.5.4 LIF intensity model

In the previous sections, the dependences of the absorption cross-section and the fluorescence quantum yield of p -DFB on the environmental conditions have been described. To enable the application of these data to other experiments, the dependences need to be combined and then, the results can be compared to measurements in more applied cases, like, e.g., in Faust et al. [41]. With exponential fits to the temperature dependent absorption cross-section (Figure 38, right panel) and the temperature- (Figure 40 [101]), pressure- (Figure 41), and O_2 partial pressure- (in form of the Stern-Volmer coefficients Figure 43, right) dependent fluorescence lifetime it is possible to predict fluorescence intensities per unit number density or volume in a given situation. The respective fit functions are given in Table 8.

Table 8: Empirical functions to predict p -DFB LIF intensities for variable temperature, pressure, and O_2 partial pressure conditions. Temperatures are in Kelvin and pressures in bar. p_{tot} is the total pressure and p_{O_2} the O_2 partial pressure.

Absorption cross-section	$\sigma_{\text{abs}}(266 \text{ nm}, T) = 3.13 \times 10^{-18} + 4.81 \times 10^{-17} \exp\left(-\frac{T}{179.9}\right)$
Oxygen quenching	$\phi_{\text{fl}}(266 \text{ nm}, T, p_{O_2}) = \left(1.32 + 87.94 \times \exp\left(-\frac{T}{256.67}\right)\right) p_{O_2}$
LIF lifetime at 1 bar	$\tau(266 \text{ nm}, T, p_{O_2}) = \frac{-2.2074 + 13.067 \exp\left(-\frac{T}{708.8}\right)}{\phi_{\text{fl}}(266 \text{ nm}, T, p_{O_2})}$
Temperature and pressure dependence	$\begin{aligned} \tau(266 \text{ nm}, T, p_{\text{tot}}, p_{O_2}) &= (3.83 \times 10^{-7} \times T^2 + 3.63 \times 10^{-4} \times T - 0,201) \\ &\times \exp\left(-\tau(266 \text{ nm}, T, p_{O_2}) \times \frac{p_{\text{tot}}}{2.34157}\right) \\ &+ (-1.85838 + 15,4845 \exp\left(-\frac{T}{505,07}\right)) \end{aligned}$

The signal intensity per molecule can then be calculated by:

$$S \sim \sigma_{\text{abs}}(\lambda, T) \times \phi_{\text{fl}}(\lambda, T, p_{\text{tot}}, p_{O_2}) \sim \sigma_{\text{abs}}(266 \text{ nm}, T) \times \frac{k_{\text{fl}} \times \tau(266 \text{ nm}, T, p_{\text{tot}}, p_{O_2})}{1 + \phi_{\text{fl}}(266 \text{ nm}, T, p_{O_2})} \quad (45)$$

This formula is the result of a simplification of a rate-constant approach to determining the fluorescence quantum yield, ϕ_{fl} (similar to the strategy used by Koban et al. for toluene in Ref. [20]) multiplied by the absorption cross-section. Multiplying the result with the number density and the total pressure yields the estimated signal per volume.

A comparison for expected p -DFB and toluene signal are shown in the left panel in Figure 44 per molecule (i.e., unit number density) and in the right panel per volume. The toluene data is from the extended Koban model together with measured absorption cross-sections [16, 23, 57] (note the error in the model description in Ref. pressure [23] on page 90 where the T^4 term in the description of B_3 has the wrong sign). This comparison illustrates the signal improvement by 2 to 3 orders of magnitude gained by p -DFB in comparison to toluene depending on the environmental conditions.

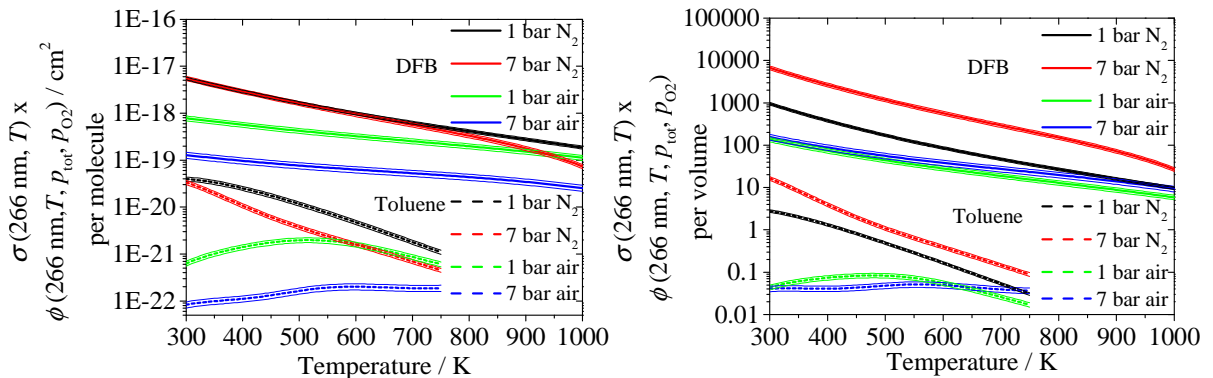


Figure 44: Temperature-dependent LIF-signal intensities for various bath-gas conditions of p -DFB and toluene per molecule (left panel) and per volume with the number density corresponding to 10% of the vapor pressure at 298 K (right panel). Toluene data from extended Koban model that is validated up to 750 K [16, 23, 57].

5.3.6 Discussion

The data presented in section 5.3.5 indicate high signal intensities for *p*-DFB for a wide range of environmental conditions. The structure of the absorption spectra matches the one reported by Volk et al. [43] for room temperature. However, the gas pressure in their experiment was close to vacuum (0.066 mbar air) which explains the broader band structure that we showed in Figure 38 as well as the difference in lamp and laser measurements. The value at 266 nm from the laser measurements of $1.26 \times 10^{-17} \text{ cm}^2$ at room temperature also matches the one determined by Volk of $1.28 \times 10^{-17} \text{ cm}^2$.

The decrease in fluorescence lifetime of *p*-DFB (Figure 41) with increasing pressure fits into the explanation we gave for the pressure dependence based on low-pressure experiments for various tracer species [102]. We showed there, that the pressure dependence slowly changes from increasing the fluorescence lifetime to decreasing it with increasing temperature. This is due to the change in the Boltzmann distribution in the S_0 and S_1 state and whether the first populated state after excitation is above or below the thermal energy level in the S_1 state. This is further emphasized by the fact that in *p*-DFB the 0–0 band gap is $\sim 760 \text{ cm}^{-1}$ smaller than 266 nm excitation [101]. This is very close to the difference in the population-weighted thermal energy of the Boltzmann distribution in the S_0 and S_1 vibrational manifolds for this temperature in similar molecules; therefore, no vibrational relaxation and therefore no pressure dependence of the fluorescence quantum yield is to be expected for low temperatures, which is confirmed by the data in Figure 41. At higher temperatures, the difference in thermal energy increases and the effect of photo-induced cooling takes place, which induces collisional heating by the bath gas towards thermal equilibrium [45, 79]. The presented effective fluorescence lifetimes and spectra of *p*-DFB were compared to existing data obtained for similar experimental conditions and showed only minor differences [94, 103]. The strong increase in laser stray light for temperatures above 1175 K in N_2 and 975 K in air indicate pyrolysis processes to take place; however, it is uncertain if it is due to soot particles or eroded cell material due to the possible formation of reactive fluorine-containing species.

The measured Stern-Volmer coefficients are the lowest that have been reported for aromatic fluorescence tracers so far. This means that quenching of this fluorinated single-ring aromatic by O_2 is comparatively weak, resulting in higher fluorescence intensities for otherwise equal conditions when the tracer is applied in air. The functional forms for calculating signal intensities of *p*-DFB and toluene from the Koban model suggest that due to the low overall temperature dependence of *p*-DFB the signal per molecule of *p*-DFB is more sensitive on quenching by O_2 than toluene for temperatures above 600 K.

5.3.7 Conclusions

Temperature dependent absorption spectra in the first electronic singlet absorption band of *p*-DFB were measured, and absorption cross-sections were derived at moderately high spectral resolution. For low and intermediate temperatures, the absorption cross-sections derived from laser measure-

ments at 266 nm differ from the ones determined from the recorded spectra. Despite the comparatively high spectral resolution of our setup (0.47 nm FWHM), the measurements are partly under-resolved leading to underprediction of the absorption cross sections by up to 30% for room temperature.

Fluorescence spectra and effective fluorescence lifetimes after picosecond laser excitation of gas-phase *p*-DFB were determined for a large range of gas-phase conditions commonly faced in LIF applications. Effective fluorescence lifetimes are used to determine relative fluorescence quantum yields. Vaporized *p*-DFB mixed with appropriate buffer gas was continuously flown through a heated ceramic cell inside a high-pressure vessel at temperatures in the range 296–1200 K, while the pressure could be varied between 1 and 10 bar. Normalized fluorescence spectra are presented as a function of temperature and O₂ partial pressure. On a logarithmic scale, the evaluated fluorescence lifetimes decrease with a smaller and larger slope in a lower and upper temperature regime, respectively, whose relative magnitudes also depend on the total pressure. For lower temperatures (<475 K for the data presented here), the fluorescence lifetime τ is independent of the total pressure, while at higher temperatures τ first decreases at lower pressures before becoming pressure independent.

The effect of O₂ on the fluorescence lifetime of *p*-DFB was also investigated and the fluorescence quantum yields are reduced less drastically than for other aromatic tracers (e.g., toluene, anisole, naphthalene) which makes *p*-DFB an interesting candidate tracer for measurements in air. Functional forms for predicting the relative signal intensity behavior with environmental conditions were derived from the available experimental data and are compared to similar data for toluene derived from the Koban model, which showed that the expected DFB signal per molecule is about two to three orders of magnitude stronger than that for toluene in many conditions typical for combustion experiments.

The large absorption cross-sections, high fluorescence yield, weak quenching behavior, together with its comparatively low trend towards thermal degradation or oxidative reactivity make *p*-DFB a valuable candidate as a gas-phase fluorescence tracer in LIF diagnostics for the study of mixing processes and for imaging of, e.g., temperature and mass fraction, which may be extended to temperature regions not accessible with other commonly employed aromatic fluorescence tracers. However, if the test conditions exceed 980 K in air, 1150 K in N₂ or include combustion, further kinetics studies involving this species are needed to provide data on the thermal decomposition, oxidation or formation of hydrofluoric acid and further explore its limits of applicability in high-temperature reactive systems.

5.4 Temperature, pressure, and oxygen quenching behavior of fluorescence spectra and lifetimes of gas-phase *o*-xylene and 1,2,4-trimethylbenzene

The following chapter is based on the journal paper "Temperature, pressure, and oxygen quenching behavior of fluorescence spectra and lifetimes of gas-phase *o*-xylene and 1,2,4-trimethylbenzene", published in Applied Physics B 124 (1) 2018, 70–83 by Thorsten Benzler, Torsten Endres, Thomas Dreier, and Christof Schulz.

Abstract

Ortho-xylene (1,2-dimethylbenzene, XL) and 1,2,4-trimethylbenzene (TMB) are promising aromatic fluorescence tracer species for gas-phase imaging measurements of concentration, temperature, and oxygen partial pressure. In the present work, temperature dependent gas-phase ultraviolet absorption spectra of XL and TMB were measured. In the investigated temperature range (296–725 K), the absorption bands red-shift with increasing temperature for both species and their absorption cross-sections increase. Time-resolved fluorescence spectra were recorded after picosecond laser excitation at 266 nm as a function of temperature (XL: 296–1025 K, TMB: 296–775 K), pressure (1–10 bar), and O₂ concentration using a streak camera coupled to a spectrometer. The fluorescence spectra of both species show a noticeable red-shift with increasing temperature and O₂ concentration. In N₂ as bath gas, the fluorescence lifetime of XL and TMB decreases by three orders of magnitude at the peak temperatures compared to room temperature. For both species, fluorescence quenching by N₂ (up to 10 bar) is temperature dependent and is strongest at about 500 K. Quenching by O₂ shortens the fluorescence lifetime for both species significantly. This effect is much reduced at higher temperatures. The temperature dependence of the Stern-Volmer coefficients that describe the effect of O₂ quenching, can be approximated by an exponential decay. Semi-empirical exponential fits to all investigated data (for XL and TMB) as well as published data for toluene were used to provide signal prediction models that are capable of predicting the signal intensities over a wide range of environmental conditions.

5.4.1 Introduction

Laser-induced fluorescence (LIF) imaging is one of the most widely applied measurement techniques for visualization of mixing processes and for determining gas-phase properties such as temperature and fuel/air ratios [4]. In these applications, tracer species with known photo-physical behavior and a high sensitivity of their fluorescence properties towards the studied parameters are added to non-fluorescent carriers (e.g., surrogate fuels and/or nitrogen or air) and the resulting signals are imaged onto cameras upon excitation of the tracers in the ultraviolet with laser light sheets. Various mixing studies have been conducted utilizing the tracer species toluene (TL), acetone, 3-pentanone and triethylamine (TEA) [60, 104, 105]. More recently, anisole [41] and difluorobenzene [106] have been suggested as tracers that provide particularly high signal levels [42]. In case of a liquid base fuel, it is also necessary to adjust the evaporation characteristics to

the respective measurement situation and to select a tracer that does not condense at the lowest temperatures present in an experiment [4]. It has been shown that combinations of two tracers can be exploited to visualize stratification of high- and low-volatility fuel components which requires tracers that particularly well match the properties of the respective volatility class [44]. For applications in diesel engine combustion, efforts were undertaken to further extend the choice of tracer species to 1-phenyloctane and 1-phenyldecane [90] or 5-nonanone [107] that meet the higher evaporation temperatures of diesel fuel. Therefore, there is a continuous interest in obtaining the required spectroscopic data of tracer species with various molecule sizes (and thus evaporation and transport properties). The quantities of interest include absorption cross sections and fluorescence quantum yields to enable quantitative signal evaluations in practical measurement situations as well as changes in absorption and emission spectra as a function of the bath gas composition, temperature, and pressure.

1,2,4-Trimethylbenzene (TMB, C_9H_{12}) and 1,2-dimethylbenzene (*o*-xylene, XL, C_8H_{10}) are two of the less common aromatic tracer species employed for fluorescence diagnostics [4, 60, 108], which feature spectroscopic properties similar to the frequently applied toluene (TL), but with higher boiling points (111, 144.4, and 170°C for TL, XL, and TMB, respectively). Due to their thermophysical properties, TMB and XL would be suitable tracers for mixing studies representing low-volatility diesel or high-volatility gasoline components. All of these structural analogues, TL as well as XL and TMB have similar fluorescence quantum yields (ϕ_{fl}) and are components of commercial fuels. However, since their concentrations vary and their fluorescence spectra overlap (also with additional fluorescing species), it is not possible to directly use the fluorescing components of commercial fuels for quantitative LIF measurements. Therefore, usually, non-fluorescent surrogate fuels are applied with one (or few) tracers added for visualization purposes.

For all three species, the center wavelength and spectral width of the first ($^1A_{1g} \rightarrow ^1B_{2u}$) absorption bands of interest are located in the near UV and are quite similar because methylation does not significantly change the π -electron system [81]. For practical applications, the dependence of essential parameters governing the generated LIF signal intensity, i.e., absorption cross-sections and ϕ_{fl} as well as their dependence on environmental conditions, i.e., temperature, pressure, and bath-gas composition (especially oxygen content), must be known and understood before quantitative LIF measurements are feasible. Due to their dense manifolds of thermally populated vibrational energy levels in the electronic ground state, the species exhibit almost structureless absorption bands at atmospheric pressure and above [4]. Apart from the varying absorption cross-sections, varying the excitation wavelength also results in a change in excess energy in the excited state and can therefore influence the spectroscopic parameters [102].

Temperature dependent relative fluorescence quantum yields for TMB have previously been determined by Rossow [10]. It was found that their variation with respect to temperature, pressure, and O_2 partial pressure is similar to that of TL. No study of the relative quantum yield of XL has been published up to now.

Fluorescence quantum yields can be derived from LIF-intensity measurements as long as the absorption cross-sections and the laser fluence are known and the tracer number densities are well controlled. Alternatively, the dependence of (relative) ϕ_{fl} on environmental conditions can be determined through the measurement of effective fluorescence lifetimes [6, 22], which makes the measurement independent of the determination of the parameters mentioned above, especially the uncertainties in tracer concentrations that often arise when preparing mixtures with bath gases at high temperatures and pressures. The fluorescence lifetime of TMB was recently presented by us for pressures up to 1 bar in the 295–475 K range [102]. We observed a change from increasing to decreasing FQY with increasing pressure for rising temperature, which could be explained by the difference of the relative thermal energy distribution and the excess energy right after excitation in the S_1 state.

The present work aims at extending the available database of XL and TMB into regimes of higher temperatures and gas pressures relevant in LIF-based optical diagnostics, e.g., in engines, shock tubes, or model gas-turbine sections. The spectral and fluorescence-lifetime data is also important for the further development of existing and new photo-physical models for the prediction of FQYs of these species. In the present work, we analyze the dependence of the absorption cross-sections of TL, XL, and TMB up to 725 K and fluorescence lifetimes of XL and TMB in up to 1075 K with picosecond laser excitation at 266 nm. Because literature data on temperature- and wavelength-dependent absorption cross-sections of toluene are sparse in the practically relevant temperature region and often spectrally under-resolved (which is relevant mostly in the lower temperature and pressure regions) [16], new measurements are presented here along with the respective data for XL and TMB. Measurements were carried out in pure N_2 from 1 to 10 bar total pressure and in N_2/O_2 mixtures with varying O_2 partial pressures at 1 bar total pressure. We also compare the expected signal intensities of XL and TMB with those of TL using semi-empirical models that consider the dependence on temperature (up to 1000 K), total pressure (up to 10 bar), and oxygen partial pressure (up to 209.5 mbar).

5.4.2 Theoretical background

For single-ring aromatics, methyl substitution adds vibrational modes and therefore increases the vibrational state density from TL (one methyl group) via XL (two) to TMB (three). Methyl substitution also results in an increase of the absorption cross-section and a red-shift of the spectra for $S_0 \rightarrow S_1$ transitions. This is due to the decrease of the 0–0 transition energy between the ground and the excited states with an increasing number of methyl groups [81]. In addition, at a given temperature, the higher density of states leads to a shift of the mean vibrational energy towards higher levels due to the Boltzmann distribution. Because this vibrational distribution is transcribed from the ground state to the electronically excited state during laser excitation, the excess energy in the excited state for the molecules with a high density of states is even higher (and higher than a simple 0–0 transition energy consideration would suggest).

As with most single-ring aromatic hydrocarbons, the S_1 state after 266-nm excitation can undergo

radiative (with fluorescence rate k_{fl}) and non-radiative deactivation, whereby the latter processes are dominated by intersystem crossing (rate: k_{ISC}) and internal conversion (from S_1 to S_0 , rate: k_{IC}) [4]. Other collision-induced non-radiative deactivation processes k_q are electronic quenching by bath-gas molecules, including ground-state target species such as the carrier gas (e.g., N_2) and O_2 , the latter being the most efficient quencher because of its triplet ground state [4]. The total depopulation rate, k_{tot} , then is inversely proportional to the experimentally accessible effective fluorescence lifetime, τ_{eff} [65]:

$$k_{tot} = k_{fl} + k_{ISC} + k_{IC} + k_q = \frac{1}{\tau_{eff}} \quad (13)$$

The relation between τ_{eff} and the fluorescence quantum yield, ϕ_{fl} , is given by

$$\phi_{fl} = \frac{k_{fl}}{k_{tot}} = \frac{\tau_{eff}}{\tau_{fl}} = k_{fl} \tau_{eff}, \quad (14)$$

with τ_{fl} , the natural lifetime [65]. Thus, the fluorescence quantum yield is proportional to the effective fluorescence lifetime τ_{eff} .

For quenching by O_2 , a Stern-Volmer relation

$$\frac{S_{fl}^0}{S_{fl}} = \frac{\tau_{eff}^0}{\tau_{eff}} = 1 + k_{SV} n_q \quad (17)$$

often holds, i.e. a linear dependence of the fluorescence signal intensity ratio S_{fl}^0 / S_{fl} (and thus $\tau_{eff}^0 / \tau_{eff}$) without (S_{fl}^0) and with (S_{fl}) presence of the quencher with its number density n_q (e.g., [10, 20, 52]). The respective Stern-Volmer factor, k_{SV} , can be extracted by linearly fitting the ratio of measured signal intensities (or fluorescence lifetime) for various quencher concentrations and the respective measured values without quenching (i.e. S_{fl}^0 / S_{fl} or $\tau_{eff}^0 / \tau_{eff}$) vs. the quencher concentration n_q .

The strong temperature dependence of the quantum yield and the fluorescence lifetime of toluene is explained by the vibrational excess energy that increases with temperature and boosts non-radiative relaxation processes (intersystem crossing and internal conversion) [10, 22]. The influence of pressure on the quantum yield was described previously for TL and TMB for up to 1 bar which corresponds well to results for even higher pressures [10, 23, 102]. One therefore expects similar behavior for all three methyl-substituted single-ring aromatics investigated here.

5.4.3 Experiment

5.4.3.1 Absorption experiments

Absorption measurements were performed in an optically accessible stainless-steel high-temperature cell that is continuously purged with the respective tracer/bath-gas flow (Figure 45) [96]. It was used at atmospheric pressure and can be heated in a cylindrical oven. The temperature was monitored by a K-type thermocouple mounted inside the cell close to the measurement volume. A deuterium lamp (LOT Oriel) was used as broadband UV light source to record absorption spectra

in the 230–300 nm range. A quartz plate in front of the cell entrance window splits off part of the incoming light beam for recording I_0 . This reference signal as well as the light transmitted through the cell was then coupled into a quartz Y-fiber, spectrally dispersed by a spectrometer (Horiba, iHR320; $f = 320$ mm, 1200 grooves/mm grating), and detected by a CCD camera (Horiba, Syncerity; 256×1024 pixels). The Y-fiber allowed the positioning of the dispersed light from both arms on top of each other onto different regions (50×1024 pixels each) of the CCD chip – from now on referred to as “reference” and “signal”. An exposure time of 1 ms and an entrance slit of $200 \mu\text{m}$ were used to make good use of the 16 bit dynamic range of the camera while maintaining a spectral resolution of 0.47 nm (75 cm^{-1} at 250 nm). Spectra were then generated by binning over 50 rows per channel and dividing the signal by the reference.

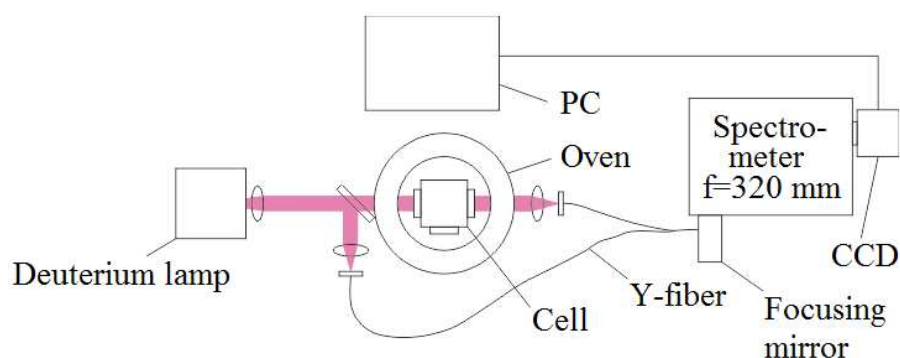


Figure 45: Experimental arrangement for absorption cross-section measurements.

5.4.3.2 Fluorescence experiments

The experimental setup for the time-resolved detection of fluorescence spectra is identical to the one presented in detail in Ref. [22], therefore only a brief description is given here. Fluorescence measurements were carried out in a gas mixture of the evaporated tracer and the respective bath gas flowing through an externally heated (up to 1200 K) cylindrical ceramic chamber contained inside an optically-accessible stainless-steel pressure vessel (up to 10 bar). The tracer species were excited at 266 nm by the beam of a frequency-quadrupled picosecond Nd:YAG laser (pulse width 26 ps, at 10 Hz) with typical pulse energies of 1 mJ at the measurement volume entering and exiting through 10 mm thick quartz windows. The signal was imaged onto the slit of a spectrograph (ARC, SP2300; $f = 300$ mm, 150 grooves/mm grating) connected to a streak camera (Hamamatsu Photonics, model C5680-24C). The system thus delivers images with a wavelength (nominally 0.2 nm/pixel) and a time axis (down to 0.2 ps/pixel depending on the total duration of the time trace).

5.4.3.3 Gas handling and linearity check

TMB, XL, and TL (Merck Chemicals, for analysis grade) were filled into glass containers and bubbled through with N_2 to drive out dissolved O_2 before feeding an HPLC (high performance liquid chromatography) pump (Bischoff-Chrom, model Compact Pump 2250). The liquids were vaporized in a heated chamber (Bronkhorst, CEM) with part of the flow of the carrier gas (vaporized from liquid N_2) and afterwards mixed with additional carrier gas. For the absorption experi-

ment, increasing tracer concentrations (from 0.1 to 1 mbar partial pressure) were fed to the cell at each temperature to ensure that measurements took place in the linear absorption regime, which then were averaged. For the fluorescence experiments, N₂ (vaporized from liquid N₂) and compressed air were used as bath gas for pressures up to 6 bar, while gas from cylinders (Air Liquide, 4.9 grade) was used for experiments above 6 bar. To avoid condensation, all tubes were resistively heated and kept at 470 K. The O₂ partial pressure in the chamber was varied by mixing air with varying amounts of N₂.

Fluorescence intensities were investigated as a function of laser fluence to determine the limits of the linear LIF regime (not shown here). Linear behavior was observed when the laser fluence was kept below 35 mJ/cm² at 296 K for XL and TMB, which is consistent with data previously reported for TL [23]. This laser fluence was used for temperatures up to 900 K. Because the saturation regime is known to shift to higher laser fluences at elevated temperatures [97], for reasons of gaining a better signal-to-noise ratio, the fluence level was increased stepwise to 50 mJ/cm² at the highest temperatures investigated which was also checked to be in the linear regime. The partial pressures of XL and TMB were set to 1.8 mbar at 296 K (20 μl/min liquid tracer in 2 l/min buffer gas, number density $\sim 4 \times 10^{22} \text{ m}^{-3}$). At higher temperatures, the liquid flow of the tracer was increased to maintain a nearly constant number density in the probe volume. In additional measurements it was tested that at these number densities and laser fluences self-quenching [98] can be neglected. The temperature, pressure, and bath-gas conditions in the absorption and fluorescence experiments are summarized in Table 9.

Table 9: Experimental conditions for spectral and fluorescence lifetime measurements presented in this work.

	XL		TMB	
	Spectra	Lifetimes	Spectra	Lifetimes
T / K	298–1075	298–1075	298–1025	298–1075
$p_{\text{tot}} / \text{bar}$	1–10		1–10	
$p_{\text{O}_2} / \text{mbar}$	5.1–210		8.7–210	

5.4.4 Date evaluation

5.4.4.1 Absorption experiments

For each lamp-based measurement, 200 camera images with detection times of 50 ms each were averaged for noise reduction. Figure 46 shows sample spectra of the deuterium lamp intensity (signal) through the N₂-filled cell ($I_0(\lambda)$, red line) and with a mixture of toluene (partial pressure 0.8 mbar) in 1 bar N₂ at 296 K ($I(\lambda)$, black line). After dark-signal subtraction, the absorption cross-section was then calculated using Lambert-Beer's law

$$\sigma_{\text{abs}}(\lambda) = \frac{\ln \left(\frac{I_0(\lambda)}{I(\lambda)} \right)}{d n}, \quad (44)$$

with the absorption path length d as the distance between the quartz windows (11 cm), and the tracer number density n . Both measurements, with and without tracer, were conducted for all tem-

peratures since the transmission characteristics of the cell slightly changed with temperature.

The measured emission spectra of a Hg(Ar) UV light source (LOT-Oriel pen-ray LSP034) were used to determine the spectral resolution of the system (FWHM: 0.47 nm). This is important (especially at low temperatures and pressures) where the spectral features have a similar or smaller width. Note that data in literature are often spectrally under-resolved (as is also the case here and in literature), which can lead to a significant deviation in absorption cross-sections between the reported lamp measurements and the data relevant for excitation with a narrowband laser. As an example, the peak absorption at 267 nm reported by Koban et al. [16] for room temperature and atmospheric pressure that was measured with an estimated FWHM of 1.5 nm is 20% lower than our value with the current achievable spectral resolution of FWHM = 0.47 nm of our system.

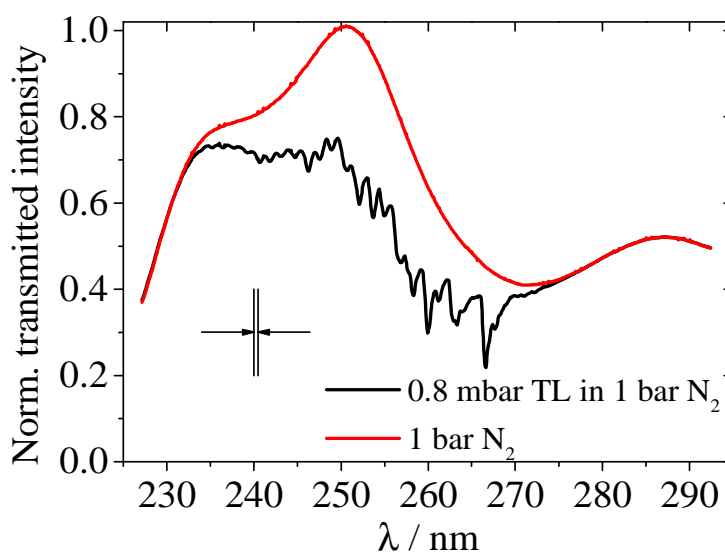


Figure 46: Spectral intensity distribution of deuterium lamp transmitted through the N_2 -filled cell (red line) and after filling with 0.8 mbar TL in 1 bar N_2 at 296 K (black line). The arrows indicate the spectral resolution of the detection system of 0.47 nm (FWHM).

5.4.4.2 Fluorescence experiments

For each condition, 1000 individual single-shot measurements were acquired and stored. To compensate for temporal jitter, the time axis of the measured signal trace was shifted according to a jitter-correction (Hamamatsu software) that adjusts the time axis to the measured initial signal rise and that is applied to each individual camera image before pulse-averaged images were formed. The software-based jitter correction has been tested by alternatively coupling a small fraction of the laser beam into the spectrometer via an optical fiber that bypasses the experiment. Using the laser peak as reference for the jitter correction gave the same results as the software-based jitter correction that adjusts the time axis to the measured initial rise in LIF signal.

A background image was subtracted that was obtained with the streak camera while the laser was firing with pure N_2 flowing through the cell. Resulting sample images for both tracers are shown in Figure 47 with calibrated wavelength and time axis. These images deliver wavelength-specific temporal profiles (horizontal binning of columns) and fluorescence spectra for specific time inter-

vals (vertical binning of rows) after laser excitation. It was found that within the error limits (variation below 5%), the number of binned columns did not influence the evaluated effective fluorescence lifetimes, i.e. there was no measurable dependence of the fluorescence lifetime on the emission wavelength. Therefore, the signal-to-noise ratio was enhanced by averaging pixel counts within columns covering the spectral range between 265 and 350 nm for XL and between 270 and 360 nm for TMB. Fluorescence spectra were determined by binning a number of rows in the range of significant pixel counts. The resulting spectra were corrected for the instrument spectral response by recording emission spectra of a deuterium lamp with known spectral radiance using the same optical setup. While the recorded tracer fluorescence showed a gradual variation in intensities and red-shift with increasing temperature, above certain (species and bath-gas specific) temperatures, dramatic changes occurred both in intensity and emission spectra. These were attributed to tracer decomposition and oxidation as reported before [22, 41] and investigated in more detail for toluene in specific high-temperature experiments in shock tubes [40].

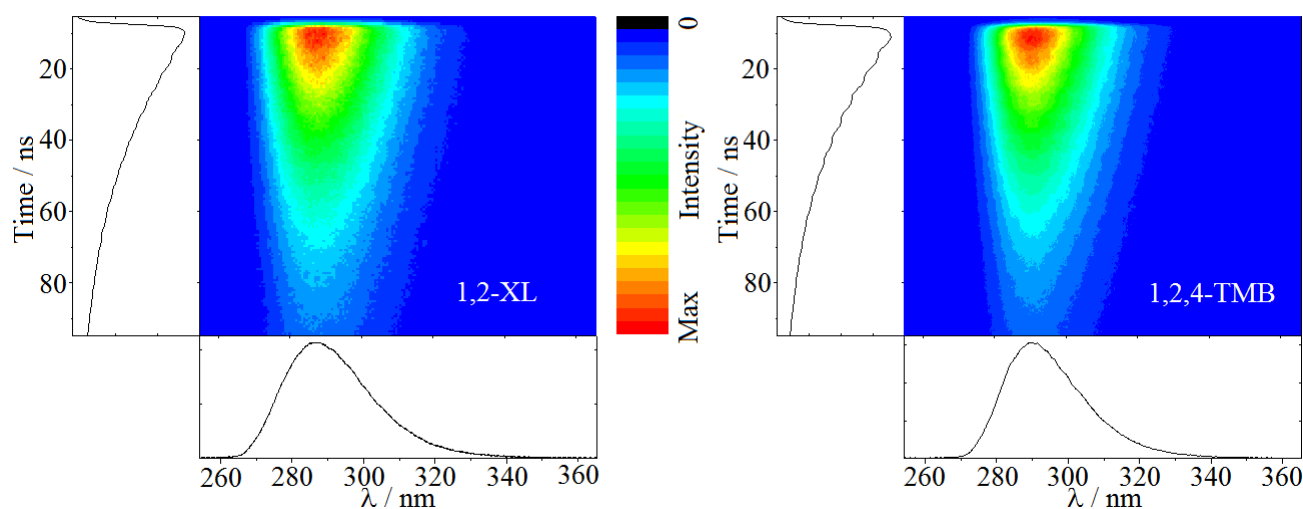


Figure 47: Spectrally- and temporally-resolved fluorescence (color coded) after excitation at 266 nm of XL (left) and TMB (right). Conditions: Temperature: 296 K, 2 mbar XL or TMB in N_2 , total pressure: 1 bar. Solid lines: signal integration along the time axis results in the plotted spectral profiles (bottom: spectra) and along the spectral axis the decay profiles (left: fluorescence intensity–time traces).

Figure 48 presents examples of LIF excitation/decay profiles for each species for three temperatures. Because the fluorescence decay times strongly vary depending on the environmental conditions, the sweep time of the streak tube needs to be adjusted to detect the entire signal trace on the full height of the CCD, which also influences the resulting time resolution of the setup. The temporal instrument function is measured using the stray light from the picosecond laser pulse in the absence of tracers and shown in Figure 48. For the fastest decays, the minimum temporal resolution of the detection system is 25 ps FWHM.

Signal decay times τ were determined using the convolve-and-compare method [99]. A convolution of a single- or double-exponential decay with the measured instrument response function was least-squares fitted to the experimental excitation/decay profiles. Figure 48 shows examples of this fitting procedure for each species using mono-exponential decay functions (red lines) for the room

temperature data (black dots). Fitting parameters are the decay time, the signal amplitude, and a temporal shift to optimize the instance where experimental and simulated signal intensities reach their respective peak values.

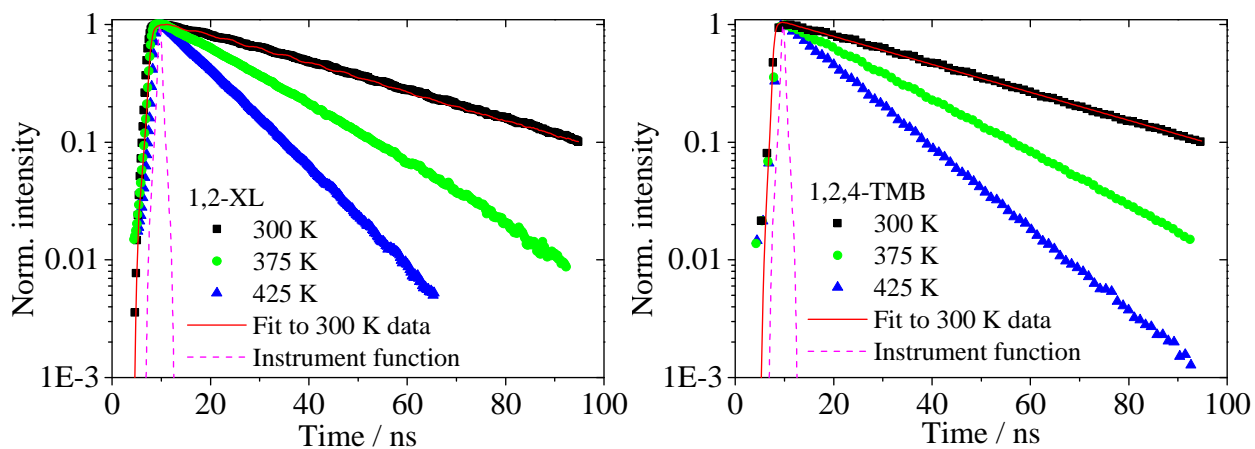


Figure 48: Time-resolved measurements of the fluorescence intensity for XL (left) and TMB (right) in 1 bar N_2 with excitation at 266 nm at various temperatures. For 300 K the fitted convolution functions are shown as red lines. The instrument response (dashed magenta lines) was recorded from laser stray light for the same streak settings chosen for the measurements at the respective lowest temperature.

5.4.5 Results

5.4.5.1 Absorption cross-section

To verify that the absorption experiments provide reliable data, spectra of TL were recorded as a well-documented reference case, and are presented for a range of temperatures in Figure 49 (upper left). Our own measurements (solid lines) are compared to data from Koban et al. [16] at three temperatures (dashed lines). Our new data are in close agreement with the earlier results. The upper right and the lower left panel in Figure 49 show the absorption cross-sections of XL and TMB for a range of temperatures. All the spectra show a characteristic band structure that is most prominent at low temperatures but can be recognized almost up to the highest temperatures investigated. Although the spectral resolution of the lamp measurement is quite good ($0.47 \text{ nm FWHM} \approx 75 \text{ cm}^{-1}$ at 250 nm), cf. arrows in Figure 49 as determined by the FWHM of a recorded mercury line at 254 nm from a low-pressure discharge lamp), the spectra are still under-resolved at low temperatures compared to highly-resolved spectra of Etzkorn et al. (resolution $\approx 23 \text{ cm}^{-1}$) [35] and Fally et al. (resolution $\approx 1 \text{ cm}^{-1}$) [36]. It is apparent from Figure 49 that the much better resolution of the narrow vibrational and rotational structure can lead to up to 80% higher peak values.

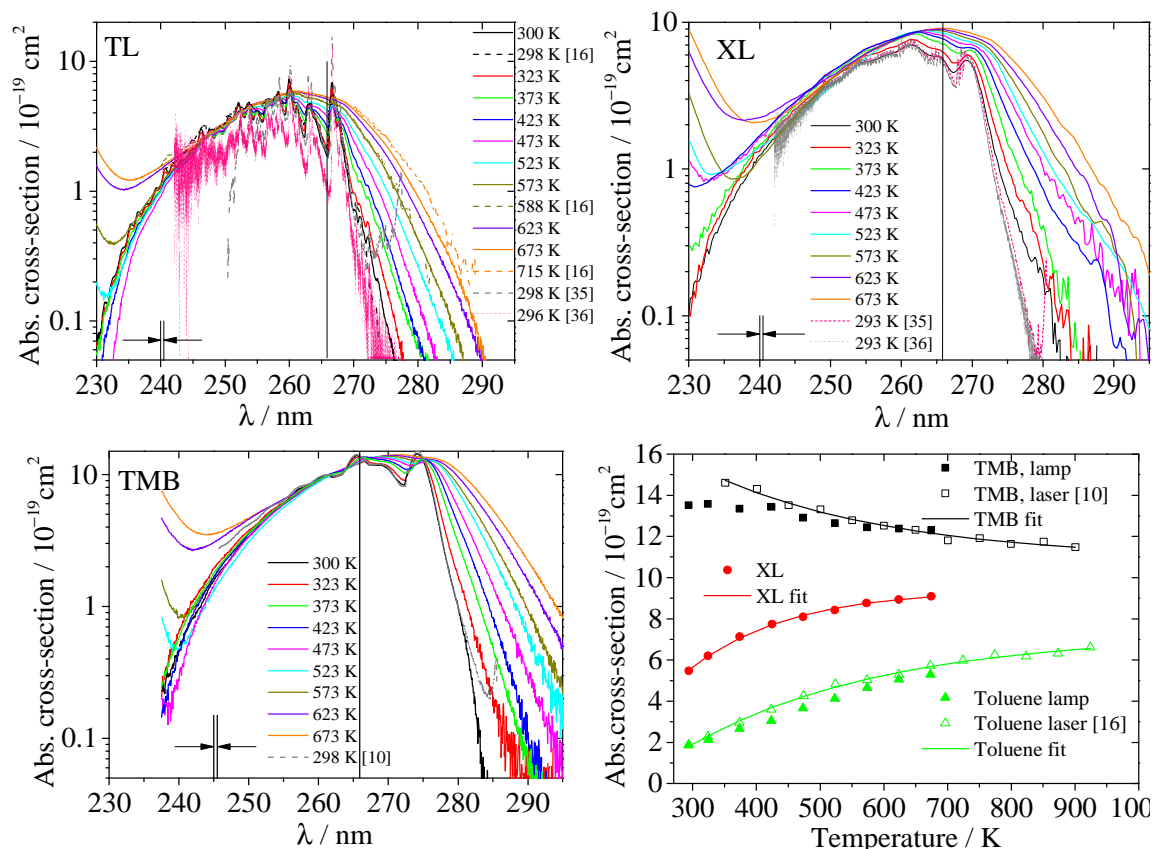


Figure 49: Absorption spectra of TL (upper left), XL (upper right), and TMB (lower left) at various temperatures in 1 bar N_2 . The arrows indicate the spectral resolution (0.47 nm FWHM). Results from Koban et al. [16], Etzkorn et al. [35] and Fally et al. [36] are plotted for comparison. Lower right: Absorption cross-sections at 266 nm determined from the spectra (solid symbols) and the laser measurements (open symbols) with fits based on the function given in Table 10. Literature data from Koban et al. [16] and Rossow [10]. While the fluctuations and deviation from the references for low absorption cross-sections represent noise, the structure reported at room temperature in the data from Etzkorn et al. [35] and Fally et al. [36] are considered real and originate from vibrational structure.

The absorption spectra of XL and TMB red-shift with increasing temperature and the cross-sections increase slightly, as it is the case for TL. At the same time, the spectra of all species broaden towards the long-wavelength side. With increasing temperature, a strong band below 230 nm emerges that represents $S_0 \rightarrow S_2$ transitions that become accessible due to increasing thermal population of higher vibrational states in the S_0 level. The lower right panel shows the data from the lamp measurements at 266 nm (solid symbols) compared to laser-based absorption measurements (open symbols) [10, 16] together with respective fit functions (function in the first row in Table 10, and parameters in Table 11). The fit functions for TL and TMB were generated with the laser-based results since their temperature exceeded those measured with the lamp. The reduced values of the lamp data towards lower temperatures (below ~ 400 K in case of TMB) are a result of the insufficient spectral resolution close to the spectral peak near 266 nm. However, the small deviation shows that the spectral resolution in our measurements are high enough to cause a $<20\%$ deviation even at room temperature.

5.4.5.2 Fluorescence spectra

Fluorescence spectra of TL [22], XL and TMB are shown in Figure 50 for a series of temperatures in 1 bar N₂, normalized to their respective peak intensities. To reduce noise, the spectra were smoothed by an adjacent-average filter with a window size of 2 nm.

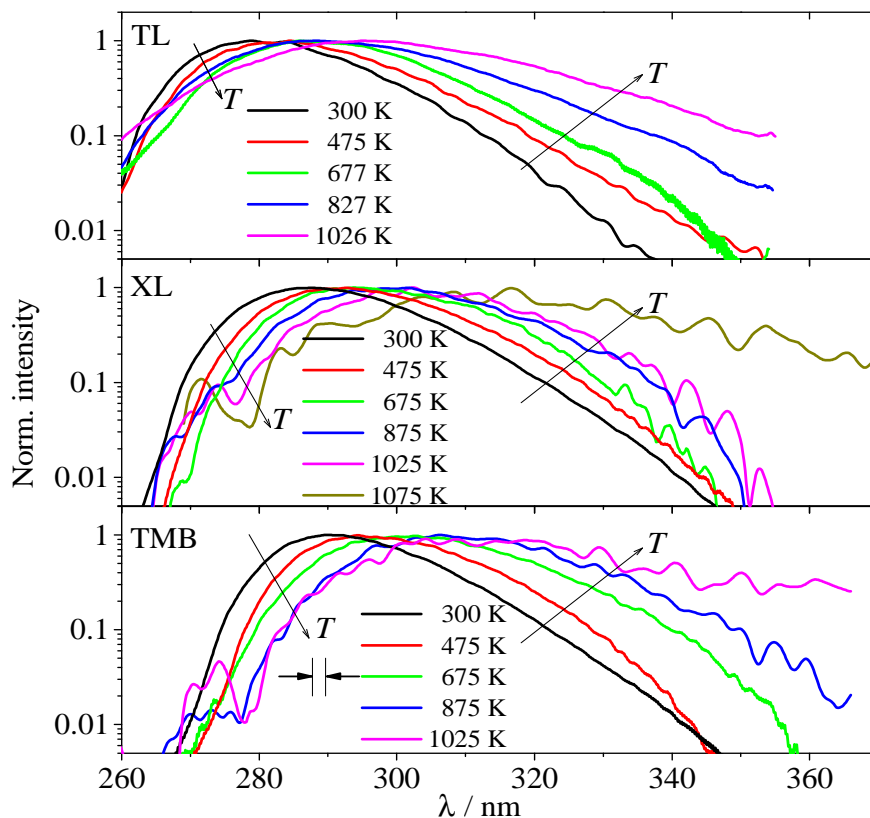


Figure 50: Peak-normalized fluorescence spectra of TL [22], XL, and TMB at various temperatures in 1 bar N₂ after excitation at 266 nm. The signal-to-noise ratios get low at higher temperatures, resulting in a wavy structure. Number densities of XL and TMB were kept constant at $\sim 2 \times 10^{23} \text{ m}^{-3}$ independent of the temperature. The arrows show the spectral resolution of the detection system derived from measurements with a Hg lamp. The arrows indicate the trends with increasing temperature.

As expected, for temperatures up to 875 K, the overall spectral signatures of the three methyl-substituted single-ring aromatics are quite similar with respect to peak position and half width. At room temperature, the spectra of XL and TMB peak at 287 and 290 nm (FWHM: 28 and 25 nm, respectively). In agreement with Nijegorodov et al. [85], these positions are red-shifted compared to toluene (280 nm) having a single methyl group. The result for TMB is in rough accordance with the data from Rossow [10] where at 350 K a peak position of 285 nm and a FWHM of 30 nm were determined. With increasing temperature (up to 875 K), a slight red-shift of about 2.3 nm/100 K for XL and 2.5 nm/100 K for TMB is observed, the latter being slightly lower than that measured by Rossow [10] who reported $3.6 \pm 0.6 \text{ nm/100 K}$. Toluene shows a lower red-shift of 2.0 nm/100 K [22]. In the same temperature range, the half widths increase by approx. 12 and 29%, respectively.

For higher temperatures, a much larger apparent shift is observed. This is attributed to the onset of pyrolysis as studied in more detail for species like anisole in shock tubes [40]. Because of this effect, the temperature dependent measurements presented in this work end at 1075 K. Below, the respective tracers are considered stable on the time scale of the experiment. In the present experiments a possible fine structure of the spectra observed at lower temperature is smeared out due to the limited spectral resolution of about 1.9 nm (indicated by the arrows in Figure 50).

In the presence of O₂, the fluorescence spectra red-shift additionally (Figure 51), which is mostly linear with the O₂ partial pressure. The redshift from pure nitrogen to air (210 mbar at 1 bar total pressure) is roughly equivalent to a temperature increase of 100 K. This effect is stable (within the error limits) for the investigated temperature range.

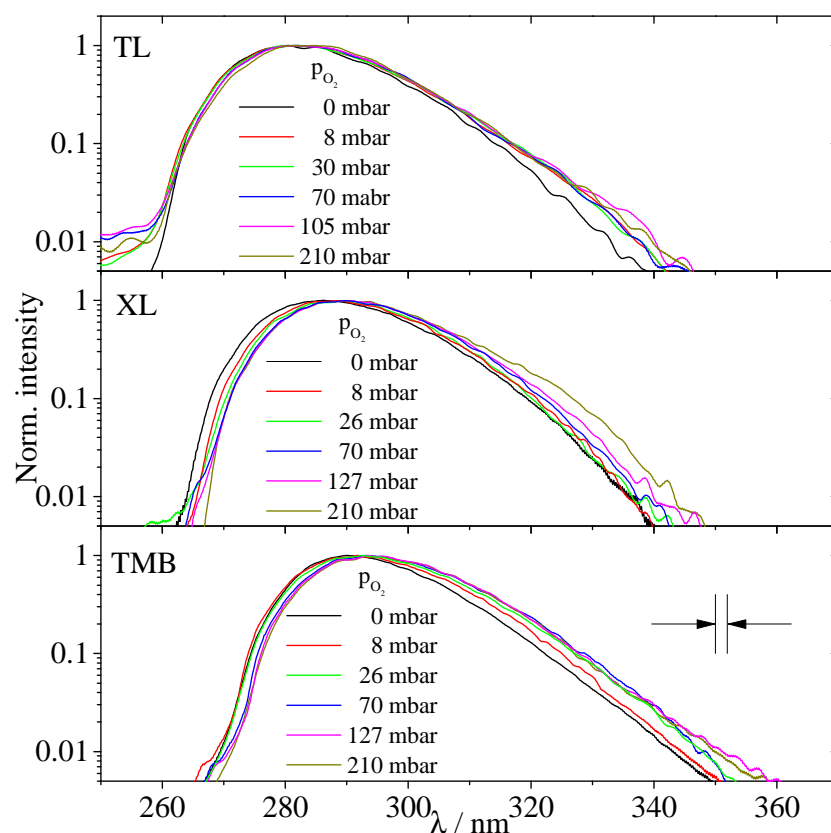


Figure 51: Peak-normalized fluorescence spectra of TL, XL, and TMB at various O₂ partial pressures, 1 bar total pressure at room temperature (296 K) after excitation at 266 nm. Number densities of TL, XL and TMB were kept constant at $\sim 2 \times 10^{23} \text{ m}^{-3}$ independent of the bath gas composition. The arrows show the spectral resolution of the detection system derived from measurements with a Hg lamp. The arrows indicate the trends with increasing O₂ partial pressure.

All data for the center-wavelength of the fluorescence spectra for XL and TMB and even an old data set of TL are presented in Figure 52. The center wavelength was determined by the mean value of the FWHM- border positions. This was the preferred method over, e.g., the integral mean value, because all redshift values and trends were the same, but the results show reduced scatter.

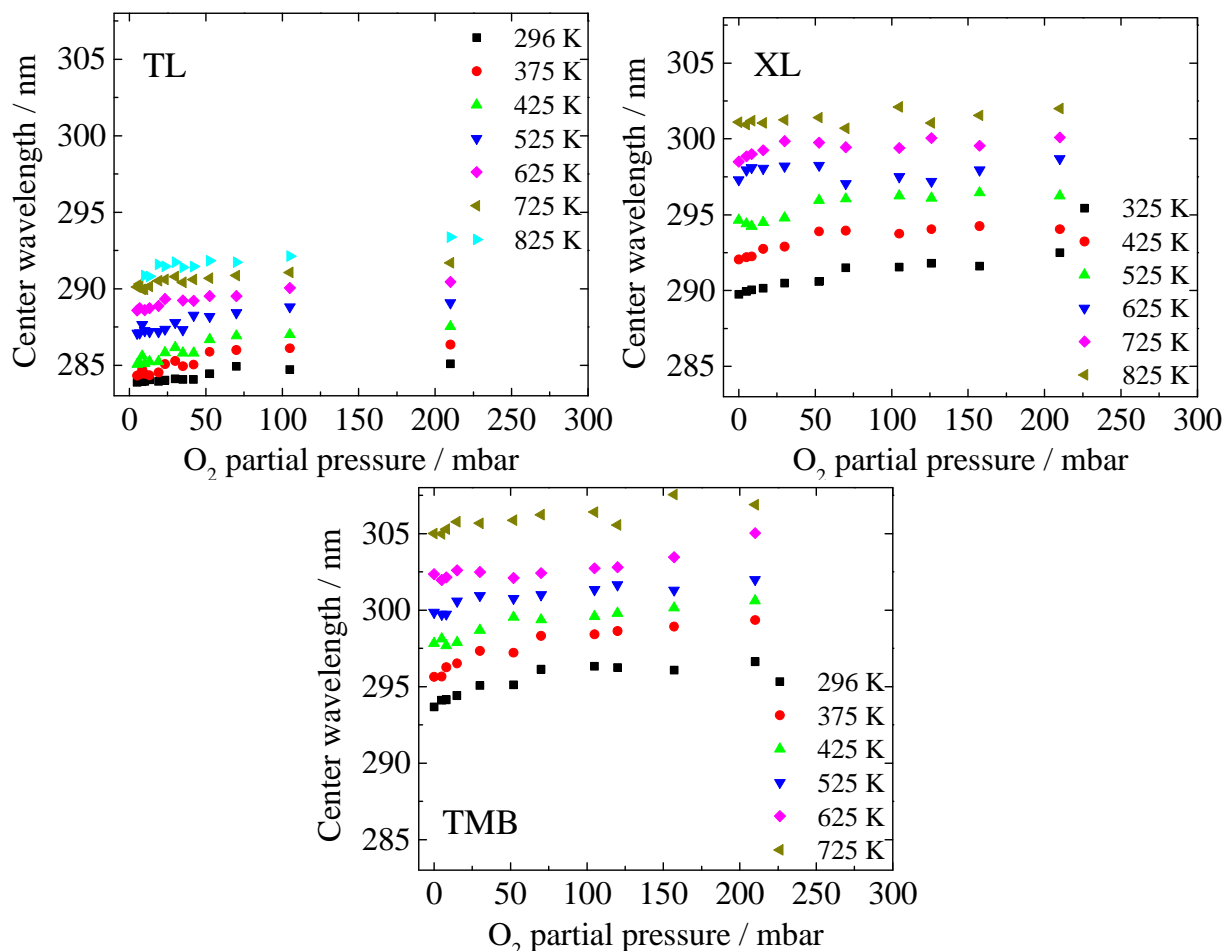


Figure 52: Temperature- and O_2 partial pressure-dependent center wavelength (determined from the average FWHM positions). The wavelength as well as the temperature dependent redshift increases from TL (upper left panel) over XL (upper right panel) to TMB (lower panel).

5.4.5.3 Effective fluorescence lifetimes

Nitrogen bath gas

Following the procedure outlined in section 5.4.4.2, effective fluorescence lifetimes of XL and TMB diluted in N_2 were determined (Figure 53). All error bars in the upcoming sections were determined from the standard deviation of multiple measurements or in case of single measurements, the uncertainties of the fitting procedure presented in section 5.4.4.2 was used for estimating errors. In the explored temperature range, the fluorescence lifetimes of XL and TMB decrease by three orders of magnitude, whereby the decrease is slightly stronger at higher pressures. The dependence can be approximated reasonably well by $c(T, p_{\text{tot}}, p_{O_2}) \tau(T)$ presented in Table 10.

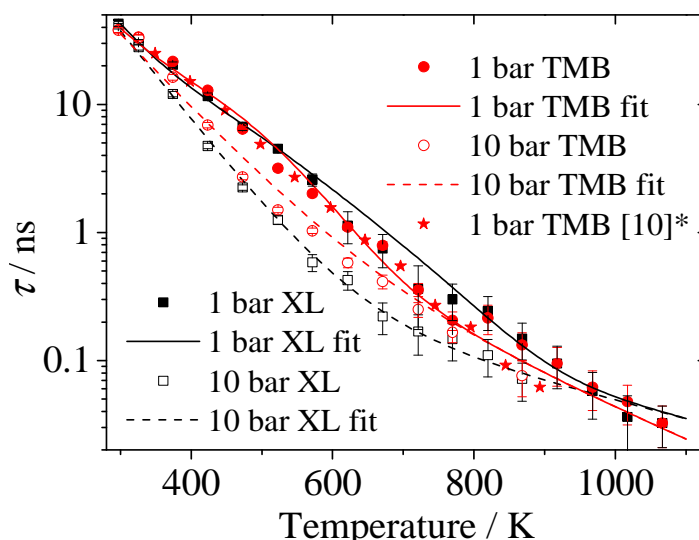


Figure 53: Effective fluorescence lifetimes of XL and TMB in N_2 as a function of temperature for 1 and 10 bar. ϕ_{fl} data from Rossow [10] (red stars) are normalized to lifetimes at 350 K. Solid lines are taken from the model introduced in section 5.4.5.3.

Our temperature dependent fluorescence lifetimes for TMB at 1 bar obtained from time-resolved measurements (solid red circles Figure 53) correlate well with the data calculated from relative ϕ_{fl} from Rossow [10] that were determined from spectrally-integrated fluorescence intensities measured at 350–900 K and normalized to the lifetime value at 350 K (red stars).

Figure 54 shows that the fluorescence lifetimes slightly decrease with increasing pressure. The overall trend with pressure and temperature is similar for XL and TMB. The room-temperature data of TMB are an exception showing a slight increase of the fluorescence lifetime with pressure. The effect of increasing fluorescence lifetime, the so-called photo-induced cooling effect, was first theoretically described by Wadi et al. [79] and experimentally tested for naphthalene by He et al. [45] while the more stabilizing effect of increased pressure was first described theoretically and experimentally proven for naphthalene by Beddard et al. [109]. This photo-induced cooling effect for TMB was experimentally shown and explained by us before for studies at sub-atmospheric pressures [102], where we discussed the importance of collision-induced vibrational relaxation in excited aromatic molecules by reducing the total pressure and therefore the collision frequency. The higher pressure data points from this study smoothly continue the previously described trend (Figure 54).

The decrease in fluorescence lifetimes with increasing pressure is stronger at moderate temperatures and flattens out at higher temperatures, most probably due to the fact that the fluorescence lifetimes become too short for the pressure-induced increase in collision frequency to show an effect. A similar quenching effect with N_2 was also observed by Rossow [10] for the spectrally-integrated TMB fluorescence intensities at 450 and 700 K, where a decrease in signal intensity was observed by about a factor of 1.9 and 1.3, respectively, when increasing the buffer gas pressure from 1 to 10 bar. This effect is weaker compared to that observed for toluene where the decrease was by a factor of 3 and 2.5 for 450 and 700 K, respectively. When normalizing the data

from Rossow [10] with the respective lifetimes at 1 bar of the fluorescence model introduced in section 4.4.5.3, the trends of both data sets show good agreement (Figure 54, right).

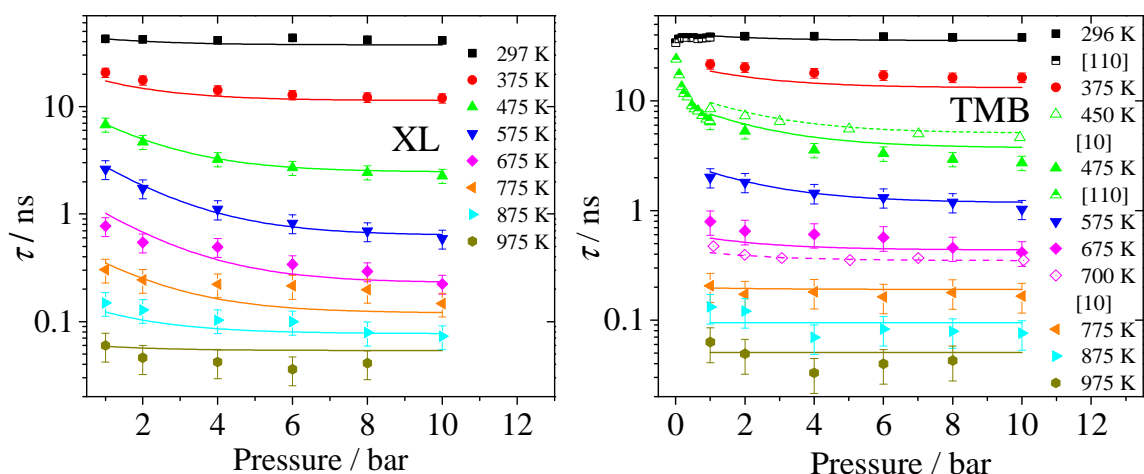


Figure 54: Pressure dependence of the effective fluorescence lifetimes of XL (left) and TMB (right) for a range of temperatures with additional data from [110] (data from 0–1 bar) and [10] (hollow symbols and dashed lines). The solid lines are simulations based on the model introduced in section 5.4.5.3.

N_2/O_2 mixtures as bath gas

Figure 55 shows fluorescence lifetimes of XL and TMB in atmospheric pressure N_2/O_2 mixtures with various partial pressures of O_2 as a function of temperature. As the comparison in both graphs shows for the case of pure N_2 (filled black squares), quenching by O_2 is most efficient at lower temperatures, and is almost independent of the O_2 partial pressure at the highest temperatures investigated. At room temperature, when a mixture equal to dry air at 1 bar is used, the fluorescence lifetime of XL and TMB decreases by a factor of 84 and 89, respectively, with respect to the values in pure N_2 . This behavior is similar to that reported for TL [22]. Except for the lowest O_2 partial pressures, the measured lifetimes exhibit a shallow maximum as a function of temperature which is shifted to higher temperatures with increasing O_2 partial pressures.

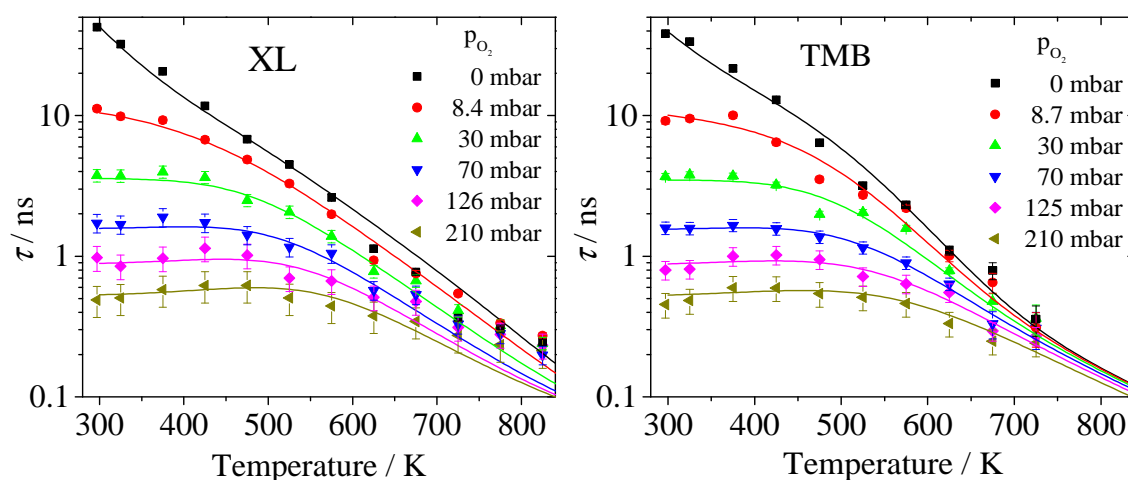


Figure 55: Effective fluorescence lifetimes of XL (left) and TMB (right) as a function of temperature for various O_2 partial pressures in N_2 at a total pressure of 1 bar. Solid lines are simulations based on the model introduced in section 5.4.5.4.

It was shown in previous work that the quenching efficiency of toluene shows Stern-Volmer behavior. This was deduced either from spectrally- and temporally-integrated fluorescence intensities [10, 20] or from fluorescence lifetime measurements [22]. In the present work, Stern-Volmer coefficients for XL and TMB were determined according to Eq. (17) for various temperatures from the slopes of the fluorescence lifetime data versus inverse O₂ partial pressure. The resulting temperature dependent Stern-Volmer coefficients for quenching of XL and TMB by O₂ are shown in Figure 56 together with values from Koban et al. [16], Faust et al. [22], and Rossow for TL [10], as well as from Rossow for TMB [10].

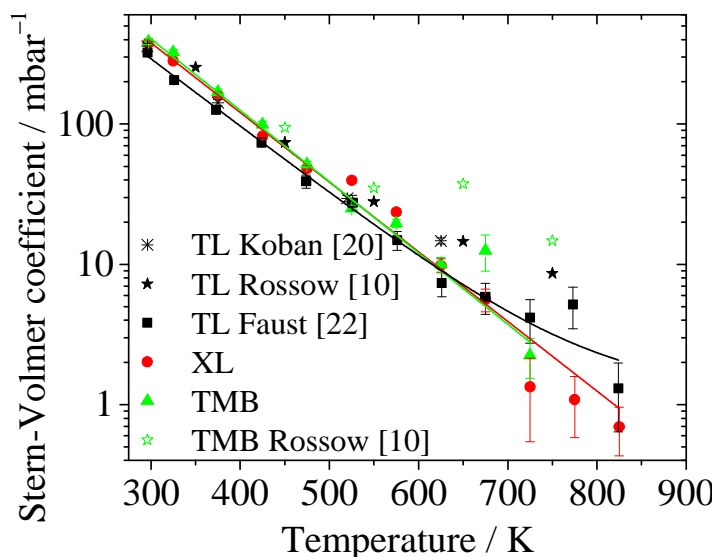


Figure 56: Stern-Volmer coefficients for O₂ quenching of TL, XL, and TMB as a function of temperature. Lines are mono-exponential fits to the TL data of Faust et al. [22, 23] and our present data.

There is overall agreement for TMB for the lower temperatures, but the deviations between Rossow and our data become significant at higher temperatures. This could be due to the different measurement techniques (our more direct fluorescence lifetime method vs. the fluorescence-intensity method) and can (to some extent) also be seen in the toluene data. However, there is almost the same trend with temperature in our data for XL and TMB which is further emphasized by the extended data for TL from Faust et al. [23] which also takes high pressure data in air (up to 10 bar) into account.

5.4.5.4 Model functions

In the following, a semi-empirical model – based on the work by Koban et al. [16] – is introduced for predicting the temperature, total pressure, and O₂ partial pressure dependence of the relative fluorescence quantum yield, ϕ_{fl} , of the methyl-substituted single-ring aromatics investigated in this work. One simplification made in Koban's fluorescence model for TL [16] was the neglect of the effect of total pressure on ϕ_{fl} . That model was extended by Faust et al. [23] to take total pressure into account:

$$\phi_{fl}(T, n_{O_2}) = \left[\frac{A_1(\lambda_{exc}, T)}{1 + k_{SV,1} n_{O_2}} + \frac{A_2(\lambda_{exc}, T)}{1 + k_{SV,2} n_{O_2}} \right] \left[B_1(T) \exp\left(-\frac{p_{tot}}{B_2(T)}\right) + B_3(T) \right] \quad (46)$$

In this equation, the first term considers the temperature and O₂-quenching dependent ϕ_{fl} originating from Koban et al., while the second term describes the dependence on the total pressure.

Both models, however, cannot predict the fluorescence signal in air above atmospheric pressure. This is due to the fact that $k_{SV,2}$ is given as a linear function of temperature, which will give negative values for $k_{SV,2}$ above 720 K, resulting in non-physical behavior and a strong failure in predicting measured fluorescence intensities for TL for high number densities of O₂ (blue dotted lines in left panel in Figure 57). Therefore, we will present a new model for TL in this section, which is able to predict the fluorescence signal per molecule even for high pressures in air for a large range of environmental conditions. The signal intensity per molecule for 266 nm excitation for all three tracer species can then be calculated from:

$$S_{fl} \sim \sigma_{abs}(266 \text{ nm}, T) \phi_{fl}(266 \text{ nm}, T, p_{tot}, p_{O_2}) = \sigma_{abs}(T) \frac{k_{fl} c(T, p_{tot}, p_{O_2}) \tau(T)}{1 + q(T) p_{O_2}} \quad (47)$$

This equation is basically identical to eq. (17) multiplied by the absorption cross-section (just like in the Koban model) and predicts the absorption cross-section times the fluorescence quantum yield for 266 nm and is therefore proportional to the signal intensity per molecule. Therefore, multiplying eq. (47) with the number density and the total pressure yields the LIF signal intensity per volume. The difference to the Koban model is that now there is just one quenching coefficient $q(T)$, which prevents singularities with the downside that it is not the Stern-Volmer coefficient. $\tau(T)$ represents the fluorescence lifetime of the average thermal energy level (ATEL) in S₁ while $c(T, p_{tot}, p_{O_2})$ is a correction factor taking into account the energy difference between the initially excited energy level and the ATEL of S₁ and the following collisional cascade. This was inspired by the step-ladder model of Thurber [68] and Koch [111]. The correction factor depends on the fluorescence lifetime which is why it also depends on temperature, total pressure, and O₂ partial pressure. This model can (with different parameters) as well predict the fluorescence signal of XL and TMB. All model parameters were determined by globally fitting equation (47) to all the toluene data of Faust et al. [22, 23] and the experimental data for XL and TMB presented in section 5.4.5.2.

Table 10 presents a collection of the different factors forming the model function (Eq. 47) while Table 11 lists all relevant fit parameters.

Table 10: Factors represented in the model function (Eq. 47) for deriving relative fluorescence signal strengths of TL, XL, and TMB. Pressure is in bar and temperature in K.

Absorption cross-section	$\sigma_{\text{abs}}(T) = \sigma_0 + \sigma_1 \exp\left(-\frac{T}{\sigma_2}\right)$
Fluorescence lifetime of the ATEL	$\tau(T) = \tau_0 + \tau_1 \exp\left(-\frac{T}{\tau_2}\right) + \tau_3 \exp\left(-\frac{T}{\tau_4}\right)$
Quenching coefficient	$q(T) = q_0 + q_1 \exp\left(-\frac{T}{q_2}\right)$
Total pressure correction	$c(T, p_{\text{tot}}, p_{\text{O}_2}) = \frac{c_0}{1 + c_1 \exp(-c_2 p_{\text{O}_2})} \exp\left(-\frac{(c_3 - T)^2}{c_4}\right) \times \exp\left(-\frac{(p_{\text{tot}} - 1)c_5}{1 + c_1 \exp(-c_2 p_{\text{O}_2})}\right) + 0.87$

Table 11: List of parameters used in the functional forms comprising the model function (Eq. 47) for TL, XL, and TMB. k_{fl} is the fluorescence rate constant derived from [29].

	TL	XL	TMB
σ_0	7.2537×10^{-19}	9.4226×10^{-19}	1.0903×10^{-18}
σ_1	-1.4249×10^{-18}	-2.4575×10^{-18}	1.2742×10^{-18}
σ_2	305.9	159.13	290.98
τ_0	4×10^{-11}	-	-
τ_1	1.4085×10^{-5}	5.4939×10^{-6}	2.4723×10^{-6}
τ_2	51.48	61.777	72.111
τ_3	-	1.5447×10^{-9}	1.2047×10^{-8}
τ_4	-	301.73	180.85
q_0	0.1	0	0.92254
q_1	93306	43341	21072
q_2	51.48	61.777	71.458
c_0	13.96	3.1974	0.97566
c_1	11.66	8.4352	11318
c_2	2.87	5.8824	0.006913
c_3	642.25	628.92	512.39
c_4	27576	33067	19257
c_5	0.19	0.56184	0.46988
k_{fl}	5.90×10^6	8.19×10^6	1.22×10^7

Figure 57 compares the new toluene model to the older ones. As one can see, it predicts the fluorescence intensity for high-pressure high-temperature conditions in air better than the old ones. Because there is no data for high pressure in air for temperatures above 800 K, at higher temperatures we cannot assess the correctness of the data extrapolated based on the model (light blue line).

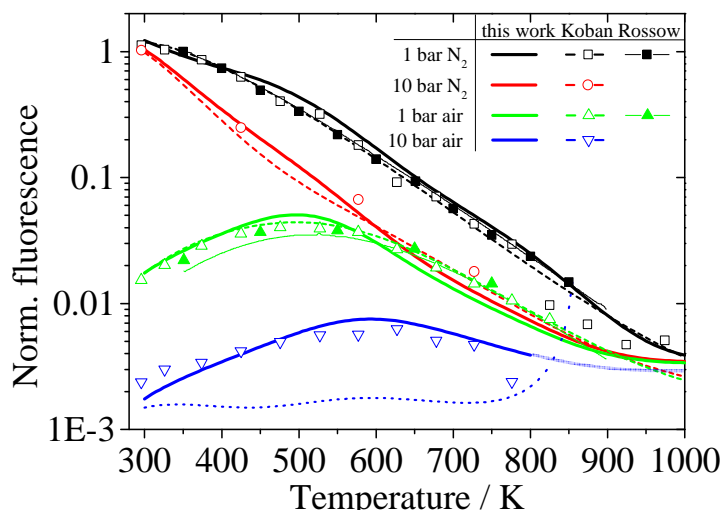


Figure 57: Comparing the extended Koban model (dashed lines) [23] and the photophysical model of Rossow (solid lines) [10] for toluene with our new model (heavy lines). Respective measurements from Koban and Faust (open symbols) [22, 23] and from Rossow (solid symbols) [10].

Figure 58 compares the expected fluorescence signal (derived from fluorescence lifetimes) per molecule for TL, XL, and TMB in the temperature range from 300 to 1000 K for N₂ and air at 1 and 10 bar total pressure, respectively. Overall, the signal of TMB is the strongest among these three tracers, apart from temperatures above 800 K and high O₂ partial pressures, where the signal of XL exceeds the one of TMB. The signal of TL is overall the weakest of the methylbenzenes, at least on a per-molecule basis.

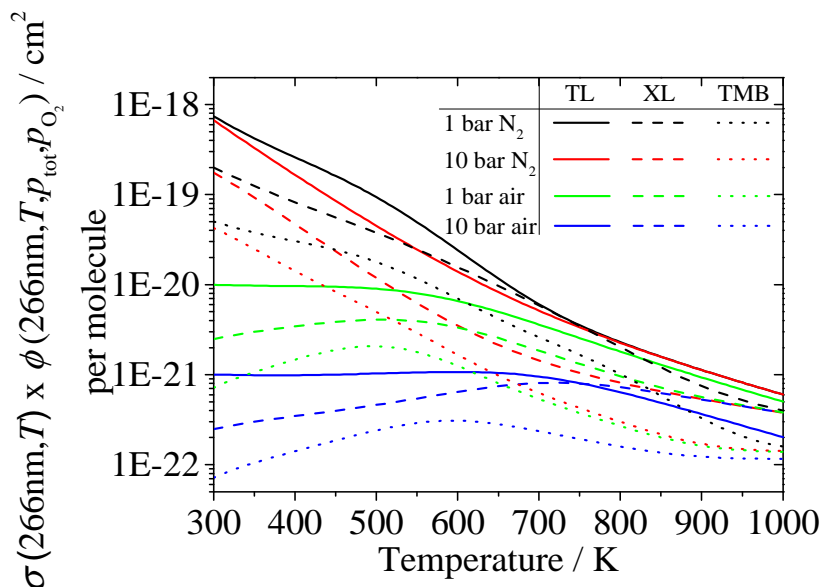


Figure 58: Fluorescence signal per molecule in air and N₂ for 1 and 10 bar predicted from Eq. (61) for TL (dotted lines), XL (dashed lines), and TMB (solid lines).

The model was created and derived from fluorescence lifetime data presented in previous and the current work for temperatures from 296 to 1000 K without O₂, and up to 800 K in the presence of O₂ for total pressures up to 10 bar air. Due to the choice of the implemented fit functions no non-physical behavior (e.g., singularities) is expected for higher temperatures, pressures or O₂ partial pressures.

Comparisons between the model and the experimental data are shown in Figure 53 (temperature dependence), Figure 54 (total pressure dependence), and Figure 55 (O_2 partial pressure dependence). As one can see, the model is capable to describe all experimental results (in the given error estimation). In case of XL and TMB, the overall agreement with the experimental data is very good. The mean relative errors of the model are 12.6%, 13.2% and 11.1% for TL, XL, and TMB, respectively, calculated by averaging the relative model error of all available data points. Thus, the model describes all three species similarly well.

5.4.6 Discussion

The presented absorption spectra of toluene, *o*-xylene and 1,2,4-trimethylbenzene (Figure 49) are in good agreement with the literature data for room temperature from Koban [16], Etkorn [35], and Fally [36], while the retrieved absorption cross-sections at 266 nm follow the trend of temperature dependent laser absorption measurements of Koban [16] and Rossow [10]. There are deviations ($\sim 10\%$) for TMB between the laser absorption measurements from Rossow and our deuterium lamp data in the region below 450 K that are attributed to slightly under-resolving the spectral features at these temperatures. The trends of the absorption cross-section retrieved at 266 nm shown in Figure 49 can be explained from the general variation of the spectra with temperature: All three absorption spectra red-shift, broaden, and increase in cross-section with temperature due to the spread in thermal population towards higher vibrational levels. The laser absorption data of TL and TMB was used to create fit functions for the absorption cross-section for these species at 266 nm, since they cover a broader temperature range and are also considered more reliable at low temperatures where the spectrometer measurements tend to provide under-resolved data. The maximum deviation of our data at 266 nm from literature values is 15% at room temperature and the deviation diminishes at higher temperatures.

The increase or decrease in the fluorescence lifetime of various tracers with increasing pressure in the sub-atmospheric pressure regime upon 266 nm excitation was discussed in detail in a previous publication [102], although in this case, apart from TMB at room temperature, the fluorescence lifetime always decreases with increasing pressure.

The effect of the so-called “third decay channel” [30] that describes the occurrence of an additional fast decay channel above a limiting temperature also applies to XL and TMB. Above 525 K for XL and 475 K for TMB, an additional, short lifetime component (τ in the range of <1 ns) can be observed in the fluorescence decay. However, we focused on the long lifetime component in this study, thus using only the longer decay constant from double-exponential fitting the fluorescence decay as explained in section 5.4.4.2.

The Stern-Volmer coefficients for TMB are in good agreement with values from Rossow [10] for low temperatures, but show increasingly larger deviation with increasing temperature. However, the data pool in [10] just consists of four points of which one was neglected for further analysis (the value at 650 K of Rossow in Figure 56). Our Stern-Volmer coefficients of XL and TMB show consistent trends and also correspond well with the extended data of Faust et al. [23]. We therefore

prefer the new data over the data reported in [10]. However, since it enabled to improve the quality of the fit, the quenching constant in the model was allowed to deviate from the Stern-Volmer coefficients, thus trading the quality of the fit over the strict physical meaning of the fit constants.

Overall, the discussed methylbenzene derivatives exhibit similar photophysical properties and thus are similarly applicable for LIF imaging measurements. For practical considerations, however, there are some important differences. The signal per molecule increases with each additional methyl group because of the increasing absorption cross-sections. In LIF experiments, however, the effective signal is sometimes limited by the vapor pressure of the tracer which is lower for the heavier species. In combination, the maximum achievable signal is comparable for all three species. TMB is advantageous if a strong signal per molecule is desired (one order of magnitude stronger signal-per-molecule compared to toluene). TMB also has advantages in the context of two-color thermometry, because its temperature-induced fluorescence red-shift is more pronounced compared to toluene, resulting in an enhanced temperature sensitivity. In terms of quenching by O_2 , the spectra are also shifted to the red by roughly the same amount as a 100 K temperature increase for a 210 mbar O_2 partial pressure rise. This effect is stable for all three molecules as well as all temperatures investigated in this study.

5.4.7 Conclusions

The spectroscopic properties of the three structurally-similar gas-phase fluorescence tracers with different vapor pressures toluene (TL), *o*-xylene (XL), and 1,2,4-trimethylbenzene (TMB) were investigated in terms of absorption spectra, fluorescence spectra, and effective fluorescence lifetimes. Measurements were conducted as a function of temperature, bath-gas pressure, and oxygen partial pressure in parameter ranges typical for tracer LIF diagnostics in practical applications. Spectrally- and temporally-resolved fluorescence measurements were obtained upon picosecond laser excitation with a streak camera coupled to a spectrometer. There is a spectral red-shift of the fluorescence peak with temperature of 2.3 and 2.5 nm/100 K for XL and TMB, respectively, as well as a spectral red-shift by oxygen of ~ 2 nm/100 mbar O_2 for both species. With increasing temperature, the fluorescence lifetime decreases significantly by a factor of ~ 3 ns/100 K in a similar fashion for both, XL and TMB. Higher total pressures enhance this decrease for both species. As for TL, O_2 is a strong fluorescence quencher for XL and TMB, and the Stern-Volmer factors derived for XL and TMB are larger than those of TL at room temperature. At 725 K range, O_2 quenching is reduced by roughly a factor of 200 for XL and TMB compared to room temperature, making them significantly less affected by oxygen quenching compared to TL at elevated temperatures.

A new semi-empirical model similar to the one of Koban et al. [16] is introduced for all three species. The measured absorption cross-sections and effective fluorescence lifetimes of toluene [22, 23] were used to validate the model and the model was compared to the one of Koban et al. [16] and Rossow [10]. The new model has the benefit of being able to predict signals at higher pressures in the presence of O_2 compared to the previous ones that were limited to peak partial pres-

tures of 0.21 bar O₂. The same model was used to predict relative LIF signal intensities for TL, XL, and TMB using a specific set of parameters for each species. All these parameters were determined through a global fitting routine to minimize the overall errors in the model. In the range of conditions where this model was validated (i.e., 300–1000 K, up to 10 bar in pure N₂ and at 1 bar for environments between pure N₂ and air composition) we found good agreement between the modeled and the measured fluorescence lifetimes as well as literature data.

5.5 Unpublished results

Some of my research results are not yet published. They complete the dataset of anisole and demonstrate the feasibility of 1-methylnaphtalene as an aromatic fluorescence tracer. Therefore, these results are presented in this section.

5.5.1 Anisole absorption cross-section

The absorption cross-section is one key parameter for the fluorescence signal of a tracer. Up to now, the σ_{abs} of anisole was only estimated by Faust et al. to be $\sim 10^{-17}$ cm² at room temperature for 266 nm excitation [41]. Since this estimate was rationalized by a comparison with *p*-cresole and phenol [35], some clarification of the true σ_{abs} was necessary. This was given even more emphasis by the point that experimental results did not show the expected signal increase for anisole that were predicted [42] and could neither be reproduced by Zabeti et al. at higher temperature in a shock tube [40]. The σ_{abs} shown in Figure 59 were measured by using the same experimental set-up and data processing procedures described in chapters 5.4.4.3 and 5.4.4.4.

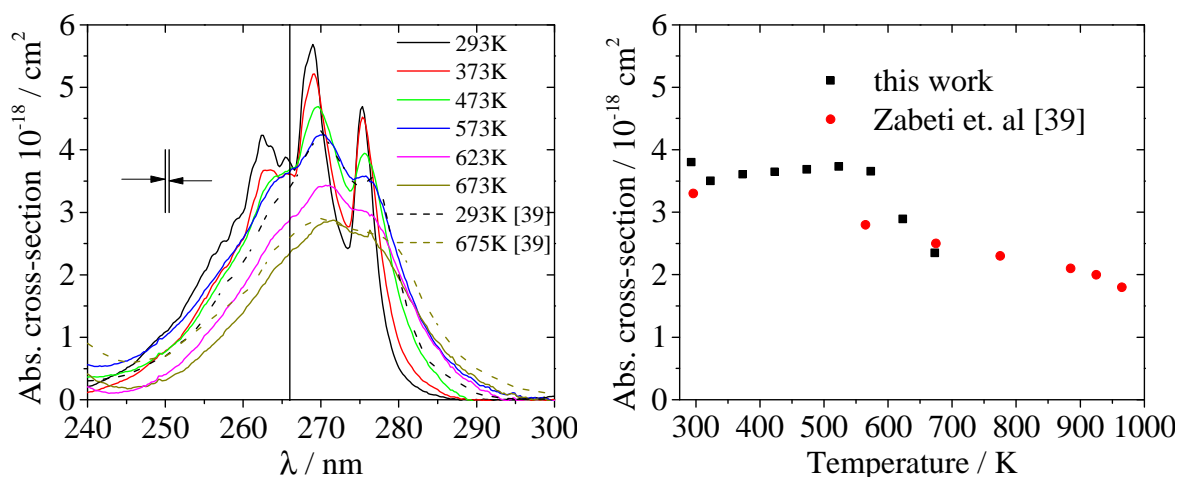


Figure 59: Spectrally-resolved absorption cross-sections of anisole determined with a deuterium lamp for various temperatures (left panel) and its temperature dependence for 266 nm (right panel). The attained spectral resolution of 0.47 nm of this measurement was determined via the FWHM of a recorded mercury line at 254 nm from a low-pressure discharge lamp.

The measured σ_{abs} is in accord with the results of Zabeti et al. [40], showing very similar values and trends. The room temperature data was measured at 120 mbar while the higher temperatures (565 to 965 K) were determined at 1.5 bar total pressure. Overall, the spectral resolution of the flow-cell measurement shown here is by an order of magnitude higher compared to Zabeti et al. (0.47 nm to ~ 7 nm). This explains the deviation in structure of both studies. The drop at 600 K may be ascribed to beginning tracer pyrolysis in the flow cell, reducing the number density of the parent molecule, depending on the kinetics. Residence times in hot areas of the cell (~ 2 s) before the measurement are longer than it is the case in a shock tube, explaining the faster decay of the absorption with temperature compared to the shock tube results around 600 K. The new results are also in accord with the results of the experimental comparison of LIF signal intensities mentioned

before [42]. The presented data is therefore verified by two independent experimental techniques.

5.5.2 1-Methylnaphthalene fluorescence

1-Methylnaphthalene (1MN) was identified as a suitable tracer for low-volatility fuels such as Diesel and kerosene by Kaiser and Long in 2005 [52]. Since then, not many investigations have been published on the photophysical characteristics of 1MN. There are clear benefits of using 1MN over naphthalene (e.g., that it is a liquid at room temperature), which justifies additional research as presented in this chapter. The experimental setup and data processing are the same as were published (chapter 5.3 and 5.4). The preferential evaporation study of Itani et al. [44] partially relies on the results presented here.

Fluorescence spectra

The fluorescence spectra of 1MN as a function of temperature in 1 bar N_2 , and for different O_2 partial pressures at 375 K at 1 bar total pressure are shown in Figure 60. The overall structure (double peak, see inset in Figure 60, left) of the spectra smears out with increasing temperature. The temperature dependent red-shift is relatively weak for 1MN (~ 2 nm/100 K). It is also noteworthy that the (peak-normalized) spectra not only shift, but also change shape, showing a relative spectral intensity increase around ~ 300 nm. This is not an absolute increase, just a part of the spectra that is not that much affected by the higher non-radiative deactivation paths, most likely due to the fact that this part of the spectrum originates from low excess energy states of S_1 (and therefore small non radiative deactivation rates). This behavior is not typical for aromatics (see chapter 5.3 and 5.4) and requires further investigation. This is also the case for the O_2 -dependent spectra (Figure 60 right panel). The normalized spectra, again, do not simply red-shift but change shape by narrowing. This just applies to the higher energy part of the spectra (~ 310 nm) while the low energy part (around 360 nm) is unchanged apart from the pure nitrogen measurement. The overall intensity shift is about 2 nm/100 mbar O_2 . Overall, this is a stronger effect than what was observed for the methylbenzenes (see chapter 5.4), and may be exploited for diagnostics purposes.

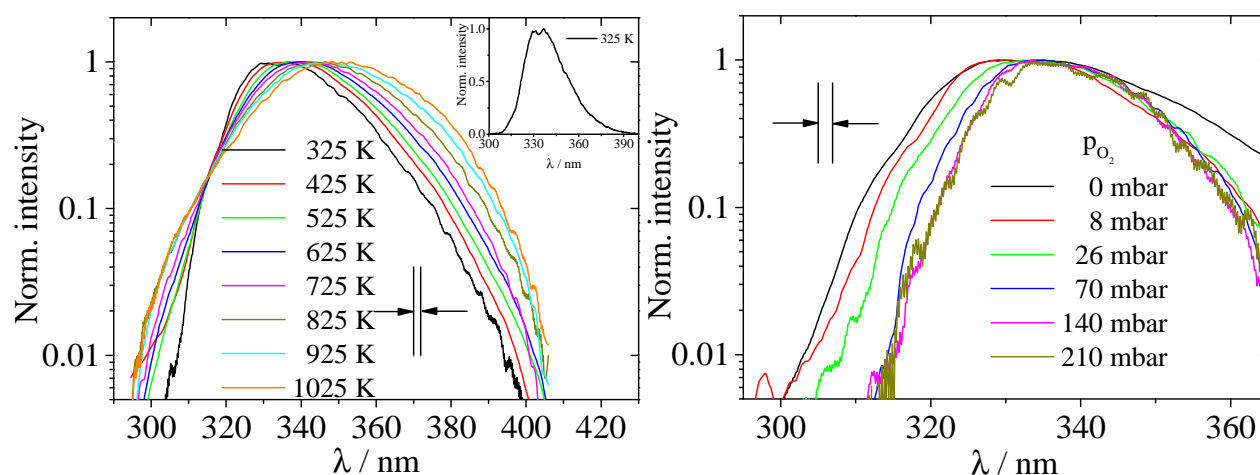


Figure 60: Temperature-dependent fluorescence spectra of 1MN after 266 nm excitation and at 1 bar total pressure in N_2 (left panel) and in dependence of O_2 partial pressure at 375 K 266 nm excitation and at 1 bar total pressure. Arrows indicate the instrumental spectral resolution.

The combination of the effects of these two parameters (temperature and oxygen partial pressure) on the fluorescence spectra of 1MN may pose some interesting options for two-color thermometry and fuel/air-ratio measurements.

Fluorescence lifetime in N₂

The evaluated fluorescence lifetimes depending on temperature (see 5.3 and 5.4 for details on set-up and post processing) for 1 and 10 bar in N₂ are shown in Figure 61. In the temperature region from 325 to 725 K, the fluorescence lifetime decreases by 75% for 1 bar and 84% for 10 bar. This is similar to other aromatic tracers that have been investigated so far. However, from 725 to 875 K (less than half of the temperature range mentioned above), there is an additional decrease in fluorescence lifetime by ~75%, also visible in a clear change in the slope of the temperature dependence (black lines in Figure 61). This is similar to what was reported for naphthalene by Faust et al. [23]. Overall, the fluorescence decrease with temperature is less pronounced when compared with the methyl-benzenes (toluene, xylene, trimethylbenzene) and quite comparable to naphthalene. Another interesting effect can be seen at roughly 600 K where the fluorescence lifetime at 10 bar (up to this point higher than at 1 bar) drops below that of the 1 bar measurement. A detailed explanation for this behavior is given in chapter 5.1.

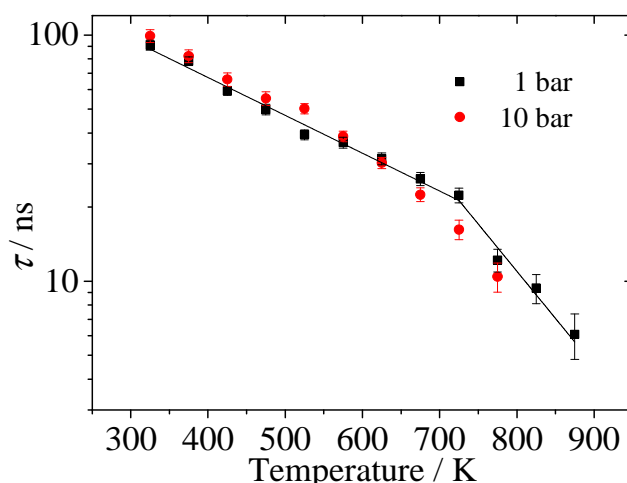


Figure 61: Temperature-dependent fluorescence lifetimes of 1MN at 1 and 10 bar total pressure in N₂ after 266-nm excitation together with two single-exponential decay curves to guide the eye.

Figure 62 illustrates this effect quite well. For low temperatures, the fluorescence lifetime increases with increasing pressure. At 625 K, there is practically no pressure dependence and for higher temperatures, the fluorescence lifetime decreases with increasing pressure. This is mirrored by the relation between the excess energy and the average thermal energy level (ATEL). As the ATEL rises above the excess energy that the molecule gets through excitation, collisions with environmental molecules stop to decrease the internal energy of the excited molecule and start to increase the energy. Since the non-radiative deactivation processes are energy dependent, this has an influence on these deactivation channels and the fluorescence lifetime (intensity) changes. As a result, the fluorescence lifetime decreases with increasing pressure at high temperatures.

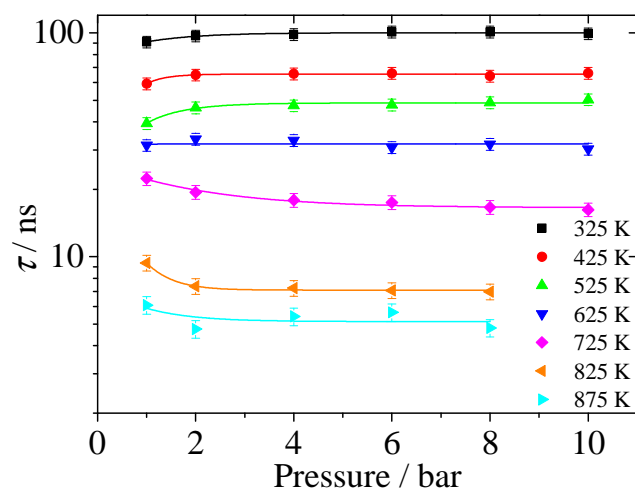


Figure 62: Pressure-dependent fluorescence lifetimes of 1MN at different temperatures in N_2 after 266-nm excitation together with mono-exponential decay curves to guide the eye.

Fluorescence lifetime in O_2 -containing mixtures

Figure 63 (left panel) shows the effect of O_2 quenching on 1MN by displaying the fluorescence lifetime as a function of temperature for different O_2 concentrations. The overall trend (i.e., decrease of lifetime with increasing oxygen concentration, with the effect becoming reduced at higher temperatures) is the same shown by all aromatics when exposed to varying concentrations of O_2 but the strength of the effect is different. The quenching efficiency (manifested by the Stern–Volmer coefficient) exceeds the one of toluene by a factor of 4 for low temperatures and decreases less with increasing temperature (Figure 63 right panel). The slope follows the trend of naphthalene quite closely.

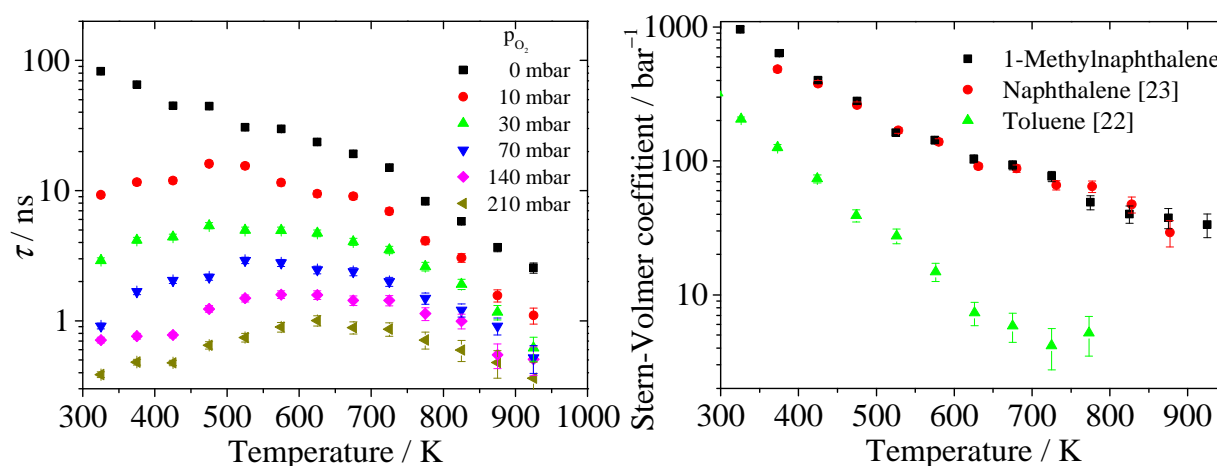


Figure 63: Left panel: Temperature dependent fluorescence lifetime of 1MN after 266 nm excitation in 1 bar total pressure for various O_2 partial pressures in the bath gas nitrogen. Right panel: Stern-Volmer coefficients of 1MN and naphthalene as a function of temperature. Toluene and naphthalene data from Faust et al. [22, 23].

Summary

The fluorescence characteristics of 1MN are interesting from a standpoint of fundamental understanding of the underlying photo physics and for diagnostics applications. However, the tracer is also difficult to handle: Its high viscosity and boiling point makes it resistant towards cell cleaning using pumping, or flushing, even at higher temperatures. The vapor pressure of 1MN is low, reducing the possible fluorescence signal per volume. Apart from that, the signal per molecule in N_2 that just depends on the σ_{abs} (known from personal communication [112]) and the ϕ_{fl} is as high as the signal of DFB and several orders of magnitude higher than that of, e.g., toluene. The red-shift of the spectra pose challenges since the spectrum does not only shift but also changes shape, but it also provides chances for simultaneous two-color thermometry. The strong susceptibility to O_2 quenching may also be beneficial for some applications (e.g., FARLIF) for high contrast (although the overall signal is relatively low). There is still work to do for this tracer (e.g., σ_{abs} measurements, model development, ...) but chances are that 1MN will improve optical diagnostics in IC engines at some point in the future.

6 Potential LIF tracer data summary

The efficient use of commercial fuel will be an ongoing topic for scientists, politicians, and every user of gasoline alike. For improvement, more detailed and more specific analysis of gas-phase mixing and combustion processes are necessary. This however demands more specific fluorescence tracers that either give better signal-to-noise ratio or improve the realism of the experiment e.g., by following the evaporation characteristic of commercial fuel more closely. The results presented in this thesis are helping to achieve this goal and this chapter will summarize some of the photophysical information that was gathered so far.

An overview for the absorption cross-section (Figure 64), the relative fluorescence lifetime (Figure 65) and the Stern–Volmer coefficients (Figure 66) in dependence on temperature is given. These graphs make it easier to compare the different tracers and choose the one most suitable for a specific application.

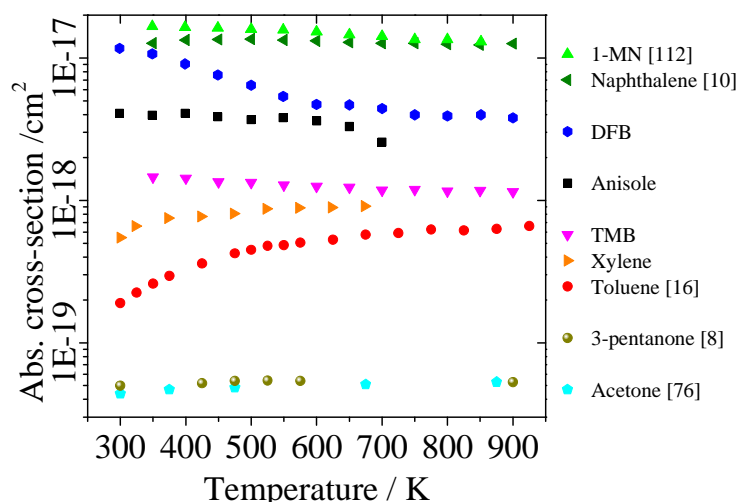


Figure 64: Absorption cross-section of several ketones and aromatics as a function of temperature.

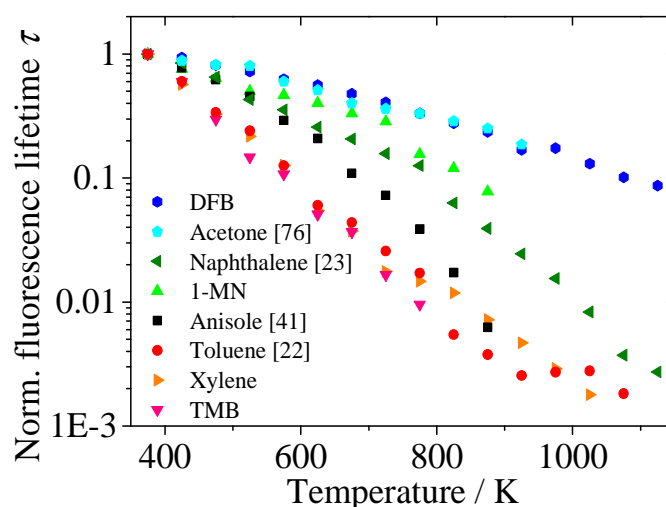


Figure 65: Relative fluorescence lifetimes normalized to 375 K of several ketones and aromatics as a function of temperature.

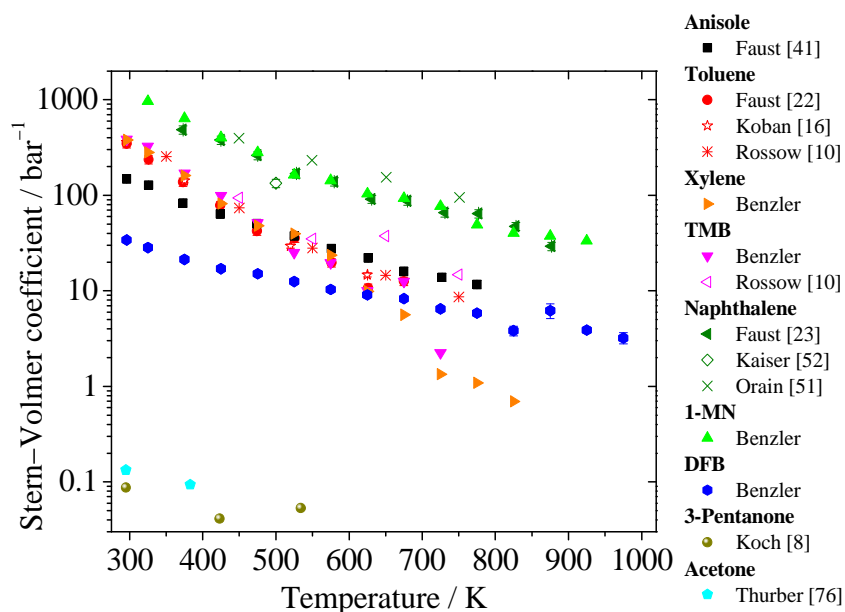


Figure 66: Stern–Volmer coefficients of several ketones and aromatics as a function of temperature.

In order to condense this information, several fluorescence intensity models have been developed over the years for comparison. Figure 67 and Figure 68 give the expected fluorescence intensity per molecule for common aromatic and ketone tracer molecules as well as new models introduced by the publications presented in Chapter 5.3 and 5.4. Since the vapor pressure at room temperature dictates the amount of tracer that can be added to a surrogate fuel before nonlinearity and / or self-quenching interfere with measured comparison data, Figures 69 and 70 are multiplied by the number density present at 10% of the respective vapor pressure at 293 K [80]. Therefore, these Figures describe the fluorescence intensity per cm^3 according to $n \sigma_{\text{abs}} \phi_{\text{fl}}$.

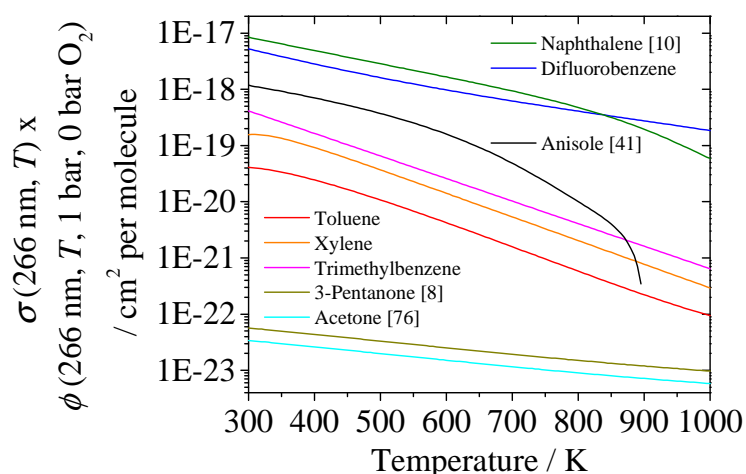


Figure 67: Comparison of the fluorescence intensity per molecule for selected aromatic and ketone tracers after excitation with 266 nm in 1 bar N_2 as a function of temperature.

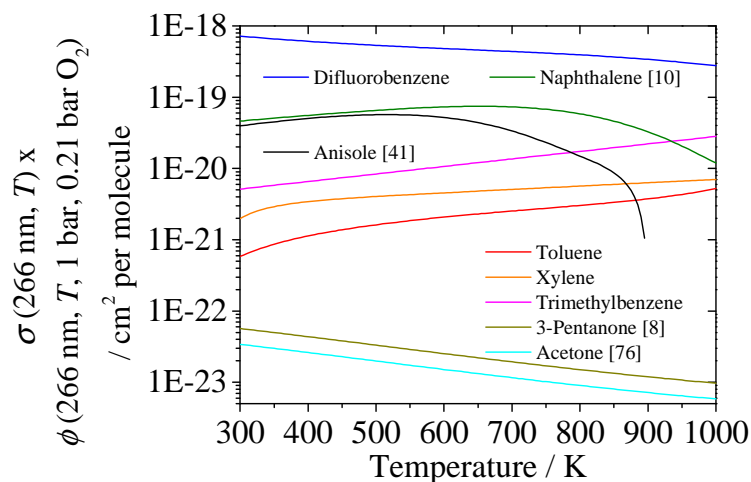


Figure 68: Comparison of the fluorescence intensity per molecule for selected aromatic and ketone tracers after excitation with 266 nm in 1 bar air as a function of temperature.

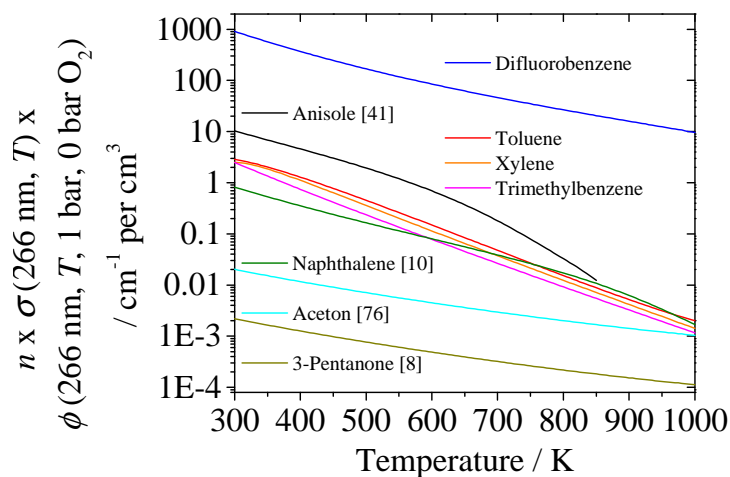


Figure 69: Comparison of the fluorescence intensity per cm^3 for selected aromatic and ketone tracers (number density equivalent to 10% vapor pressure at 293 K each) after excitation with 266 nm in 1 bar N_2 as a function of temperature.

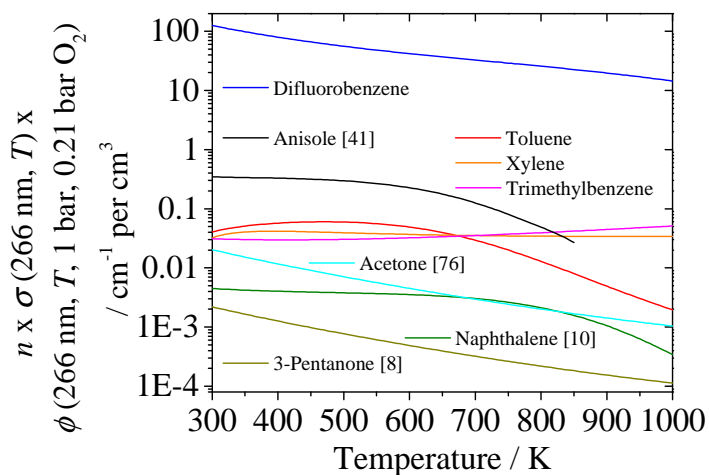


Figure 70: Comparison of the fluorescence intensity per cm^3 for selected aromatic and ketone tracers (number density equivalent to 10% vapor pressure at 293 K each) after excitation with 266 nm in 1 bar N_2 as a function of temperature.

The real benefit of these fluorescence intensity models comes after the choice of the right tracer for the application at hand. Figure 71 gives an idea of the information one can extract from these models on hand of the fluorescence intensity model of toluene that was presented in chapter 5.4.

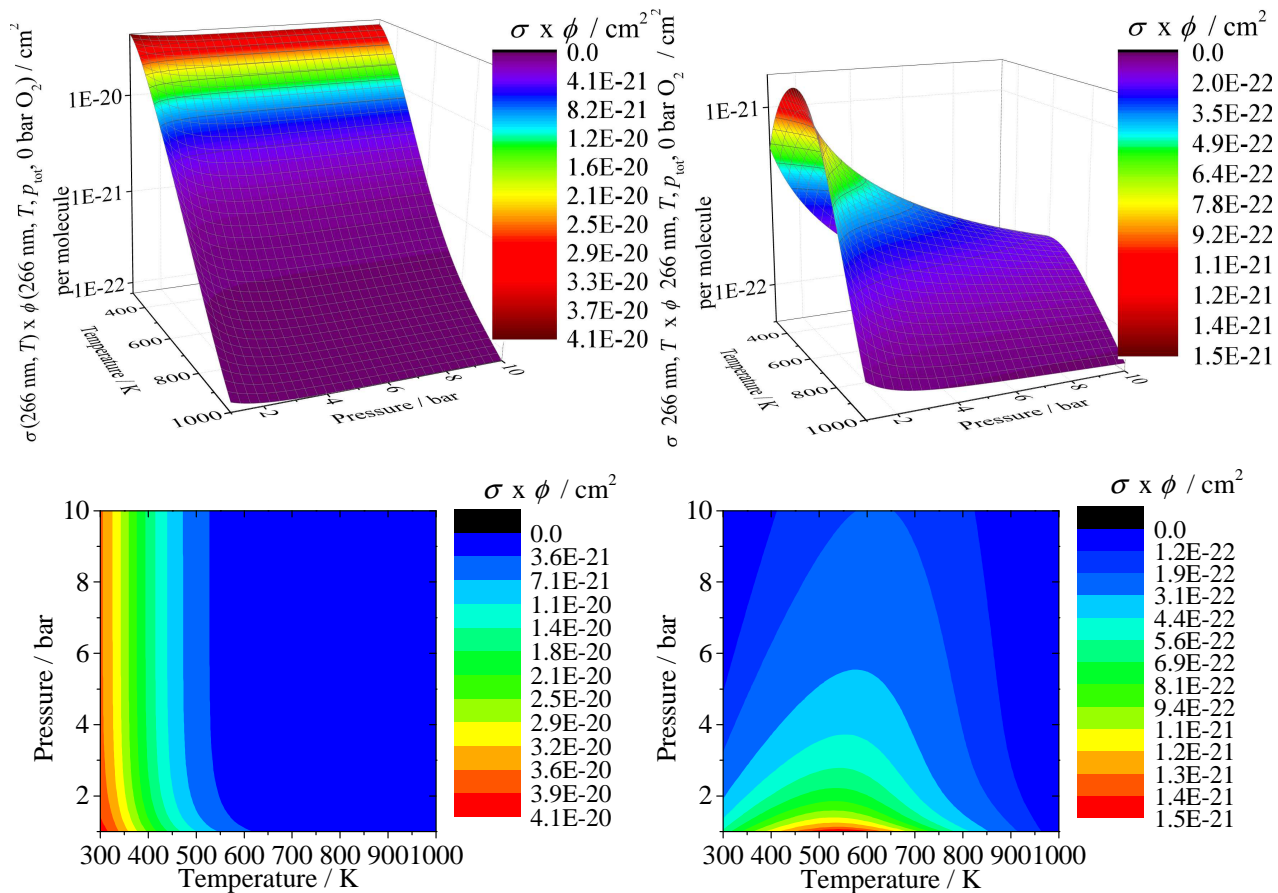


Figure 71: Fluorescence signal prediction for toluene after 266 nm excitation (upper row) as a function of temperature and total pressure in nitrogen (left) and air (right) as well as the corresponding contour plots (bottom row).

7 Conclusions

The use of photophysical properties of various organic species via laser-induced fluorescence (LIF) for the visualization of mixing processes and quantitative measurement of fuel concentration, fuel/air equivalence ratio, and temperature has become a popular diagnostics method over the last decades. The feasibility of this method was improved by the introduction of aromatic compounds because their absorption cross-section (σ_{abs}) and fluorescence quantum yield (ϕ_{fl}) is several orders of magnitude larger compared to ketones that have been frequently used before. However, just a few of these aromatic species have been investigated in enough detail for applications in quantitative measurements. At the same time, there are still photophysical effects that are not well understood and may be used for diagnostics purposes once their influence on the fluorescence parameters (σ_{abs} , ϕ_{fl} , different fluorescence lifetime components, and the changing shape of the spectrum) can be fully explained. These two aspects were the main goal of this thesis, which contributes new and previously unpublished results towards a growing data base of aromatic tracer species spectroscopy.

Investigating the pressure dependences of the ϕ_{fl} for several aromatics (toluene, 1,2,4-trimethylbenzene, anisole, naphthalene, and 1-methylnaphthalene) at low pressure (10–1000 mbar) for temperatures between 296 and 475 K in N_2 after 266 nm excitation with a ps-Nd:YAG laser, the effect of collisions on the excited-state energy randomization could be illuminated. The interplay between the thermal equilibrium and the initial excess energy leads to an increase or a decrease of the internal energy of the fluorescence tracer and thereby influences the total relaxation rate responsible for the non-radiative deactivation of the tracer. This directly impacts the fluorescence quantum yield and the fluorescence lifetime. This result is the experimental proof of photo-induced cooling previously discussed for species like naphthalene [45]. As a by-product of the measurement of fluorescence lifetimes at almost collision-free conditions, quantitative temperature-dependent rate constants for the non-radiative deactivation of toluene, 1,2,4-trimethylbenzene, anisole, naphthalene, and 1-methylnaphthalene are extracted and can now be used for photophysical model development.

Self-quenching of tracers at high concentration can also reduce the fluorescence quantum yield. This process was investigated much less than the quenching of excited states by molecular oxygen. A quantitative study of self-quenching of toluene was undertaken, which combines the techniques of integrated fluorescence and fluorescence lifetime measurements for different tracer number densities and laser fluences. By tracer excitation with of a picosecond Nd:YAG laser with nanojoule pulse energies and time-correlated single-photon counting detection, it was possible to identify collisions between excited tracer molecules as the main source of self-quenching. With this knowledge, an error-estimation formula was derived that calculates the estimated signal in dependence of the laser fluence and the tracer number density.

A complete photo-physical characterization of 1,4-difluorobenzene, 1,2-xylene, and 1,2,4-trimethylbenzene is presented in this thesis. This includes σ_{abs} in dependence of the excitation

wavelength (250–380 nm) and temperature (296–700 K), ϕ_{fl} and fluorescence spectra in dependence on temperature (296–1075 K), total pressure (1–10 bar) and O₂ partial pressure (0–210 mbar). This was done after excitation with a ps-Nd:YAG laser and measured by a spectrometer-coupled streak camera. In addition, semi-empirical fluorescence signal models are shown. The absorption cross-section of anisole and the fluorescence spectra and the ϕ_{fl} of 1-methylnaphthalene in the same parameter range are presented as well. The differences between the absolute values of σ_{abs} and ϕ_{fl} for the different aromatics as well as their dependence on the investigated parameter changes are significant. As an example, the longest fluorescence lifetimes (generally obtained at room temperature in 1 bar N₂) vary from 110 ns (1-methylnaphthalene) to 7 ns (difluorobenzene). However the large difference in fluorescence lifetimes does not reflect the variation in ϕ_{fl} . Due to different non-radiative deactivation rates, ϕ_{fl} is quite similar for these two aromatic tracers. The same applies to quenching by O₂, which is most prominent for 1-methylnaphthalene (Stern–Volmer coefficient of 1000 bar⁻¹) and almost negligible for difluorobenzene (Stern–Volmer coefficient of 35 bar⁻¹). This is at least true for every aromatic tracer in Figure 66 that all have increasing Stern-Volmer coefficients with increasing (natural) fluorescence lifetime, which makes sense considering the collision induced nature of the process.

Overall, DFB outperformed the other aromatic tracers that were investigated up to this point in terms of signal per molecule, and also by possible signal per volume due to its high vapor pressure (see Figures 67–70). This difference in signal intensity increases even more in the presence of O₂ due to its low propensity to quenching. One (but significant) disadvantage is that difluorobenzene can form hydrofluoric acid during pyrolysis and combustion. Apart from difluorobenzene, the signal per molecule of 1-methylnaphthalene is very strong, due to the high σ_{abs} and a low decrease of ϕ_{fl} with increasing temperature. However, its signal is strongly quenched by O₂ (comparable to naphthalene), reducing the fluorescence intensity to the level of toluene. 1,2-Xylene and 1,2,4-trimethylbenzene exhibit roughly the same photophysical behavior as toluene, with increasing σ_{abs} and better spectral separation for two-color thermometry with increasing methylation. However, the evaporation characteristics change (e.g., boiling point increases, vapor pressure decreases) reducing the overall fluorescence signal in cases where the total tracer volume is important. The σ_{abs} of anisole turns out to be a factor of three lower than was estimated by Faust et al. [41] but explains the deviations between expectation and measurement in [42] and are in accordance with the data presented by Zabeti et al. [40].

The results in this thesis show, that there is no perfect tracer that is best suited for all potential applications. All tracers have their individual strengths and weaknesses when it comes to parameter dependences, signal intensities, or chemistry. But with the additional information provided by this thesis, the pool of possible fluorescence tracers for quantitative optical diagnostics on mixing flows and combustion processes has been enriched and completed. In addition, the knowledge on the origin of the total pressure dependence of the ϕ_{fl} and the origin of self-quenching provide fundamental information on laser-induced fluorescence of organic molecules.

8 List of references

1. R.K. Hanson, Application of quantitative laser sensors to kinetics, propulsion and practical energy systems. Proc. Combust. Inst. 2011. 33: 1-40.
2. A.C. Eckbreth, Laser diagnostics for combustion temperature and species. 2nd ed. [compl. rev. and updated]. 1996: Amsterdam: Gordon & Breach
3. J.B. Jeffries, K. Kohse-Höinghaus, Applied combustion diagnostics. 2002: New York: Taylor and Francis
4. C. Schulz, V. Sick, Tracer-LIF diagnostics: quantitative measurement of fuel concentration, temperature and fuel/air ratio in practical combustion systems. Prog. Energy Combust. Sci. 2005. 31: 75-121.
5. W. Koban, Photophysical characterization of toluene and 3-pentanone for quantitative imaging of fuel/air ratio and temperature in combustion systems. dissertation. 2005: Ruperto-Carola University Heidelberg, Germany
6. F. Ossler, T. Metz, M. Aldén Picosecond laser-induced fluorescence from gas-phase polycyclic aromatic hydrocarbons at elevated temperatures I. Cell measurements Appl. Phys. B. 2001. 72: 465-478
7. F. Ossler, T. Metz, M. Aldén Picosecond laser-induced fluorescence from gas-phase polycyclic aromatic hydrocarbons at elevated temperatures. II. Flame-seeding measurements Appl. Phys. B 2001. 72: 479-489
8. J.D. Koch, Fuel Tracer Photophysics for Quantitative Planar Laser-Induced Fluorescence. dissertation. 2005: Stanford University California, USA
9. B.H. Cheung, R.K. Hanson, 3-pentanone fluorescence yield measurements and modeling. Appl. Phys. B 2012. 106: 755-768.
10. B. Rossow, Photophysical processes of organic fluorescent molecules and kerosene - application to combustion engines. dissertation. 2011: Université Paris-Sud 11 Paris, France
11. W. Koban, J.D. Koch, V. Sick, N. Wermuth, R.K. Hanson, C. Schulz, Predicting LIF signal strength for toluene and 3-pentanone under engine-related temperature and pressure conditions. Proc. Combust. Inst. 2005. 30: 1545-1553.
12. P. Baranger, M. Orain, F. Grisch, Fluorescence Spectroscopy of Kerosene Vapour: Application to Gas Turbines. AIAA paper 2005. 2005-828.
13. <https://www.sigmaldrich.com>. 2017.
14. J. Savard, Comparative spectrum analysis of *o*-, *m*- and *p*-isomerides of certain benzene

- derivatives. *Ann. Chim.* 1929. 10: 287-350.
15. A.M. Bass, Fluorescence Studies of Some Simple Benzene Derivatives in the Near Ultraviolet. II. Toluene and Benzonitrile. *J. Chem. Phys.* 1950. 18: 1403-1410.
 16. W. Koban, J.D. Koch, R.K. Hanson, C. Schulz, Absorption and fluorescence of toluene vapor at elevated temperatures. *Phys. Chem. Chem. Phys.* 2004. 6: 2940-2945.
 17. C.S. Burton, W.A. Noyes, Electronic Energy Relaxation in Toluene Vapor. *J. Chem. Phys.* 1968. 49: 1705-1714.
 18. C. Gessenhardt, F. Zimmermann, C. Schulz, R. Reichle, C. Pruss, W. Osten, Hybrid endoscopes for laser-based imaging diagnostics in IC engines. SAE technical paper series 2009. 2009-01-0655.
 19. M. Luong, R. Zhang, C. Schulz, V. Sick, Toluene laser-induced fluorescence for in-cylinder temperature imaging in internal combustion engines. *Appl. Phys. B* 2008. 91: 669-675.
 20. W. Koban, J.D. Koch, R.K. Hanson, C. Schulz, Oxygen quenching of toluene fluorescence at elevated temperatures. *Appl. Phys. B* 2005. 80: 777-784.
 21. K. Mohri, M. Luong, G. Vanhove, T. Dreier, C. Schulz, Imaging of the oxygen distribution in an isothermal turbulent free jet using two-color toluene LIF imaging. *Appl. Phys. B* 2011. 103: 707-715.
 22. S. Faust, T. Dreier, C. Schulz, Temperature and bath gas composition dependence of effective fluorescence lifetimes of toluene excited at 266 nm. *J. Chem. Phys.* 2011. 383: 6-11.
 23. S. Faust, G. Tea, T. Dreier, C. Schulz, Temperature, pressure, and bath gas composition dependence of fluorescence spectra and fluorescence lifetimes of toluene and naphthalene. *Appl. Phys. B* 2013. 110: 81-93.
 24. S.A. Kaiser, M. Schild, C. Schulz, Thermal stratification in an internal combustion engine due to wall heat transfer measured by laser-induced fluorescence. *Proc. Combust. Inst.* 2013. 34: 2911-2929.
 25. B.H. Cheung, Tracer-based planar laser-induced fluorescence diagnostics: Quantitative photophysics and time-resolved imaging. dissertation. 2011: Stanford University California, USA.
 26. J. Yoo, D. Mitchell, D.F. Davidson, R.K. Hanson, Planar laser-induced fluorescence imaging in shock tube flows. *Exp. Fluids* 2010. 49: 751-759.
 27. F.P. Zimmermann, W. Koban, C.M. Roth, D.-P. Herten, C. Schulz, Fluorescence lifetime of gas-phase toluene at elevated temperatures. *Chem. Phys. Lett.* 2006. 426: 248-251.
 28. G.M. Breuer, E.K.C. Lee, Fluorescence Decay Times and non-Radiative Decay Rates of the First Excited Singlet States of Methylated and Fluorinated Benzenes. *Chem. Phys. Lett.*

1972. 14: 404-406.
29. C.G. Hickman, J.R. Gascooke, W.D. Lawrance, The S_1 - $S_0(1B_{2-1}A_1)$ transition of jet-cooled toluene: Excitation and dispersed fluorescence spectra, fluorescence lifetimes, and intramolecular vibrational energy redistribution. *J. Chem. Phys.* 1996. 104: 4887-4901.
 30. M. Jacon, C. Lardeux, R. Lopez-Delgado, A. Tramer, On the "Third Decay Channel" and Vibrational Redistribution Problems in Benzene Derivatives. *Chem. Phys. Lett.* 1977. 24: 145-157.
 31. E.H. Kincaid, V. Worah, M.D. Schuh, Collision-induced state-to-state flow of vibrational energy in S_1 toluene. *J. Chem. Phys.* 1991. 94: 4842-4851.
 32. A. Ehn, B. Kaldvee, J. Bood, M. Aldén, Development of a temporal filtering technique for suppression of interferences in applied laser-induced fluorescence diagnostics. *Appl. Opt.* 2009. 48: 2373-2387.
 33. E. Friesen, C. Gessenhardt, S.A. Kaiser, T. Dreier, C. Schulz, In-cylinder temperature measurements via time-correlated single-photon counting of toluene-LIF through a fiber-based sensor. *Opt. Lett.* 2012. 37: 5244-5246.
 34. E. Friesen, C. Gessenhardt, S. Kaiser, T. Dreier, C. Schulz. In-cylinder temperature measurements via fiber-based toluene-LIF time-correlated single-photon counting. in LACSEA2012. 2012. San Diego, CA, USA.
 35. T. Etzkorn, B. Klotz, S. Sörensen, I.V. Patroescu, I. Barnes, K.H. Becker, U. Platt, Gas-phase absorption cross sections of 24 monocyclic aromatic hydrocarbons in UV and IR spectral range. *Atmos. Environ* 1999. 33: 525-540.
 36. S. Fally, M. Carleer, A.C. Vandaele, UV Fourier transform absorption cross sections of benzene, toluene, meta-, ortho-, and para-xylene. *J. Quant. Spectrosc. Radiat. Transfer* 2009. 110: 766-782.
 37. M. Orain, P. Baranger, B. Rossow, F. Grisch, Fluorescence spectroscopy of 1,2,4-trimethylbenzene at high temperatures and pressures: application to temperature measurements. *Appl. Phys. B* 2010. 100: 945-952.
 38. J.K. Marsh, Studies in Fluorescence Spectra. Part II. Phenol and Phenolic Ether Vapours. *J. Chem. Soc. Trans.* 1924. 125: 418-423.
 39. T. Hirasawa, T. Kaneba, Y. Kamata, K. Muraoka, Y. Nakamura, Temperature Dependence of Intensities of Laser-Induced Fluorescences of Ethylbenzene and Naphthalene Seeded in Gas Flow at Atmospheric Pressure: Implications for Quantitative Visualization of Gas Temperature. *J. Visualization* 2007. 10: 197-206.
 40. S. Zabeti, M. Aghsaee, M. Fikri, O. Welz, C. Schulz, A high-temperature shock-tube study on the optical properties and pyrolysis of anisole. *Proc. Combust. Inst.* 2017. 36: 4525-4532.

41. S. Faust, T. Dreier, C. Schulz, Photo-physical properties of anisole: temperature, pressure, and bath gas composition dependence of fluorescence spectra and lifetimes. *Appl. Phys. B* 2013. 112: 203-213.
42. S. Faust, M. Goschütz, S.A. Kaiser, T. Dreier, C. Schulz, A comparison of selected organic tracers for quantitative scalar imaging in the gas phase via laser-induced fluorescence. *Appl. Phys. B* 2014. 117: 183-194.
43. L.J. Volk, E.K.C. Lee, Reinvestigation of vibronic level dependence of fluorescence quantum yields and radiative and nonradiative lifetimes of p-difluorobenzene in its first excited singlet state ($^1B_{2u}$). *J. Chem. Phys.* 1977. 67: 236-241.
44. L.M. Itani, G. Bruneaux, A. Di Lella, C. Schulz, Two-tracer LIF imaging of preferential evaporation of multi-component gasoline fuel sprays under engine conditions. *Proc. Combust. Inst.* 2015. 35: 2915-2922.
45. Y. He, E. Pollak, Theory of fluorescence decay of naphthalene: Was photoinduced cooling observed experimentally? *J. Chem. Phys.* 2002. 116: 6088-6101.
46. J.C. Hsieh, C.-S. Huang, E.C. Lim, Radiationless singlet deactivation in isolated large molecules. I Naphthalene, naphthol, and naphthylamine. *J. Chem. Phys.* 1974. 60: 4345-4353.
47. A. Reimann, Über die Photolumineszenz des Benzols und einiger Derivate in verschiedenen Aggregat- und Lösungszuständen. *Ann. Phys.* 1926. 80: 43-70.
48. R.E. Smalley, Dynamics of Electronically Excited States. *Annu. Rev. Phys. Chem.* 1983. 34: 129-153.
49. M. Stockburger, H. Gattermann, W. Klusmann, Spectroscopic studies on naphthalene in the vapor phase. II. Fluorescence quantum yields from single vibronic levels in the first excited singlet state - behavior of higher excited singlet states. *J. Chem. Phys.* 1975. 63: 4529-4540.
50. E. Wiedemann, G.C. Schmidt, Ueber Lichtemission organischer Substanzen im gasförmigen, flüssigen und festen Zustand. *Ann. Phys.* 1895. 56: 18-26.
51. M. Orain, P. Baranger, B. Rossow, F. Grisch, Fluorescence spectroscopy of naphthalene at high temperatures and pressures: implications for fuel-concentration measurements. *Appl. Phys. B.* 2011. 102: 163-172.
52. S.A. Kaiser, M.B. Long, Quantitative planar laser-induced fluorescence of naphthalenes as fuel tracers. *Proc. Combust. Inst.* 2005. 30: 1555-1563.
53. J. Ferguson, L.W. Reeves, W.G. Schneider, Vapor absorption spectra and oscillator strengths of naphthalene, anthracene, and pyrene. *Can. J. Chem.* 1957. 35: 1117-1136.
54. T. Ni, L.A. Melton, Two-Dimensional Gas-Phase Temperature Measurements Using Fluorescence Lifetime Imaging. *Appl. Spectr.* 1996. 50: 1112-1116.

55. J. Reboux, D. Puechberty, F. Dionnet, A New Approach of Planar Laser Induced Fluorescence Applied to Fuel/Air Ratio Measurement in the Compression Stroke of an Optical S.I. Engine. SAE technical paper series 1994. 941988.
56. J. Scholz, T. Wiersbinski, V. Beushausen Planar Fuel-Air-Ratio-LIF with Gasoline for Dynamic Mixture-Formation Investigations. SAE technical paper series 2007. 2007-01-0645.
57. W. Koban, C. Schulz, Toluene laser-induced fluorescence (LIF) under engine-related pressures, temperatures and oxygen mole fractions. SAE technical paper series 2005. 2005-01-2091.
58. W. Koban, J.D. Koch, R.K. Hanson, C. Schulz, Toluene LIF at elevated temperatures: implications for fuel/air ratio measurements. *Appl. Phys. B*. 2005. 80: 147-150.
59. M. Luong, W. Koban, C. Schulz, Novel strategies for imaging temperature distribution using Toluene LIF. *J. Phys.: Conf. Series* 2006. 45: 155-161.
60. B. Peterson, D.L. Reuss, V. Sick, High-speed imaging analysis of misfires in a spray-guided direct injection engine. *Proc. Combust. Inst.* 2011. 33: 3089-3096.
61. H. Krämer, S. Einecke, C. Schulz, V. Sick, S.R. Natrass, J.S. Kitching, Simultaneous mapping of the distribution of different fuel volatility classes using tracer-LIF tomography in an IC engine. *SAE Transactions, Journal of Fuels & Lubricants* 1998. 107: 1048-1059.
62. T. Ni, L.A. Melton, Fluorescence Lifetime Imaging: An Approach for Fuel Equivalence Ratio Imaging. *Appl. Spectr.* 1991. 45: 938-943.
63. A. Ehn, O. Johansson, A. Arvidsson, M. Aldén, J. Bood, Single-laser shot fluorescence lifetime imaging on the nanosecond timescale using a dual image and modeling algorithm. *Opt. Exp.* 2012. 20: 3043-3056.
64. P.W. Atkins, J. de Paula, *Physikalische Chemie*. 2006, Weinheim: Wiley-VCH.
65. J.R. Lakowicz, *Principles of Fluorescence Spectroscopy*. 3rd ed. 2006, New York: Springer Science + Business Media, LLC.
66. A. Gilbert, J.E. Baggott, *Essentials of molecular photochemistry*. 1991: Crc Pr I Llc.
67. R. Kienle, M.P. Lee, K. Kohse-Hoinghaus, A scaling formalism for the representation of rotational energy transfer in OH A in combustion experiments. *Appl. Phys. B* 1996. 63: 403.
68. M.C. Thurber, F. Grisch, B.J. Kirby, M. Votsmeier, R.K. Hanson, Measurements and modeling of acetone laser-induced fluorescence with implications for temperature-imaging diagnostics. *Appl. Opt.* 1998. 37: 4963-4978.
69. J.B. Birks, Energy transfer in organic systems. *J. Phys. B* 1970. 3: 417-424.
70. D.L. Dexter, A Theory of Sensitized Luminescence in Solids. *J. Chem. Phys.* 1953. 21: 836-

- 850.
71. T. Förster, Zwischenmolekulare Energiewanderung und Fluoreszenz. *Ann. Phys.* 1948. 6: 55-75.
72. K. Shibuya, F. Stuhl, Fluorescence Lifetime and Collisional Quenching of the Predissociative NO B²-Π('v'=7) State. *J. Chem. Phys.* 1983. 3: 367-381.
73. V. Sivakumaran, K.P. Subramanian, V. Kumar, Self-quenching and zero-pressure lifetime studies of NO₂ at 465–490, 423–462 and 399–416 nm. *J. Quant. Spectrosc. Radiat. Transfer* 2001. 69: 525-534.
74. W.R. Ware, P.T. Cunningham, Lifetime and Quenching of Anthracene Fluorescence in the Vapor Phase. *J. Chem. Phys.* 1965. 43: 3826-3831.
75. A. Davis, M.J. Pilling, M.J. Westby, Concentration Quenching of Pyrene (B⁻¹)_{lu} in the Vapor-Phase. *J. Chem. Phys.* 1981. 63: 208-218.
76. M.C. Thurber, R.K. Hanson, Pressure and composition dependence of acetone laser-induced fluorescence with excitation at 248, 266, and 308 nm. *Appl. Phys. B* 1999. 69: 229-240.
77. T. Endres, Step-ladder model for toluene. private communication. University of Duisburg-Essen, 2016.
78. T. Benzler, Druck- und Temperaturabhängigkeit effektiver Fluoreszenzlebensdauern einiger Aromaten in der Gasphase. Master Thesis. 2013: University of Duisburg-Essen
79. H. Wadi, E. Pollak, Theory of laser cooling of polyatomic molecules. *J. Chem. Phys.* 1999. 110: 11890-11905.
80. Information, N.C.f.B., PubChem Compound Database.
81. A. Bolovinos, J. Philis, E. Pantos, P. Tsekeris, G. Andritsopoulos, The methylbenzenes vis-a-vis benzene, Comparison of their spectra in the valence-shell transitions region. *J. Mol. Spectros.* 1982. 94: 55–68.
82. L.J.H. Hoffmann, S. Marquardt, A.S. Gemechu, H. Baumgärtel, The absorption spectra of anisole-h8, anisole-d3 and anisole-d8. The assignment of fundamental vibrations in the S₀ and the S₁ states. *Phys. Chem. Chem. Phys.* 2006. 8: 2360-2377.
83. G.S. Beddard, S.J. Formosinho, G. Porter, Pressure Effects on Fluorescence from Naphthalene Vapor. *Chem. Phys. Lett.* 1973. 22: 235-238.
84. Hamamatsu Photonics, Available from: http://sales.hamamatsu.com/assets/pdf/parts_C/e_C5680.pdf 2011.
85. N. Nijegorodov, R. Mabbs, D.P. Winkoun, Influence of weak and strong donor groups on the fluorescence parameters and the intersystem crossing rate constant. *Spectrochim. Acta A* 2003. 59: 595-606.

86. J.A. Draeger, The methylbenzenes-I. Vapor-phase vibrational fundamentals, internal rotations and a modified valence force field, *Spectrochimica. Acta A* 1985. 41: 607-627.
87. J.E. Dec, J.O. Keller, High speed thermometry using two-line atomic fluorescence. *Proc. Combust. Inst.* 1986. 21: 1737-1745.
88. S. Lind, et al., Application of tracer combination TEA/acetone for multi-parameter laser-induced fluorescence measurements in IC engines with exhaust gas recirculation. *Proc. Combust. Inst.* 2015. 35: 3783-3791.
89. T. Blotevogel, M. Hartmann, H. Rottengruber, A. Leipertz,, Tracer-based laser-induced fluorescence measurement technique for quantitative fuel/air-ratio measurements in a hydrogen internal combustion engine. *Appl. Opt.* 2008. 47: 6488-6496.
90. J. Trost, L. Zigan, A. Leipertz, D. Sahoo, P.C. Miles, Characterization of four potential laser-induced fluorescence tracers for diesel engine applications. *Appl. Opt.* 2013. 52: 8001 - 8008.
91. J.E. Dec, W. Hwang Characterizing the development of thermal stratification in an HCCI engine using planar-imaging thermometry. SAE technical paper series 2009. 2009-01-0650.
92. B.R. Petersen, J.B. Gandhi, J.D. Koch, Fluorescence saturation measurements of 3-pentanone. *Appl. Phys. B* 2008. 93: 639-644.
93. R.G. Brown, D. Phillips, Quenching of the first excited singlet state of substituted benzenes by molecular oxygen. *Trans. Farad. Soc. II* 1974. 70: 630-636.
94. T. Cvitas, J.M. Hollas, Rotational band contour analysis in the 2710 Å system of p-difluorobenzene *Molecular Physics* 1970. 18: 793-800.
95. M.G. Rockley, J. Metcalfe, D. Phillips, Singlet to Triplet Absorption-Spectra of Substituted Benzenes. *Journal of the Chemical Society-Faraday Transactions II* 1974. 70: 1660-1666.
96. W. Koban, J. Schorr, C. Schulz, Oxygen-distribution imaging with a novel two-tracer laser-induced fluorescence technique. *Appl. Phys. B* 2002. 74: 111-114.
97. R. Devillers, G. Bruneaux, C. Schulz, Investigation of toluene LIF at high pressure and high temperature in an optical engine. *Appl. Phys. B* 2009. 96: 735-739.
98. D. Fuhrmann, T. Benzler, S. Fernando, T. Endres, T. Dreier, S. A. Kaiser, C. Schulz, Self-quenching in toluene LIF. *Proc. Combust. Inst.* 2016. 36.
99. T.B. Settersten, A. Dreizler, R.L. Farrow, Temperature- and species-dependent quenching of CO B probed by twophoton laser-induced fluorescence using a picosecond laser. *J. Chem. Phys.* 2002. 117: 3173-3179.
100. T.B. Settersten, B.D. Patterson, J.A. Gray, Temperature- and species-dependent quenching of NO A² Σ⁺ (v'=0) probed by two-photon laser-induced fluorescence using a picosecond laser. *J. Chem. Phys.* 2006. 124: 234-308.

101. J.M. Hollas, T. Cvitas, Rotational Band Contour Analysis in 2710 a System of Para-Difluorobenzene. *Mol. Phys.* 1970. 18: 793-800.
102. T. Benzler, S. Faust, T. Dreier, C. Schulz, Low-pressure effective fluorescence lifetimes and photo-physical rate constants of one- and two-ring aromatics *Appl. Phys. B* 2015. 121: 549-558.
103. R.A. Coveleskie, D.A. Dolson, C.S. Parmenter, Chemical Timing .1. A Method of Picosecond Fluorescence Spectroscopy for the Study of Intramolecular Vibrational Redistribution. *J. Phys. Chem.* 1985. 89: 645-654.
104. M. Loeffler, F. Beyrau, A. Leipertz, Acetone laser-induced fluorescence behavior for the simultaneous quantification of temperature and residual gas distribution in fired spark-ignition engines. *Appl. Opt.* 2010. 49: 37-49.
105. S. Lind, S. Aßmann, L. Zigan, S. Will, Fluorescence characteristics of the fuel tracers triethylamine and trimethylamine for the investigation of fuel distribution in internal combustion engines. *Appl. Opt.* 2016. 55: 1551-1558.
106. T. Benzler, T. Dreier, C. Schulz, UV absorption and fluorescence properties of gas-phase p-difluorobenzene. *Appl. Phys. B* 2017. 123: 39.
107. C. Schulz, J. Gronki, S. Andersson, Multi-Species Laser-Based Imaging Measurements in a Diesel Spray. SAE technical paper series 2004. 2004-01-1917.
108. D. Frieden, V. Sick, J. Gronki, C. Schulz, Quantitative oxygen imaging in an engine. *Appl. Phys. B.* 2002. 75: 137-141.
109. G.S. Beddard, G.R. Fleming, O.L.J. Gijzeman, G. Porter, Vibrational energy dependence of radiationless conversion in aromatic vapours. *Proc. R. Soc. Lond. A* 1974. 340: 519-533.
110. T. Benzler, S. Faust, T. Dreier, C. Schulz, Low-pressure effective fluorescence lifetimes and photo-physical rate constants of one- and two-ring aromatics. *Appl. Phys. B* 2015. 121: 549-558.
111. J.D. Koch, R.K. Hanson, Temperature and excitation wavelength dependencies of 3-pentanone absorption and fluorescence for PLIF applications. *Appl. Phys. B* 2003. 76: 319-324.
112. B. Rossow, Laser measured absorption cross-section of 1-Methylnaphthalene. personal communication. Complexe de Recherche Interprofessionnel en Aérothermochimie, Saint-Étienne-du-Rouvray, France. 2016.

9 Acknowledgement

First of all, I want to acknowledge Prof. Christof Schulz for giving me the opportunity to do my PhD in his fantastic workgroup. I was able to meet a lot of interesting, fun, intelligent, and caring people, see different countries and experience my best years in life so far. I also want to thank him for the insightful discussions we had over the years, his elaborate ideas and suggestions for my experiments and his constant drive for improvement and critical eye for details which (at least partially) rubbed off on me.

My special thanks goes to Dr. Thomas Dreier for his guidance over the past years that made somewhat of a scientist out of the student that I once was. Without his support and knowledge, I would not have been able to do my research on this high level of scientific accuracy. Not to mention his diligent efforts to retype my incoherent writing into something widely understandable.

Further I want to acknowledge my (current and former) colleagues of Prof. Schulz' group, especially the diagnostics team: Dr. Stefan Faust, Simon Görs, Dr. Torsten Endres, Jan Menser, Mathias Beuting, Thomas Baranowski, Dr. Omid Feroughi, Raphael Mansmann, Eugen Friesen, Markus Röder, and Dr. Martin Leschowski. Thanks to you, the working atmosphere has always been pleasant and the fruitful discussions in scientific and private matters have been a great help for me. Thanks to the engine group of Prof. Sebastian Kaiser, especially Dr. Martin Goschütz and Dr. Daniel Fuhrmann for their collaboration and practical outlook on the usage of my research. Additional thanks goes to Dr. Mustapha Fikri and Siavash Zabeti from the kinetics group for their insights on tracer pyrolysis.

Special thanks goes to all the technical and administrative staff in the workgroup of Prof. Schulz, first off all Ludger Jerig and Dr. Erdal Akyildiz for their great engagement in construction work and practical help in the lab. I would also like to acknowledge Jörg Albrecht, Beate Endres, Barbara Graf, Dieter Hermanns, Birgit Nelius, Barbara Nota, and Natascha Schlösser for their continuous help throughout my work.

Further thanks go to the whole Schulz group, for the delightful atmosphere, for the pleasant celebrations and several outings.

Last but not least, I thank my wife Sandra for her love and support, as well as some well-deserved kicks in the butt to finish up this thesis, as well as my father who ended up asking if I finished my thesis every time we met. Special thanks go also to my friends and family for their confidence in me and my work as well as their continuous moral support.

DuEPublico

Duisburg-Essen Publications online

UNIVERSITÄT
DUISBURG
ESSEN

Offen im Denken

ub | universitäts
bibliothek

Diese Dissertation wird über DuEPublico, dem Dokumenten- und Publikationsserver der Universität Duisburg-Essen, zur Verfügung gestellt und liegt auch als Print-Version vor.

DOI: 10.17185/duepublico/70230

URN: urn:nbn:de:hbz:464-20190709-142133-9

Alle Rechte vorbehalten.